Porosity Studies of Isoreticular Mixed-Ligand Metal-Organic Frameworks

Nolwazi Gcwensa

Dissertation presented for the degree of

Master of Science

in the Department of Chemistry

University of Cape Town

February 2019

Supervisor: Clive L. Oliver

Plagiarism Declaration

I know the meaning of plagiarism and hereby declare that the work on which this dissertation is based is my original work (except where acknowledgements indicate otherwise) and that neither the whole work nor any part of it has been, is being, or is to be submitted for another degree in this or any other university. I authorise the University to reproduce for the purpose of research either the whole or any portion of the contents in any manner whatsoever.

Signature: Signed by candidate Date: ……11 February 2019……

Acknowledgements

A special thanks to:

- My supervisor Dr Clive L. Oliver for his patience and supervision. The lessons I learnt through his guidance will be carried with me throughout my entire career.
- Dr Nabanita Chatterjee for her help and friendship. Working alongside you has been a gift.
- The members of the Centre for Supramolecular Chemistry Research group for their advice, assistance and friendship. You have helped make my journey a little easier and brighter.
- Sasol bursaries and the Allan Gray Orbis Foundation for their financial support.
- My friends and family for their patience and love. I would not have gotten here without all of you.
- To my mother especially for standing with me, helping me decide and keeping me going when I thought I had nothing left to give.

Parts of this thesis have been published:

Gcwensa, N.; Chatterjee, N.; Oliver, C. L. Interchanged Hysteresis for Carbon Dioxide and Water Vapor Sorption in a Pair of Water-Stable, Breathing, Isoreticular, 2-Periodic, Zn(II)-Based Mixed-Ligand Metal-Organic Frameworks *Inorg. Chem.* **2019,** *58*, 2080-2088.

Abbreviations

MOF – Metal-organic framework

SBU – Secondary building unit

bpy – 4,4'-bipyridine

bimb – 1,4-bis(imidazol-1-yl)-butane

1D – one dimensional

2D – two dimensional

3D – three dimensional

TATB - 4,4',4"-*s*-triazine-2,4,6-triyltribenzoate

bdc – 1,4-benzenedicarboxylate

nbdc – 5-nitro-1,3-benzenedicarboxylate

dpNDI – N,N'-di(4-pyridyl)-1,4,5,8-naphthalenediimide

SC-SC – single-crystal-to-single-crystal

1,4-AphaH – 4-aminophenylhydroxamic acid

H_2**ia** – isophthalic acid / 1,3-benzenedicarboxylic acid

H_2**nia** – 5-nitroisophthalic acid / 5-nitro-1,3-benzenedicarboxylic acid

H_2**mia** – 5-methoxyisophthalic acid / 5-methoxy-1,3-benzenedicarboxylic acid

bpe – 1,2-bis(4-pyridyl)ethane

bpee – 1,2-bis(4-pyridyl)ethylene

DMF – *N*,*N'*-dimethylformamide

SCXRD – single crystal X-ray diffraction

VT–SCXRD – variable-temperature single crystal X-ray diffraction

PXRD – powder X-ray diffraction

VT–PXRD – variable-temperature powder X-ray diffraction

TGA – thermogravimetric analysis

DSC – differential scanning calorimetry

HSM – hot stage microscopy

Compound Codes

Compound **1** – [Zn(μ_2-**ia**)(μ_2-**bpe**)]$_n$·nDMF (as-synthesised)

Compound **2** – [Zn(μ_2-**mia**)(μ_2-**bpe**)]$_n$·nDMF (as-synthesised)

Compound **1W** – [Zn(μ_2-**ia**)(μ_2-**bpe**)]$_n$·n(H_2O)$_2$ (compound **1** solvent exchanged with water)

Compound **2W** – [Zn(μ_2-**mia**)(μ_2-**bpe**)]$_n$·n(H_2O)$_2$ (compound **2** solvent exchanged with water)

Compound **1'** – [Zn(μ_2-**ia**)(μ_2-**bpe**)]$_n$ (**1W** desolvated)

Compound **2'** – [Zn(μ_2-**mia**)(μ_2-**bpe**)]$_n$ (**2W** desolvated)

Compound **3** – [Cd(μ_2-**mia**)(μ_2-**bpe**)$_{1.5}$]$_n$·n(DMF)$_{0.5}$$n$($H_2O$)$_{0.5}$ (as-synthesised)

Compound **4** – [Cd(μ_2-**nia**)(μ_2-**bpee**)$_{1.5}$]$_n$·nDMF (as-synthesised)

Compound **4'** – [Cd(μ_2-**nia**)(μ_2-**bpee**)$_{1.5}$] (**4** desolvated)

JECRAN – [Cd(bpe)$_{1.5}$(nbdc)]$_n$·nDMF

JECROB – [Cd(bpe)$_{1.5}$(nbdc)]$_n$ (**JECRAN** desolvated)

Abstract:

The syntheses of four novel mixed-ligand metal-organic frameworks (MOFs) are reported. Isoreticular, Zn(II)-based mixed-ligand MOFs with formulae [Zn(μ_2-**ia**)(μ_2-**bpe**)]$_n$·*n*DMF (**1**) and [Zn(μ_2-**mia**)(μ_2-**bpe**)]$_n$·*n*DMF (**2**), where **ia** = isophthalate, **mia** = 5-methoxyisophthalate, **bpe** = 1,2-bis(4-pyridyl)ethane and DMF = *N*,*N*'-dimethylformamide were synthesised and characterised. Both compounds **1** and **2** exhibit **sql**, 2-periodic, 2D net coordination layers. Catenation of neighbouring frameworks form 2-fold interpenetrated bilayers which are interdigitated resulting in channel voids containing DMF. Experimental void calculations indicate **2'** has larger void space per unit cell than **1'**; however, experimentally, **1'** showed higher water vapour and carbon dioxide 195 K sorption as well as significant hysteresis upon desorption of carbon dioxide 195 K. This hysteresis behaviour of **1'** is interchanged with **2'** for water vapour sorption at 298 K. Sorption isotherm inflection points indicate that structural changes occur, and empirical evidence point to weak bilayer···bilayer interactions in **1'** which allow the separation of the bilayers as well as the limiting effect on structural changes of the methoxy group present in **2'**.

Isoreticular mixed-ligand Cd(II)-based MOFs with formulae [Cd(μ_2-**mia**)(μ_2-**bpe**)$_{1.5}$]$_n$·*n*(DMF)$_{0.5}$*n*(H_2O)$_{0.5}$ (**3**) and [Cd(μ_2-**nia**)(μ_2-**bpee**)$_{1.5}$]$_n$·*n*DMF (**4**), where **nia** = 5-nitroisophthalate and **bpee** = 1,2-bis(4-pyridyl)ethylene were also synthesised and characterised. Both compounds **3** and **4** exhibit **sql**, 2-periodic, 3D net coordination layers with disorder around a single **bpe** or **bpee** ligand. These structures are compared to published structure [Cd(bpee)$_{1.5}$(nbdc)]$_n$·*n*DMF (**JECRAN**) which is isoreticular to both MOFs. Activation of **4** and **JECRAN** occurs *via* single-crystal-to-single-crystal transformations. Potential and actual void space calculations indicate that **4'** has a larger void space than **3'** and **JECROB**. Liquid sorption experiments revealed that **3'** and **4'** showed affinities for different solvents. Although carbon dioxide 195 K sorption for **4'** is initially higher than for **JECROB**, structural changes, indicated by sorption isotherm inflection points, allow **JECROB** to adsorb more carbon dioxide than **4'**.

Table of Contents

Chapter 1:

Introduction

Topics and terms of interest associated with metal-organic frameworks including supramolecular chemistry, crystal engineering, reticular synthesis, secondary building units and single-crystal-to-single-crystal transformations are discussed. The importance of interpenetration and ligand structural features on the synthesis and porosity of MOFs is highlighted. The rationale behind the use of the mixed ligand synthetic strategy is discussed. The objectives of this research project are stated at the end of **Chapter 1**.

1.1 Supramolecular Chemistry and Crystal Engineering

Supramolecular chemistry, a term coined by Jean-Marie Lehn in his study in inclusion compounds and cryptands, refers to chemistry involving intermolecular bonds.[1] Supramolecular chemistry involves the construction of complex assemblies held together by non-covalent interactions between molecules.[2] These non-covalent interactions include hydrogen bonding, van der Waals interactions, coulombic interactions and pi-pi stacking interactions between molecules.[3] Coordination polymers and metal-organic frameworks are examples of supramolecular complexes owing to their host-guest and host-host interactions.

Understanding and manipulating supramolecular interactions is necessary for greater control of supramolecular synthesis through the rational design of molecular solids with desired chemical and physical properties, a process known as crystal engineering.[2,3] Crystal engineering involves the study of molecular interactions, the packing modes with which these interactions are associated as well as the study of the resulting crystal properties. The goal of crystal engineering is to predict the packing arrangement and physical properties of new, solid-state structures by relying on knowledge of the robust, recurring packing patterns as seen in certain functional groups. The principles of crystal engineering are used in the synthesis of crystalline coordination polymers, known as metal-organic frameworks, which can be prepared with specific and desirable properties through a manipulation of supramolecular principles, i.e. crystallization, a process by which multiple functional groups compete for intermolecular interactions that may create the most stable structure.

1.2 Metal-Organic Frameworks

Metal-organic frameworks (MOFs) are crystalline, porous materials comprised of metal clusters connected by organic linkers. Since 1972, these structures have seen an increase in interest with almost 70 000 MOF entries in the Cambridge Structural Database (CSD), the repository of small molecule crystal structures, by 2016 (**Figure 1.1**).[4,5] MOFs are characterised by their tunable pore sizes and large surface

areas and have garnered interests for their potential applications as storage materials,[6,7] in catalysis,[8,9] separation chemistry,[10,11] and luminescence[12-14].

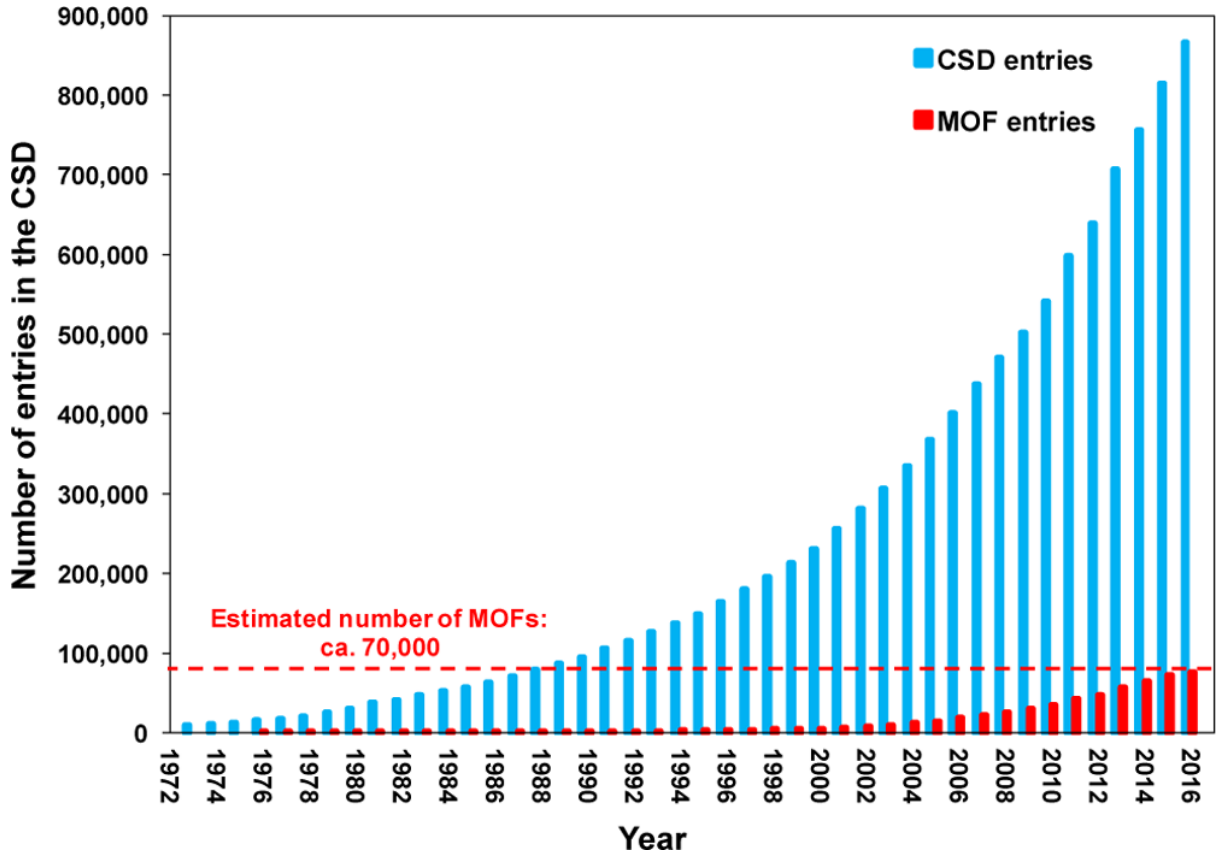

Figure 1.1 Graph to show growth of the CSD and MOF entries since 1972.[5]

Despite extensive research into the synthesis and characterization of MOFs, there are still difficulties in their classification. In broader terminology, MOFs can sometimes be referred to as coordination polymers which has understandably led to some confusion in the literature due to inconsistencies in nomenclature.[15] A coordination polymer is defined as a coordination compound with repeating coordination entities. However, within this definition, coordination polymers need not be crystalline in nature. If that coordination compound extends in one-dimension (with cross-links between two or more individual chains, etc.) or extends in two- or three-dimensions, then it is classed as a coordination network.

In a 2014 review, Carlucci, Proserpio and Blatov made a distinction between dimensionality and periodicity in metal-organic frameworks.[16] In this review, 2-periodic and 3-periodic nets are distinguished from two- and three-dimensional (2D and 3D) nets. Carlucci, Proserpio and Blatov refer to 2- and 3-periodic nets as having infinite coordination in 2 and 3 dimensions, respectively while 2D nets are classed as nets with no finite coordination in the third dimension and 3D nets are nets with a finite coordination in the third dimension that offer the layer a measure of 'thickness' (**Figure 1.2**). In this work, the IUPAC definition of MOFs will be used along with the Carlucci, Proserpio and Blatov convention of describing nets.

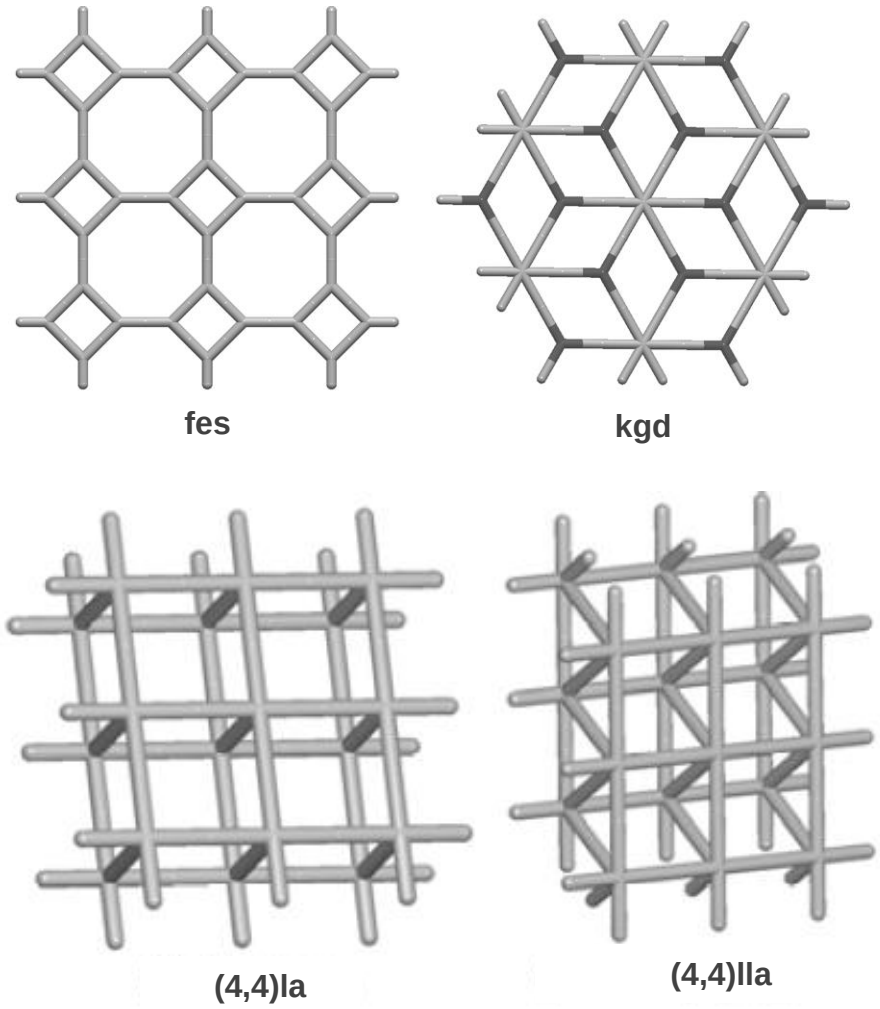

Figure 1.2 Two examples of 2-periodic, 2D nets to depict infinite extension in two dimensions (above) and 2-periodic, 3D nets to depict infinite extension in two dimension and finite coordination in the third dimension i.e. 'thickness' of the layer (below).[16]

A coordination compound is defined as a MOF if the coordination network involves coordination of a metal with organic ligands and contains potential voids. This definition is valid for crystalline and non-crystalline MOFs (**Figure 1.3**).[15] It is this porosity that makes MOFs a topic of interest in multiple fields of chemistry. Although there are other porous materials such as zeolites and activated carbons, the ability to manipulate the pore size of MOFs through synthetic strategy suggests higher potential for practical applications for these coordination polymers.

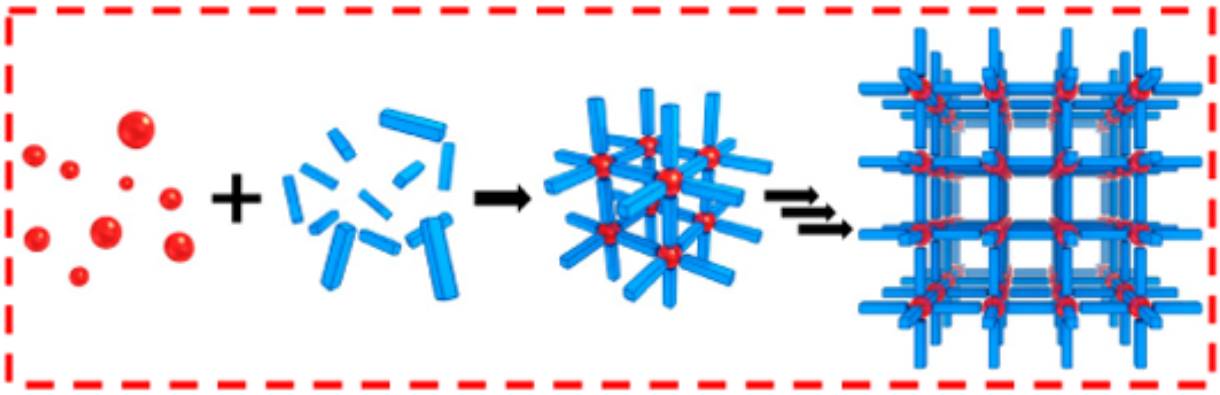

Figure 1.3 Pictogram to show the self-assembly process of a MOF using metal (red spheres) and organic ligands (blue struts) as building blocks.[5]

1.3 Metal-Organic Framework Design

1.3.1 Topology

Analysis of the network topology, the structure of the net associated with the crystal structure, can be used to enhance the description of MOFs. An understanding of the underlying topology of molecular assemblies can also be essential for the rational design of MOFs. A means to simplify the description of complicated crystal lattices in MOFs is to replace the framework components with nodes and rods. A node may replace a metal centre, the centre of a metal cluster or the centroid of a ligand i.e. the centroid of a benzene ring. Rods, which are often aligned with the axis of a ligand, then connect nodes to each other according to the framework structure to form a motif. The overall architecture of the MOF is then simplified to look like that of a scaffolding and more clearly reveals the topology of the MOF which can be used to enhance the description of the framework. In a 2014 survey of entangled, two-dimensional coordination networks, the investigation by Carlucci, Proserpio and Blatov. revealed that of the 75 000 net topologies in the TOPOS TTD collection, the most common 2D motif was the square lattice motif (**sql**) with the honeycomb motif (**hcb**) topology occurring second most regularly (**Figure 1.4**).[16]

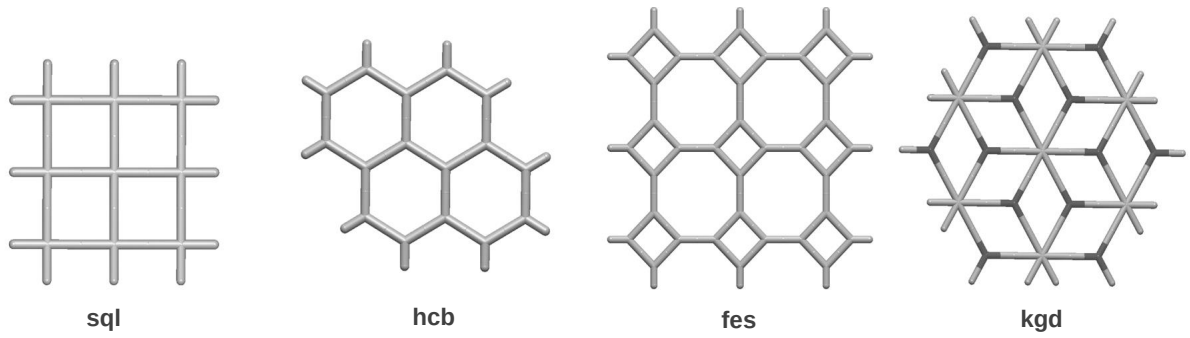

Figure 1.4 Four examples of planar nets observed for 2-periodic, 2D frameworks.[16]

1.3.2 Reticular Synthesis

It is of great interest to devise strategies to synthesise MOFs with specific properties. Reticular synthesis is a synthetic technique which involves the preparation of materials with a targeted geometry and has garnered much success.[17,18] This technique involves the synthesis of a desired network based around the selection of secondary building units to produce materials with predetermined structures and properties. Isoreticular structures are structures which have the same topological net.[19]

Secondary building units (SBUs) for the formation of MOFs are comprised of metal ions and organic linker molecules to form clusters. These units are formed, in situ, through a self-assembly process. An understanding of the way in which certain ligands coordinate and the specifics of the metal environment allows a rational approach to design and the possibility of extending the properties of structure fragments into the extended porous network to produce stable extended frameworks. Metal-oxygen-carbon (M-O-C) clusters are an example of an SBU employed in MOF synthesis wherein the carboxylate functionality is used to chelate metal ions and lock them into rigid frameworks. The synthesis of MOF-5 is one of the first times a rigid framework based on M-O-C SBUs was used to successfully synthesise a MOF.[17,20] In the synthesis of this compound, Zn(II) and benzene dicarboxylic acid were reacted to form an octahedral SBU defined by four ZnO_4 tetrahedra with a common vertex and linked together by benzene dicarboxylate ligands (**Figure 1.5**).

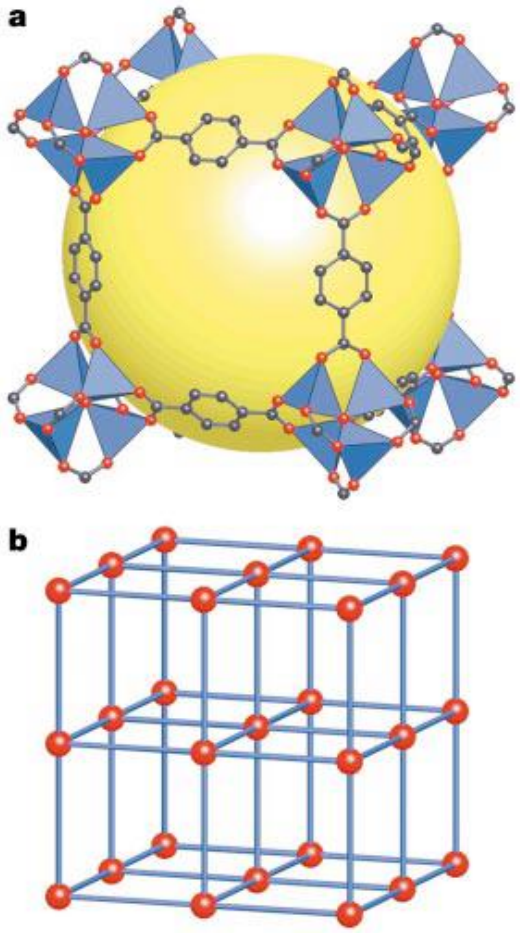

Figure 1.5 (a) The structure and topology of MOF-5 shown as ZnO_4 tetrahedra (blue polyhedra) connected *via* benzene dicarboxylate linkers. Pore depicted as a yellow sphere. (b) Ball and stick model of the primitive cubic net topology of MOF-5.[17,20]

1.4 Porosity

In an article published by Len Barbour, the definition of porosity was broadened to include, not only (i) conventional porosity, but also (ii) virtual porosity and (iii) porosity 'without pores". Virtual porosity involves generating potential void spaces in the framework by deleting certain molecules, i.e. small counterions or solvent molecules, from the ASU of the crystal structure. Usually, further experimentation is needed to prove retainment of crystallinity and permeability with solvent evacuation. Porosity "without pores" describes a category of porosity in which crystals possess lattice voids with no atomic-scale channels.

Although this definition seems counterintuitive, it can be explained when dynamic processes that occur within the crystal are considered. For example, crystals of 5,11,17,23-tetra-*t*-butyl-25,26,27,28-tetramethoxy-2,8,14,20-tetrathiacalix[4]arene were shown to possess small lattice voids of 14, 16 and 36 $Å^3$, however, these crystals possessed no channels leading to the voids. Despite this, the immersion of the crystals in water for 8 hours resulted in the diffusion of water molecules into the seemingly nonporous and hydrophobic lattice guest pockets as confirmed by X-ray analysis.[21]

The surge in interest in MOFs is largely attributed to their porosity and large apparent surface areas.[5] The conventional definition of porosity requires the presence of infinite channels with a typical diameter of 3 – 10 Å in the host framework.[22] In this regard, MOFs have become quite attractive because many of these may have infinite metal-ligand combinations with the rigidity to withstand evacuation.

1.5 Entanglement

Reticular synthesis has allowed for the rational design of MOFs around known structural units. Manipulation of secondary effects, like the ligand length, has increased the potential for synthesising MOFs with higher void space. However, this increases the potential for complex MOF structures becoming further complicated by supramolecular bonding, and more specifically, hydrogen interactions which may promote entanglement or catenation, i.e. where two or more identical frameworks are inter-grown, resulting in a reduction in pore volume.[16,23] Catenated species are intergrown without the ability to be separated without breaking covalent or coordination bonds. Catenation occurs because of the loss in stability with increased pore volume. Compensation for this instability, results in the framework 'self-filling' this space through catenation. The added supramolecular and hydrogen bonding interactions increase stability to the structure at the cost of pore volume.

Two main types of entanglement will be discussed: (i) interpenetration and (ii) polycatenation. Both interpenetration and polycatenation involve the entanglement of 1D, 2D or 3D motifs however, interpenetrated motifs are usually 2D or 3D networks which (a) must be identical motifs with identical

topology, (b) must have a finite number of entangled motifs, (c) the dimensionality of the single framework and final entangled structure must be the same and (d) each single network must be interlaced with all other frameworks of the final structure. Conversely, polycatenated motifs (a) can have the same or different nets that contain closed loops to be interlocked, (b) can have finite or infinite entangled motifs, (c) the resultant polycatenated structure must have higher dimensionality than at least one framework and (d) each motif may be catenated to all, but one of its neighbours.[16,24]

Interpenetration, the most numerous groups, can be based on 1D chains, 2D layers and 3D networks (where dimensionality describes the degree of finite extension of the net). For 1D interpenetration to occur, the complexes must contain rings. Simple chains are entangled in parallel (usually as a result of the rods passing through the centre of the rings) to give new 1D structures.[25] Fan et al. reported a MOF in which 1D chains of $[Zn_2(bib)_2(OAc)_4]\cdot 2H_2O$ (where, bib = 1-bromo-3,5-bis(imidazol-1-ylmethyl)benzene and OAc = acetate anion) are interpenetrated by neighbouring chains through a Br···Br interactions leading to the formation of an infinite 1D pseudo-polyrotaxane.[24]

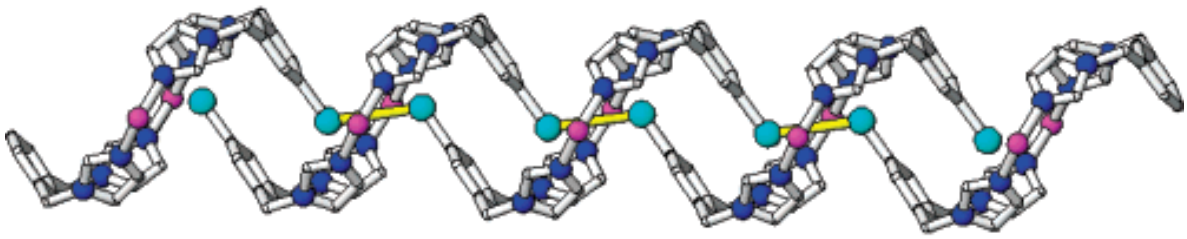

Figure 1.6 Schematic of the 1D pseudo-polyrotaxane formed by Br···Br interactions, indicated in yellow, to form infinite 1D chains.[24]

2D interpenetration is characterised by the presence of interlaced, identical 2D motifs that share the same average plane. Parallel interpenetration may give either a new 2D layered or 3D parallel polycatenated (PCAT) structure while inclined 2D interpenetration gives a 3D inclined polycatenated (ICAT) structure (**Figure 1.7**).

Interpenetration is commonly cited as an obstacle in MOF design, however, some studies have shown that entangled frameworks may still be useful as they offer increased stability to the framework which may aid in sorption and some interpenetrated MOFs have shown applications in things like chemosensing. Sun et al. reported the synthesis of polycatenated MOF $Cu_3(TATB)_2(H_2O)_3$ (where TATB = 4,4',4"-*s*-triazine-2,4,6-triyltribenzoate) in which the MOF still had 74% solvent accessible volume.[26] Takshima et al. reported the use of 2-fold interpenetrated MOF $\{[Zn_2(bdc)_2(dpNDI)].4(DMF)\}_n$ (where bdc = 1,4-benzenedicarboxylate; dpNDI = N,N'-di(4-pyridyl)-1,4,5,8-naphthalenediimide) as a chemosensor. Transformation of the interpenetrated MOF allowed confinement of the guest molecule within the MOF. Enhanced guest-NDI interactions resulted in a luminescent colour dependent on the chemical substituent of the guest.[27]

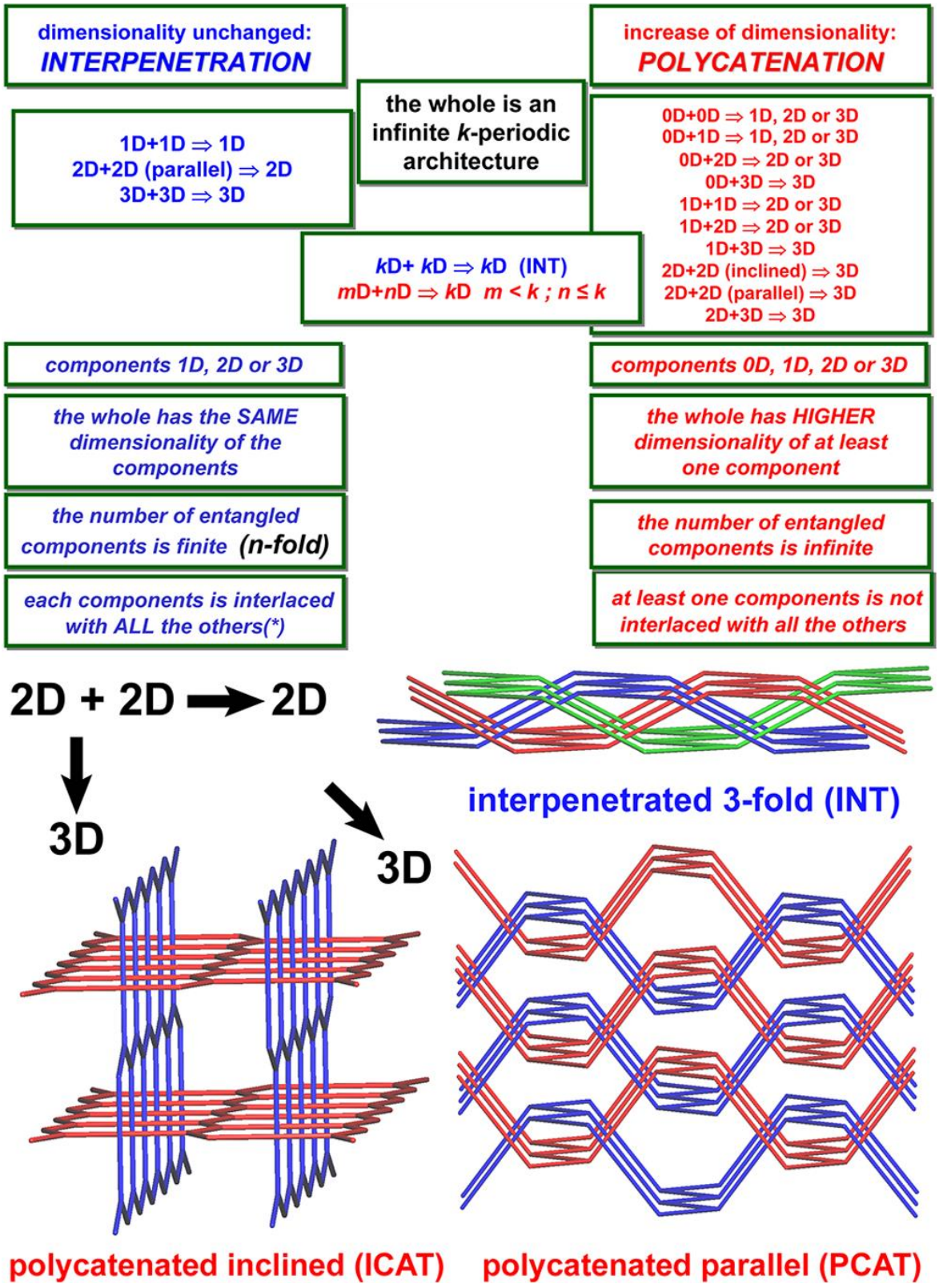

Figure 1.7 Complete scheme of classification of inclined interpenetration and parallel or inclined polycatenation, PCAT or ICAT, respectively in periodic structures.[16]

1.6 Applications

1.6.1 Advantages of Metal-Organic Frameworks over Zeolites

MOFs continue to garner interest for their robust frameworks with uniform voids of high volume and apparent surface areas. Chemists have successfully demonstrated various applications for MOFs in chemosensing, separation of mixtures and gas sorption.[27-32] The gas sorption potential is a particular area of interest with MOFs being compared to other sorbents, such as zeolites, which are often used as molecular sieves. Zeolites are microporous, crystalline, metal-oxide based materials. These structures consist of $TO_{4/2}$ (T = Si, Al, Zn, etc) building units and have been proven to have sorption capabilities.[33] MOFs are arguably preferable over zeolites due to the tunability and uniformity of their pores which improves selectivity. MOFs are also highly crystalline with predictable crystal structures that make them easier to analyse than zeolites. These characteristics have set MOFs apart as having superior applications in separation processes.[34,35]

When comparing the highest CO_2 capacity of selected zeolites against selected MOFs and activated carbon, it was found that the highest performing MOF of the study, MOF-177 far outperformed zeolite 13X and the activated carbon material MAXSORB. At a pressure of 35 bar, zeolite 13X and MAXSORB showed a CO_2 sorption capacity of 7.4 mmol g^{-1} and 25 mmol g^{-1}, respectively. MOF-177 was found to have a sorption capacity greater than 1.5 times that of the other two materials (**Figure 1.8**).[35]

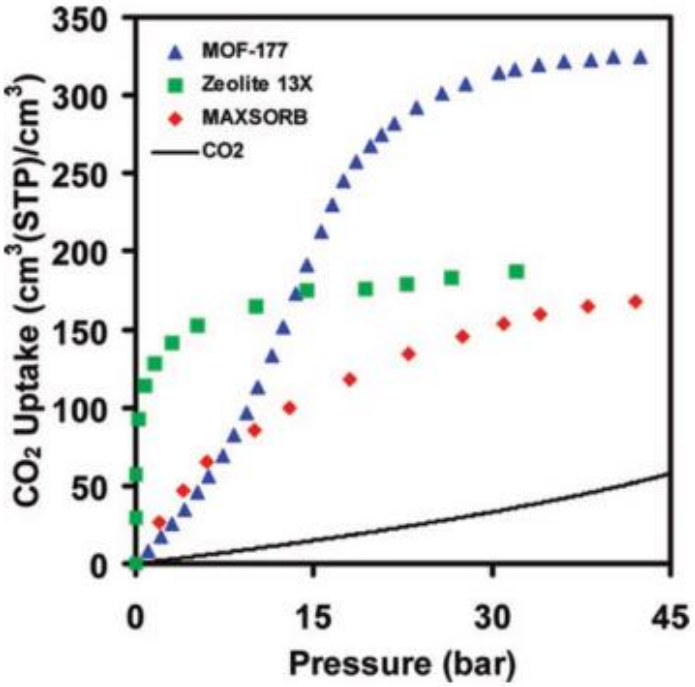

Figure 1.8 Comparison of the CO_2 sorption of MOF-177, zeolite 13X and MAXSORB against pressurised carbon dioxide.[35]

1.6.2 Water Stability of Metal-Organic Frameworks

The ubiquitous nature of water in many chemical processes has made the water stability of MOFs an important thought when considering their potential adsorption applications. Water vapour is prevalent in processes such as the selective carbon dioxide capture in flue gas mixtures (CO_2/N_2 = 85/15) wherein water is a major component (~10%) and most air control problems like the removal of toxic industrial chemicals.[36] The stability of MOFs in water is an important challenge to overcome with more water adsorption isotherm studies being conducted on MOFs. MOFs such as the MIL-100 series of materials have received much attention for their water sorption.[37,38] Recently, Das et al. reported a Co(II) and a Cu(II)-based MOF which were both water stable and showed high selectivity towards carbon dioxide sorption.[39,40] MOF characteristics such as interpenetration, coordinatively unsaturated metal centres and the basicity of ligands are some features that have been associated with adding to the water stability of MOFs.[41]

1.7 Single-crystal-to-single-crystal transformations

Some MOFs can undergo single-crystal-to-single-crystal (SC-SC) transformations, i.e. where the crystal remains intact as the guest moves into and out of the framework.[42-47] By monitoring the structure of the MOF before and after guest evacuation insight into the mechanism of the transformation may be gained. Removal of the guest can be achieved through external stimuli such as heating and monitored through variable temperature single crystal X-ray diffraction. Alternatively, SC-SC transformations can be stimulated through light, solvent exchange or through post synthetic modification of ligands.[48]

Jiang and Peng reported the synthesis of MOF $[Mn_2(4\text{-Apha})_4(H_2O)_2]\cdot 2H_2O$ (1,4-AphaH = 4-aminophenylhydroxamic acid) and its subsequent temperature-induced SC-SC transformation to the dehydrated form $[Mn_2(4\text{-Apha})_2]$.[44] When heated to 393 K, $[Mn_2(4\text{-Apha})_4(H_2O)_2]\cdot 2H_2O$ undergoes a two-step structural transition whereby the coordination number of the Mn(II) ions change from six to five. Thereafter, the Mn(II) ions coordinate to the neighbouring oxygen atoms of the NH-O(1-) groups of the 4-Apha$^-$ ligands. Interestingly, this SC-SC transformation was accompanied with a change in crystal colour (brown to dark brown) with dehydration and *in situ* PXRD patterns could be used to confirm the transition to the anhydrous form. Both structures were characterised and confirmed to have similar magnetic properties.

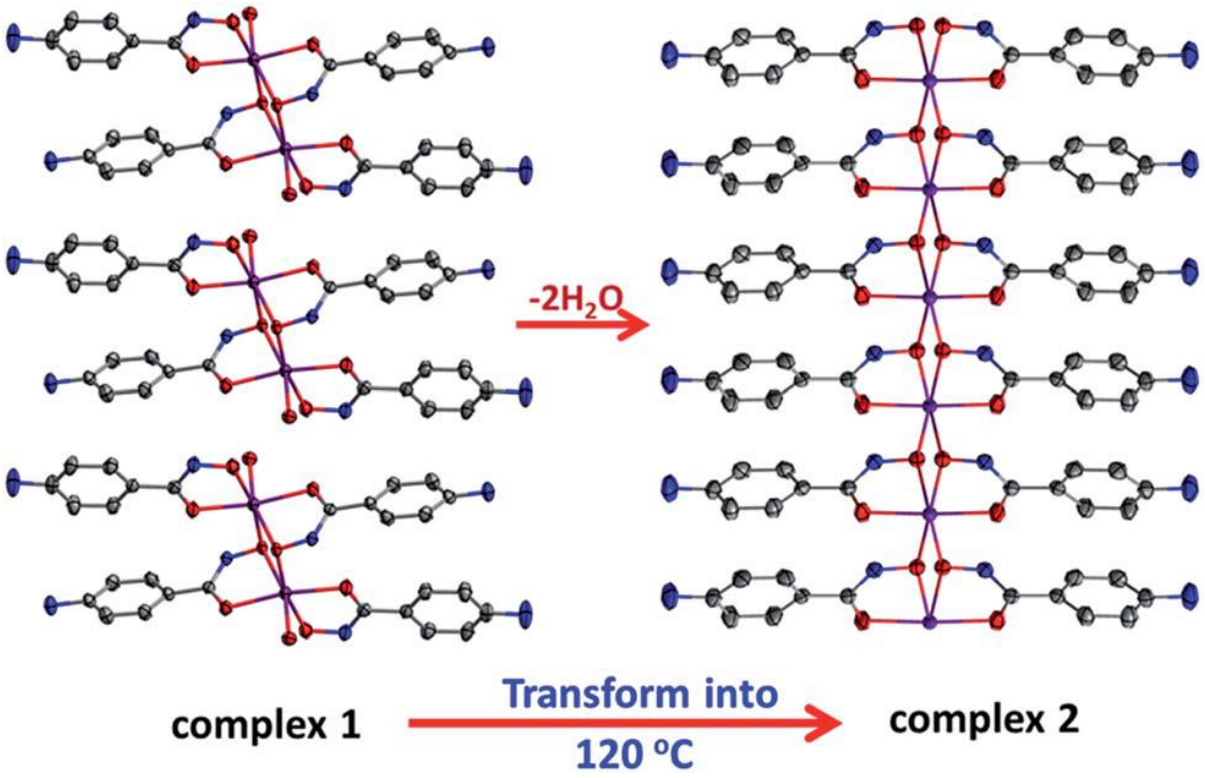

Figure 1.9 Structure transformation diagram of temperature-induced SC-SC transformation of $[Mn_2(4\text{-Apha})_4(H_2O)_2]\cdot 2H_2O$ (left) to dehydrated $[Mn_2(4\text{-Apha})_2]$ (right).[44]

1.8 Mixed-Ligand Metal-Organic Frameworks

1.8.1 Mixed-Ligand Synthetic Strategy

Through careful selection of ligands, it is possible to synthesise MOFs of increased topological complexity and varied, desirable properties. Mixed-ligand strategy has been proposed as an improvement on MOF design because it offers the possibility of the tuning of pore sizes, as ligands of various sizes can be used in the synthesis, allowing further tailoring of properties. Mixed-ligand MOFs are MOFs which have two different ligands incorporated. For coordination to occur, the first ligand must have significant synergistic contributions to enhance the ligation of the other ligand which adds further synthetic complications.[49,50]

1.8.2 Ligand Characteristics

In the design of mixed-ligand systems, ligand coordination modes must be taken into consideration. Mixed-ligand MOFs can be classed according the Lewis acid/base classification of their comprising ligands, prior to their coordination. This classification falls into either acid-acid, base-base or acid-base systems.[50] Mixed-ligand systems in which the ligands are of the same type, i.e. base-base or acid-acid, are rarer. This can be attributed to the competing ligation pathways which inhibits the ability of both ligands coordinating to the same metal. Base-base systems are especially rare for this reason and because of the need for counter ions, since the ligands are neutral, which may block channels thereby precluding 'activation' of the MOF. One example of such a system, $[Co(bpy)(bimb)(SCN)_2]_n$, (where bpy = 4,4'-bipyridine, bimb = 1,4-bis(imidazol-1-yl)-butane and SCN = thiocyanate) is a rarer example of a base-base mixed-ligand MOF system.[51]

There are more reported cases of acid-acid mixed-ligand MOF systems. One such example is one in which terephthalic acid (H_2tp) and 1,3,5-tris(4-carboxyphenyl)benzene (H_3tcb) are combined with Zn(II) to produce $[Zn_4O(tp)(tcb)_{4/3}]_n$.[52] It was found that making slight variations in the concentrations of either acid ligand resulted in different single-ligand MOFs being synthesised. At higher concentrations of H_2tp, only MOF-5, which has tp as a ligand, was synthesised in the system. The converse was true when H_3tbc was present at a higher concentration in the reaction medium where MOF-177, comprising only of tcb as a ligand, was the only MOF synthesised then. When the molar ratios of H_2tp:H_3tcb were between 3:1 and 1:1, $[Zn_4O(tp)(tcb)_{4/3}]_n$ was synthesised, thereby clearly demonstrating the competitive nature of mixed-ligand systems in which the ligands have similar coordination functionalities.[50,52-54]

The acid-base mixed ligand assembly strategy has been the most successful in terms of these ligand classifications. Acids and bases are widely regarded as reliable partners as they can compensate charge balance, coordination deficiency and the weak interactions concurrently.[50]

Ligands containing disulfoxide, dithioether and diphosphine have seldom been used due to the practical limitations of finding co-ligands. Bipyridyl and polycarboxyl compounds are widely regarded as the most

reliable acid-base combinations for mixed-ligand MOF synthesis. This combination of types of ligands offer coordination polymer design considerable diversity of structures.[55-58]

1.8.1.1 Carboxylate Ligands

Polycarboxylate ligands offer a high level of chemical and thermal stability. The carboxylic acid groups have multiple coordination and bridging modes that stabilise frameworks and offer structural complexity to the synthesised MOFs.[59,60] Aromatics are often preferred as they tend to form robust structures with limited conformational flexibility in the structures.

In this work, 1,3-benzenedicarboxylic acid or isophthalic acid (H_2**ia**) and two derivatives, 5-nitro-1,3-benzenedicarboxylic acid or 5-nitroisophthalic acid (H_2**nia**) and 5-methoxy-1,3-5-benzenedicarboxylic acid or 5-methoxyisophthalic acid (H_2**mia**) (**Figure 1.10**) were the chosen polycarboxylic acid ligands.

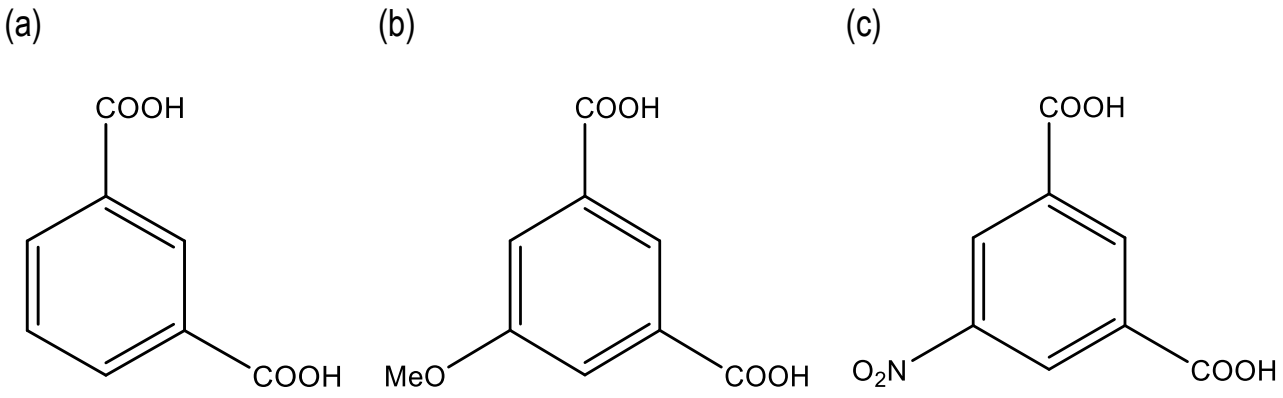

Figure 1.10 Chemical structure of (a) isophthalic acid, (b) 5-methoxyisophthalic acid and (c) 5-nitroisophthalic acid.

H_2**ia** and its derivatives demonstrate multiple coordination modes, much like 1,3,5-benzenetricarboxylic acid, a rigid, planar molecule that has become popular as a ligand in MOF synthesis, which make it ideal for the construction of MOFs with a diversity in coordination modes (**Figure 1.11**).[61]

(a)

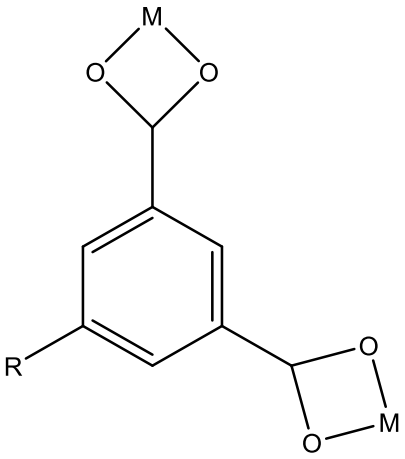

(b)

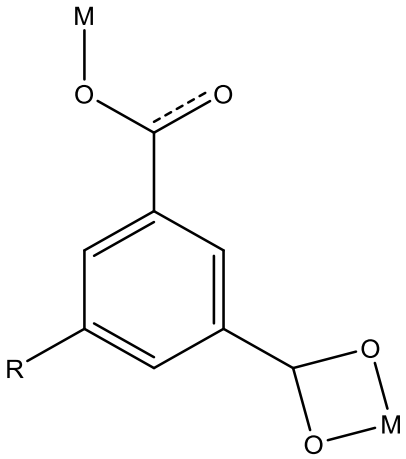

(c)

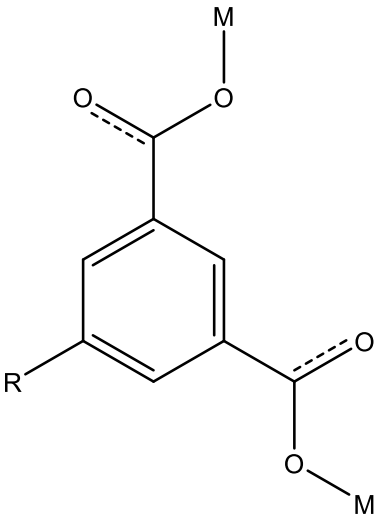

(d)

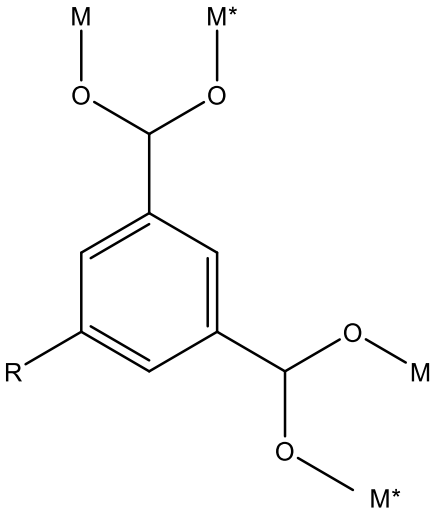

Figure 1.11 The bonding modes of polycarboxylates, where R = -H (H_2**ia**), -MeO (H_2**mia**) or -NO_2 (H_2**nia**) are (a) – (c) various combinations of mono- and bidentate coordination modes and (d) bridging two metal centres in a bridging bidentate fashion. M and M* indicate different types of metal centres.[61]

1.8.2.2 Pyridyl Ligands

Pyridyl ligands with two 4-nitrogen donors are useful Lewis base ligands in the synthesis of mixed-ligand MOFs as the pyridyl ligand can form pillars between the coordination sheets. Use of flexible spacer ligands may promote generation of distorted frameworks which may lead to dynamic MOFs that can shrink and expand, i.e. 'breathe', with external stimuli. Pyridyl ligands also allow independent tuning of the pores independent of the first ligand.[62] The danger of using very long bipyridyl ligands is that of increased probability of catenation which may ultimately negatively impact the pore volume.[23,50] However, catenation could increase the stability of the MOF as there is the potential for stabilization through hydrogen bonding interactions.

In this work, two flexible bipyridyl ligands, namely 1,2-bis(4-pyridyl)ethane (**bpe**) and 1,2(4-pyridyl)ethylene (**bpee**) were the chosen bipyridyl ligands (**Figure 1.12**).

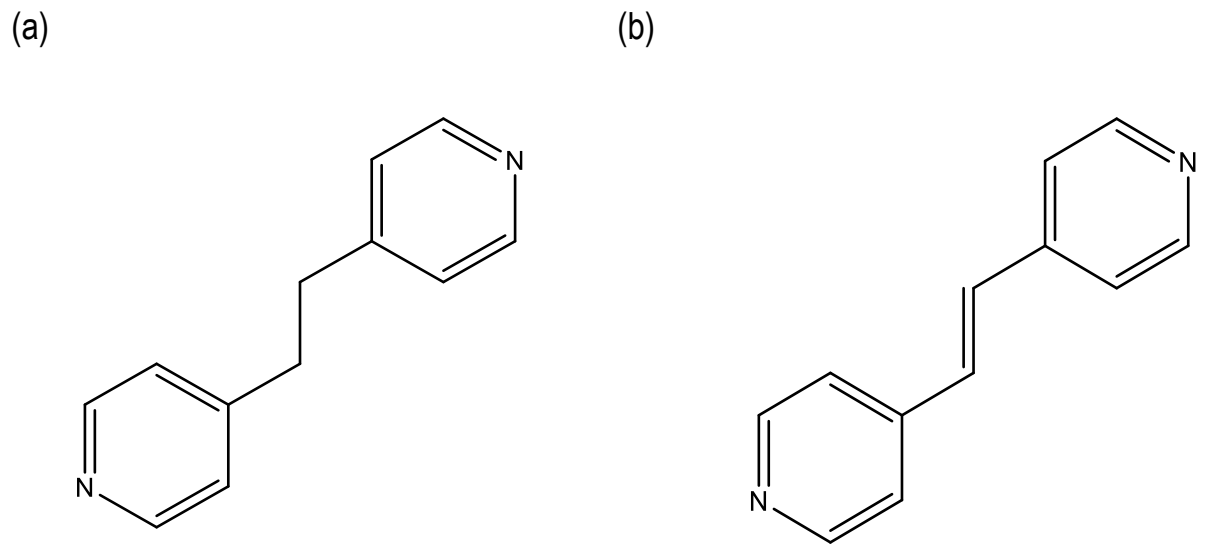

Figure 1.12 Chemical structure of (a) 1,2-bis(4-pyridyl)ethane and (b) 1,2-bis(4-pyridyl)ethylene.

1.9 Motivations

In recent years, the study of MOFs has garnered increased interest with mixed-ligand strategy being employed for its rational design and positive implications for pore size tunability. The acid-base strategy has garnered positive results with polycarboxylate and bipyridyl ligands considered reliable pairs for their contribution to the charge balance (**section 1.8.1.1**) and potential for adjustments based on the spacer and substituent effects (**section 1.4.3**). In this study, Cd(II) and Zn(II) metal ions were selected for the potential range of coordination numbers and geometries (tetrahedral, pentagonal bipyramidal, trigonal bipyramidal or octahedral) they offered. The coordination numbers typically seen for Cd(II) and Zn(II) are 4 – 7 where Cd(II) assumes coordination of 6 more easily than Zn(II) owing to its larger size. Polycarboxylic acid and bipyridyl base mixed ligand MOFs have been widely reported and offer many advantages to frameworks as discussed in **section 1.8.1.1** and **1.8.1.2.**

1.10 Objectives

The objectives of this study were:

a. Prepare isoreticular mixed-ligand MOFs based on polycarboxylate acid and bipyridyl base systems
b. To characterise synthesised compounds by single and powder X-ray diffraction including variable-temperature single crystal and powder X-ray diffraction techniques
c. To assess the thermal stability and behaviours of compounds through thermogravimetric analysis, differential scanning calorimetry and hot stage microscopy
d. To assess the liquid and gas sorption capabilities of synthesised MOFs

Chapter 2:

Experimental

The organic ligands and metal salts used in the synthesis of materials are identified in this chapter. Synthetic and analytical techniques, including their instrumentation for X-ray diffraction, hot stage microscopy, differential scanning calorimetry, thermogravimetric analysis and gas sorption used in the characterisation of the MOFs are discussed.

2.1 Starting Materials

The organic ligands which have been repeated for ease of reference (**Figure 2.1**), isophthalic acid (99% purity), 5-methoxyisophthalic acid (purity 97%), 5-nitroisophthalic acid (99% purity), 1,2-bis(4-pyridyl)ethane (99% purity) and 1,2-bis(4-pyridyl)ethylene (97% purity) were purchased from Sigma Aldrich (Germany). The metal salt, $Zn(NO_3)\cdot 6H_2O$ was purchased from Sigma Aldrich (Germany) and the metal salt, $Cd(NO_3)\cdot 4H_2O$, was purchased from Riedel-de Haën AG. (Germany). The solvents used for synthesis were, Milli-Q water, *N,N'*-dimethylformamide (≥99% purity) and diethyl ether (99% purity), which were purchased from Sigma Aldrich (Germany) and ethanol (min 99% purity), which was purchased from Merck. All materials were used as received without further purification.

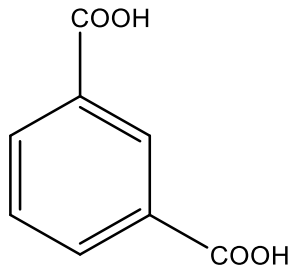

isophthalic acid (H_2**ia**)

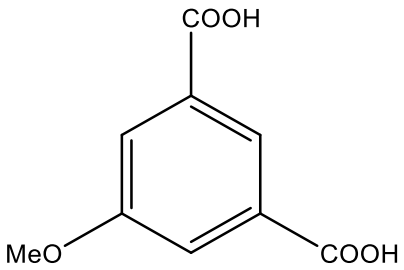

5-methoxyisophthalic acid (H_2**mia**)

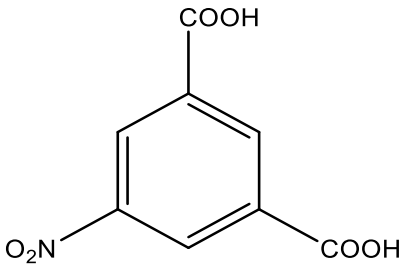

5-nitroisophthalic acid (H_2**nia**)

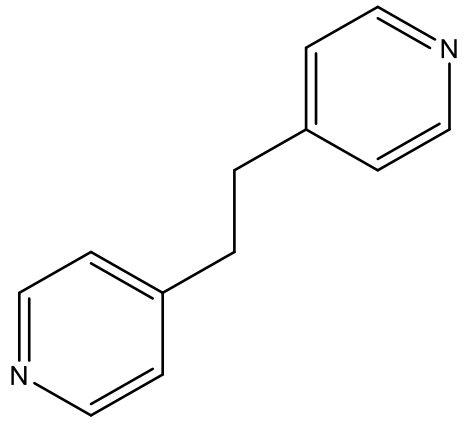

1,2-bis(4-pyridyl)ethane (**bpe**)

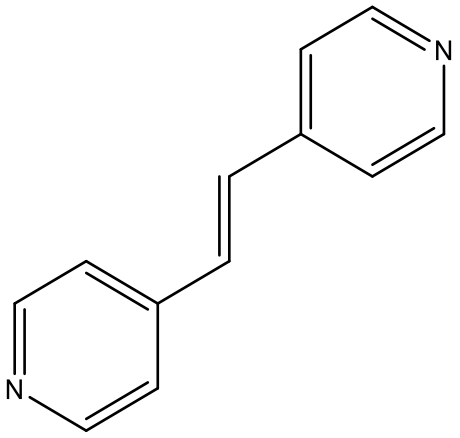

1,2-bis(4-pyridyl)ethylene (**bpee**)

Figure 2.1 Chemical structures of organic ligands used.

2.2 General Synthetic Procedure

2.2.1 Solvothermal Experiments

Solvothermal techniques were used to synthesis the MOFs discussed. The synthesis involved dissolving the metal salt in water and separately dissolving the organic ligands in solvents before combining all the solutions together. The total solution was stirred, then heated in an oven before being slow cooled to yield crystals. The full synthetic details for respective compounds are expanded upon in the respective chapter.

2.2.2 Liquid-Assisted Grinding Experiments

The synthesis of the solvothermal products was attempted through liquid-assisted grinding (LAG) experiments to produce high yield compound rapidly. Metal salt and the organic ligands were ground with a mortar and pestle in 1:1:1 molar ratios. The solvent combination of DMF/H_2O, in equal volumes, was added dropwise to assist the grinding. The sample was ground for 20 mins after which powder X-ray diffraction analysis was used to assess the success of the LAG experiments.

2.3 Structural Analysis

2.3.1 Single Crystal X-ray Diffraction

A suitable single crystal was selected and removed from the mother liquor for single crystal X-ray diffraction (SCXRD) in order to prevent solvent loss, the crystal was covered in Paratone N oil and placed on a nylon loop that was attached to a rigid mounting. The loop, with the crystal attached, was then placed on the goniometer head under a cold stream of nitrogen gas. Data collections were then carried out using a Bruker KAPPA APEX II DUO diffractometer. Samples were irradiated with graphite monochromated MoKα radiation of wavelength λ = 0.71073 Å. The X-rays were produced by a Bruker K780 generator operated at 50 kV and 30 mA. The Oxford Cryosystems-700 unit was used to maintain the low temperatures for data collections by streaming N_2 gas at a rate of 20 cm^3 min^{-1}.

Unit cell refinement and data reductions were performed using the program SAINT-Plus.[63] Thereafter, the intensity data was scaled and Lorentz-polarisation and absorption effects were corrected for using the SADABS program.[64] The space group was suggested by the program XPREP which was also used to prepare the SHELXT[65] input files used for structure solution. The space group was confirmed from studies of the systematic absences in LAYER[66] found in the X-ray data which were then compared to systematic absences of known space groups. SHELXT solves the structure in *P*1 and suggests a space group after structure solution. In all cases, this was consistent with the space groups suggested by XPREP and inspection of the reciprocal lattice layers. Metal ions, being of highest electron density, as well as most non-hydrogen atoms were placed automatically by SHELXT while non-hydrogen atoms were, in general, placed in the first electron density map and refined in SHELXL-2018/3[67] using the full-matrix least squares on F^2 method. After all the atoms had been placed and found to have well-behaved isotropic temperature factors, the structures were refined anisotropically. Where necessary (often due to disorder) DFIX restraints were used to ensure ideal bond lengths (±0.005 Å). In some cases, idealised coordinates and geometrical constraints were generated for phenyl groups by performing an AFIX 66 rigid group refinement. Where necessary, restraints were applied to restrain atoms to be approximately isotropic. The restraint SIMU was applied to restrain the U_{ij} (anisotropic displacement parameters) components of neighbouring atoms to be approximately equal, while the restraint ISOR was applied to prevent atoms from becoming 'non-positive-definite' and to restrain atoms with effective standard deviations so that their U_{ij} components approximate isotropic behaviour while allowing the corresponding isotropic U to vary.[68] The enhanced rigid bond restraint, RIGU, provides a more realistic description of the atomic thermal motion in anisotropic refinement.[69] All hydrogen atoms were placed using riding models. Further details about refinement and hydrogen placement for each structure can be found in the relevant chapters. The programs X-SEED and/or OLEX2 were used as the interface for the SHELXT and SHELXL programs.[70,71]

Idealised, calculated patterns were calculated using the program Mercury.[72] This calculated pattern could then be used to compare the calculated patterns to experimental powder X-ray diffraction (PXRD) patterns. Thereby, it could be confirmed whether the single crystal was representative of the bulk material. The PXRD pattern of subsequently produced sample could also be compared to the calculated pattern to confirm that the desired compound had been reproduced.

2.3.2 Powder X-ray Diffraction

Powder X-ray diffraction (PXRD) and variable-temperature powder X-ray diffraction (VT–PXRD) data collections were measured using a Bruker D8 Advance X-ray diffractometer using CuKα radiation (λ = 1.5406 Å). PXRD samples were scanned over a 2θ range of 4 – 40° with a step size rate of 0.015° sec^{-1} over approximately 20 mins unless otherwise stated in the relevant chapter. The X-ray generator was set to a current flow of 40 mA and voltage of 30 kV.

VT–PXRD was used to identify any phase changes with heating and to determine the effect of desolvation on sample crystallinity. Temperature ranges were determined according to desolvation mass loss events as observed in TGA experiments. VT–PXRD samples were scanned over a 2θ range of between 4 – 45° with temperature step rate of 0.5 ˚C min^{-1} unless otherwise stated in the relevant chapters.

2.4 Hirshfeld Surface Analysis

Hirshfeld surface analysis was conducted using CrystalExplorer and was used to understand the nature and type of intermolecular interactions involved in selected crystal structures.[73,74] The Hirshfeld surface is defined according to the formulae:

$$\omega_A(r) = \frac{\sum_{A \epsilon molecule} \rho_A(r)}{\sum_{A \epsilon crystal} \rho_A(r)} = \frac{\rho_{promolecule}(r)}{\rho_{procrystal}(r)}$$

where $\rho_A(r)$ is the spherically arranged density around the nucleus defined as A, whilst the promolecule and procrystal refer to the sums of the density over the entire molecule and crystal, respectively. The

parameter d_{norm} is the normalised distance based on d_e and d_i, the distances from the Hirshfeld surface to the outside and inside of the surface, respectively.

The normalization equation is:

$$d_{norm} = \frac{d_i - r_i^{vdW}}{r_i^{vdW}} + \frac{d_e - r_e^{vdW}}{r_e^{vdW}}$$

where r_i^{vdW} and r_e^{vdW} are the van der Waals radii of the atoms on the inside and outside of the surface, respectively. The type of contact is dependent on the sign of d_{norm} where a negative value indicates an intermolecular contact longer than the sum of the atoms' van der Waals radii (blue areas on the Hirshfeld surface) and a positive value indicates an intermolecular contact shorter than the sum of the atoms' van der Waals radii (red areas on the Hirshfeld surface). The Hirshfeld surface is used to derive the 2D fingerprint plot that is used to summarise the type and percentage contribution of intermolecular contacts experienced by the molecule of interest. Both the Hirshfeld surface and the corresponding 2D fingerprint of a given molecule are dependent on its unique crystal environment.

The local shape of the surface of a molecule may also yield some chemical insight. The curvedness of a surface is a function of the root-mean-square where flat surfaces have a low curvedness while sharp surfaces have a high curvedness. The curvature of a surface is calculated according to the function:

$$C = \frac{2}{\pi} ln \sqrt{\frac{\kappa_1^2 + \kappa_2^2}{2}}$$

The shape index is a qualitative measure of a shape of a Hirshfeld surface that allows the identification of complementary "stamp" and "mould" pairs, two regions in the surface where the shape index differs only by a sign, i.e. the surface has the same pattern but in opposite colours.

The shape index is calculated according to the formula:

$$S = -\frac{2}{\pi} arctan \frac{\kappa_1 + \kappa_2}{\kappa_1 - \kappa_2}$$

Where κ_1 and κ_2 are the calculated principle curvatures. Shape and curvedness indices help identify flat regions where C-H···π or π···π interactions may be present.

2.5 Thermal Analysis

To determine thermal properties such as desolvation, melting, phase changes and decomposition of the samples, three thermal analysis techniques were utilised, namely: thermogravimetric analysis (TGA), differential scanning calorimetry (DSC) and hot stage microscopy (HSM),

2.5.1 Thermogravimetric Analysis

A TGA Q500 Thermogravimetric Analyzer was used to determine the mass change of samples as a function of temperature. This provides a means to measure the solvent loss and to determine the thermal stabilities and decomposition by recording temperatures of the desolvation of the MOFs. Sample of masses ranging between 0.8 and 5 mg were dried on filter paper before TGA analysis was performed. A heating rate of 10 ˚C min^{-1} was used from at least 291 K up to temperature of approximately 723 K. All samples were run under a dry nitrogen gas flow of 60 mL min^{-1} to remove liberated gaseous products. Results obtained from TGA were analysed using Universal Analysis and TRIOS software.[75,76]

2.5.2 Differential Scanning Calorimetry

A TA DSC25 Differential Scanning Calorimeter from TA instruments was used to measure the difference in thermal energy inputs required to maintain the sample and empty reference pans at the same temperature. This was done to observe thermal events such as melting, desolvation (displayed as endothermic troughs), recrystallizations (displayed as exothermic peaks) and solid-solid phase transitions (endothermic troughs or exothermic peaks) as well as to determine decomposition temperatures, indicated by complex overlaps of endothermic troughs and exothermic peaks, and the thermal stability of

the samples. All samples, ranging in mass from 0.8 to 2.5 mg, were placed in aluminium pans with vented lids to match those of the reference pan. Temperatures of the measurements ranged from 303 K to 623 K. The maximum temperature for the DSC analysis was determined according to the temperature of crystal decomposition observed during HSM. Samples were not taken to full decomposition in order to prevent spillage onto the thermocouple. A heating rate of 10 ˚C min^{-1} was used for all analyses with a dry nitrogen flow of 40 mL min^{-1}. Results, as obtained through DSC, were analysed using TRIOS Software.[76]

2.5.3 Hot Stage Microscopy

HSM was used to visually track thermal events such as desolvation, melting, phase transitions and decompositions. In this study, this technique was primarily used to observe desolvation and decomposition events. The temperatures at which these events occurred were noted and tentatively used to anticipate the temperatures at which the same events would occur in TGA and DSC. The temperatures at which the same thermal events occurred differed from equipment to equipment due to differences in equipment geometries. For HSM analysis, samples were placed on a cover slip under silicone oil to more clearly observe changes resulting from solvent loss (indicated by bubbling). The sample was viewed with a Nikon SMZ-10 stereoscopic microscope, fitted with a Linkam THMS600 hot stage. This hot stage setup was linked to a Linkam TP92 temperature control unit. A heating rate of 10 ˚C min^{-1} was used. Crystals were heated up to 673 K or until crystals began to turn brown indicating decomposition. Thermal events were recorded using a Sony Digital Hyper HAD colour video camera and images were captured using the Soft Imaging System program analySIS.[77]

2.6 Sorption Studies

2.6.1 Liquid Sorption Studies

The porosity of some of the synthesised compounds was investigated through liquid sorption experiments. Desolvated samples, were exposed to solvents of varying polarities according to the Burdick and Jackson solvent polarity index which measures the degree to which the solvent interacts with various

polar tests solutes.[78] Solvent exposure included placing samples in a small vial containing approximately 2 mL of solvent for 24 h or 48 h. Solvents selected for this study, in order of decreasing polarity index, include water (10.2), DMF (6.4), ethanol (5.2), methanol (5.1), chloroform (4.1) and benzene (2.7).[78]

2.6.2 Gas Sorption Studies

Gas sorption capability studies were conducted for nitrogen at 77 K, hydrogen at 77 K, carbon dioxide at 195 K, and 273 – 298K and water vapour at 298 K. The Micromeritics 3flex Surface Characterization Analyzer, was used to carry out the gas sorption experiments. Samples, of mass ranging from 80 – 200 mg, were first treated using a Micromeritics Flowprep. The samples were first heated to 333 K with a constant nitrogen gas flow over the sample for at least 8 hours to evacuate as much solvent as possible before *in situ* heating under vacuum on the 3Flex analyser. Specific temperatures of desolvation were determined *via* TGA and are stated in relevant chapters. A Micromeritics water bath was used to achieve the temperatures from 273 K – 298 K, whilst a liquid nitrogen bath was used for experiments at 77 K. A mixture of acetone and dry ice was used to make a slurry at 195 K for experiments conducted at this temperature. The absolute pressure limit of the equipment is 1000 mmHg. Consequently, no sorption could be measured at higher absolute pressures. Sorption isotherms were analysed using the 3Flex Micromeritics software.

2.7 Computer Packages

The Cambridge Structural Database (CSD), accessed *via* ConQuest, was used to determine the novelty of synthesised structures.[4,5] Molecular structure and crystal packing images were generated using MERCURY and POV-RAY.[72,79] PLATON was used to determine molecular parameters.[80] The program MERCURY was used to calculate the free void space present in the host framework using a probe radius of 1.2 Å and a grid spacing of 0.7 Å.

2.8 Appendices

Results obtained from thermal experiments (TGA & DSC) and data from single crystal X-ray diffraction studies can be found in the appendices.

Table 2.1 Crystallographic data files to be found in the appendices

File Extensions	Contents
.hkl	Reflection data
.cif	Crystallographic information data
.res	SHELX coordinate data
.lis	PLATON geometrical analysis data
.pdf	CheckCif report
.fcf	Observed and calculated intensities

Chapter 3:

Zn Metal-Organic Frameworks

Two, novel Zn mixed-ligand MOFs with formula [Zn(μ_2-**ia**)(μ_2-**bpe**)]$_n$·nDMF (**1**) and [Zn(μ_2-**mia**)(μ_2-**bpe**)]$_n$·nDMF (**2**) were synthesised. Both compounds **1** and **2** exhibit **sql**, 2-periodic, 2D net coordination layers. The compounds were characterised fully through X-ray diffraction (SCXRD, VT–SCXRD, PXRD and VT–PXRD) and thermal analysis (HSM, DSC and TGA). The chapter is divided according to each characterisation technique wherein the analytical results for each compound are discussed. The compounds were tested for their gas and water vapour sorption capabilities to determine their porosity. Once desolvated, both compounds absorbed water from the atmosphere. Dehydration and rehydration for both compounds occurred *via* a reversible single-crystal-to-single-crystal transformation.

3.1 Synthesis

3.1.1 Preparation of [Zn(μ_2-ia)(μ_2-bpe)]$_n$·*n*DMF (1)

3.1.1.1 Solvothermal Synthesis

The metal salt, $Zn(NO_3)_2{\cdot}6H_2O$ (100 mg, 0.34 mmol), was dissolved in 3 mL H_2O and then stirred for 10 min. The organic ligands, 1,2-bis(4-byridyl)ethane (62 mg, 0.34 mmol) and isophthalic acid (56 mg, 0.34 mmol) were dissolved in a solvent mixture of 4 mL *N*,*N'*-dimethylformamide (DMF) and 2 mL diethyl ether then stirred for 10 min. The solution of organic ligands was mixed with the metal salt solution, in a 1:1:1 (L1:L2:M^{2+}) molar ratio, with continuous stirring for a further 10 min followed by the addition of 0.2 μl H_2SO_4 (3 M) to aid dissolution. The resulting, clear solution was sealed in a 25 mL vial then heated in an oven at 90 °C for 48 h. Thereafter, the solution was cooled slowly to 30 °C at a rate of 10 °C per hour. Clear, block shaped crystals were obtained within 10 days.

3.1.1.2 Liquid-Assisted Grinding

Liquid-assisted grinding (LAG) was explored as a means of rapid, high yield synthesis of **1**. The starting materials were identical to those of the solvothermal synthesis. The organic ligands, H_2**ia** and **bpe** were combined with 5 mg of the metal salt, $Zn(NO_3)_2{\cdot}6H_2O$ in a 1:1:1 (L1:L2:M^{2+}) molar ratio and kneaded for 20 min with a mortar and pestle. A mixture of DMF and H_2O in a 1:1 volume ratio was added dropwise to assist the grinding process. Comparison of the PXRD pattern of the LAG product and the calculated pattern of **1** (**Figure 3.1**) revealed that although there was some peak overlap at 10.6° and in the 18.0° – 19.5° 2θ region, peaks present in the calculated pattern of **1** at 7.5°, 9.9°, 11.6°, 12.4° and 13.7° are not present in the LAG product PXRD pattern.

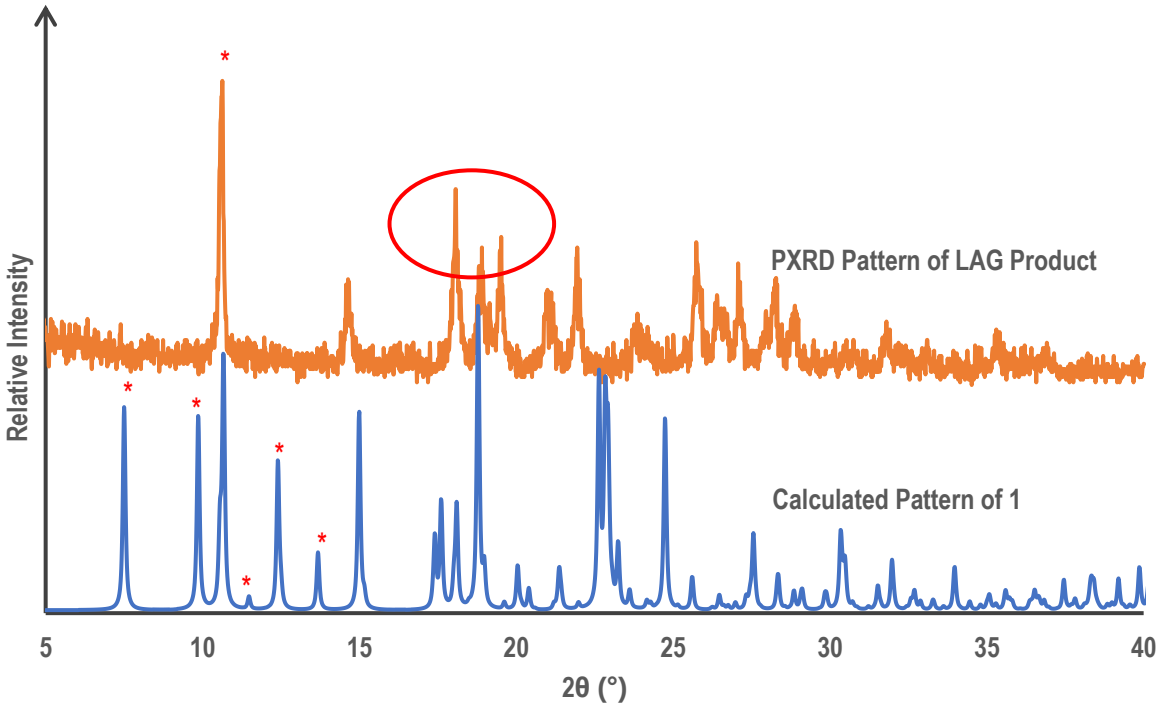

Figure 3.1 PXRD pattern of the LAG product and calculated pattern of **1**. Red asterisks and circles indicate selected peaks and peak regions specified in **section 3.1.1.2**.

Comparison of the LAG product PXRD pattern to those of the starting materials (**Figure 3.2**) revealed that the LAG product was not a mixture of the starting material as new peaks could be seen at 10.6°, 14.6°, 18.1° and 25.8° which indicates that the LAG product is a new product. Evaluation of the patterns of the LAG product and calculated patterns of **1** indicate that the LAG product may be **1** but that the reaction had not reached completion, or that some of the peaks are missing due to amorphization. However, as this product did not completely match the calculated pattern, solvothermal techniques were deemed a more reliable synthetic technique to produce **1** in bulk.

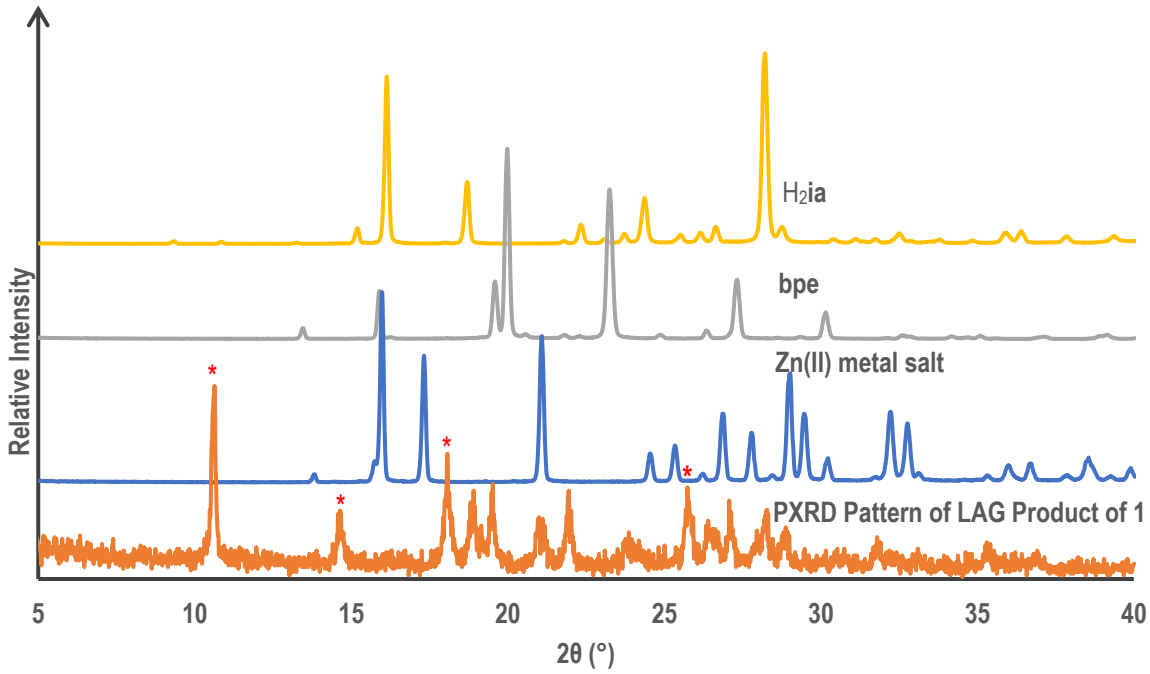

Figure 3.2 PXRD patterns of the LAG product and starting materials for **1**. Red asterisks indicate selected peaks as specified in **section 3.1.1.2**.

3.1.2 Preparation of [Zn(μ_2-mia)(μ_2-bpe)]$_n$·*n*DMF (2)

3.1.2.1 Solvothermal Synthesis

The preparation of **2** followed a similar procedure to that of compound **1**. The metal salt, $Zn(NO_3)_2 \cdot 6H_2O$ (100 mg, 0.34 mmol), was dissolved in 3 mL H_2O and then stirred for 10 min. The organic ligands, 1,2-bis(4-byridyl)ethane (62 mg, 0.34 mmol) and 5-methoxyisophthalic acid (66 mg, 0.34 mmol) were dissolved in 6 mL of *N,N'*-dimethylformamide (DMF) then stirred for 10 min. The solution of organic ligands was mixed with the metal salt solution, in a 1:1:1 ($L1:L2:M^{2+}$) molar ratio, with continuous stirring followed by the addition of 0.2 μl H_2SO_4 (3 M) to aid dissolution. The resulting clear solution was heated in an oven at 90 °C for 48 hours. Clear, block shaped crystal were obtained after 48 h. Thereafter, the solution was cooled slowly to 30 °C at a rate of 10 °C per hour.

3.1.2.2 Liquid-Assisted Grinding

LAG experiments were also conducted to determine if mechanochemical techniques could successfully produce **2**. The synthesis was identical to that described in **3.1.1.2** except that H_2**mia** was used instead of H_2**ia**. Comparison of the PXRD pattern of the LAG product and the calculated pattern of **2** revealed that the starting materials became quite amorphous upon grinding. Although some peaks could be seen in the PXRD pattern of the LAG product, these were poorly overlapped with those of the calculated pattern. The few sharp peaks in the LAG product pattern at 8.0°, 20.3° and 27.1° did not appear in the calculated pattern of **2**.

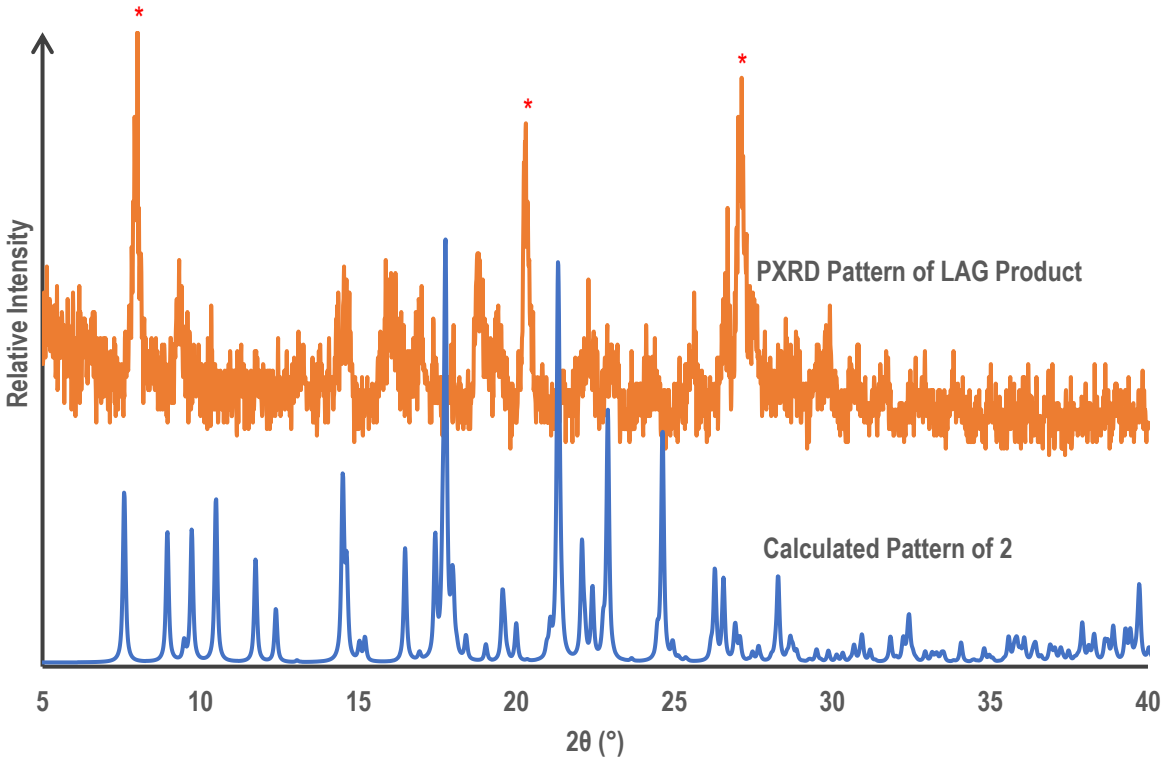

Figure 3.3 PXRD pattern of the LAG product and calculated pattern of **2**. Red aterisks indicate selected pesk as specified in **section 3.1.2.2**.

The powder pattern of the LAG product was compared to the PXRD pattern of the starting materials for **2**. New peaks at 8.0° and 20.3° 2θ in the PXRD pattern of the LAG product, when compared to those in

the PXRD patterns of the starting materials, suggested the possibility that the LAG product is a new MOF. However, some overlap with the H_2**mia** PXRD pattern in the 16.0° – 17.9° 2θ region suggests that the LAG product contains some unreacted starting material. The amorphous nature of the LAG product indicates that it is not the same as the desired crystal product. Solvothermal synthesis was deemed a more reliable method to produce **2** in bulk, therefore further analysis of the LAG product was not conducted.

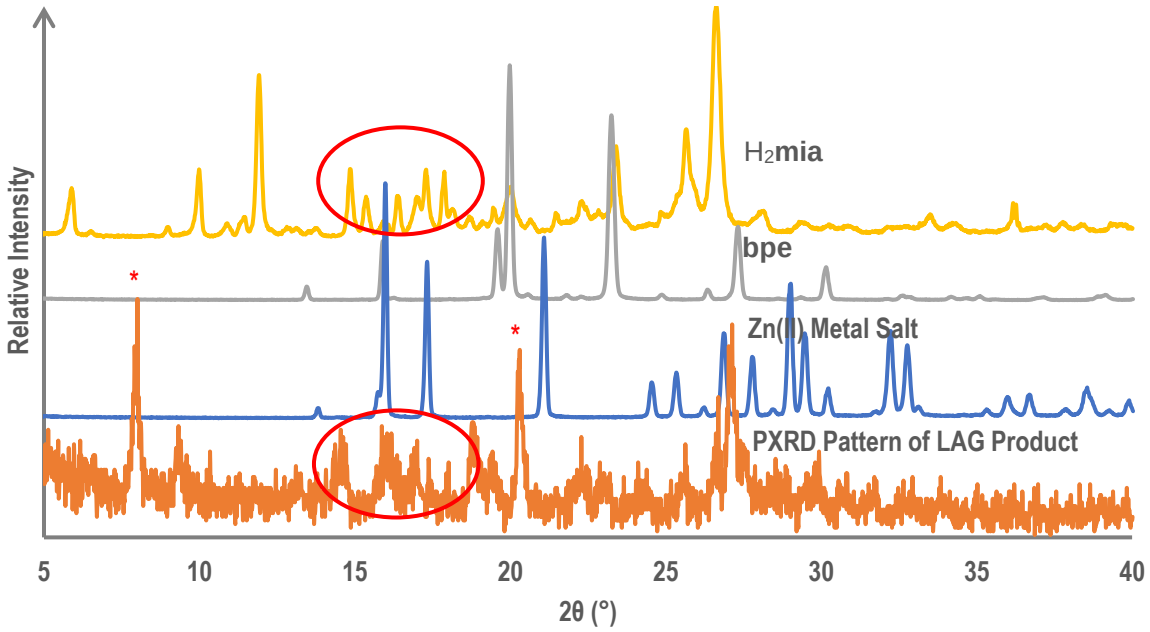

Figure 3.4 PXRD pattern of the LAG product and starting materials for **2**. Selected peaks and peak regions of interest, as specified in **section 3.1.2.2**, are indicated with red asterisks and circles.

3.2 Single Crystal X-ray Diffraction

3.2.1 Structures Solution and Refinement

A crystal of each compound was selected from the mother liquor and placed on the Bruker DUO Apex II CCD diffractometer for data collections. The data collection procedure is outlined in **section 2.3.1**. The full SCXRD collection and unit cell data are presented for both compounds in **Table 3.1**.

Table 3.1 Crystal and refinement data for MOFs **1** and **2**

	Compound 1	**Compound 2**
	As-synthesised	**As-synthesised**
Asymmetric Unit Formula	$C_{23}H_{23}N_3O_5Zn$ (**1**)	$C_{24}H_{25}N_3O_6Zn$ (**2**)
Formula Weight/g mol^{-1}	486.81	516.84
Temperature/K	100 (2)	100 (2)
Crystal System	Orthorhombic	Orthorhombic
Space Group	*Pbca*	*Pbcn*
***a* / Å**	10.1799(8)	23.2656(12)
***b* / Å**	17.9193(17)	10.1523(5)
***c* / Å**	23.548(2)	19.7050(10)
***α* / °**	90	90
***β* / °**	90	90
***γ* / °**	90	90
Volume/Å^3	4295.6(6)	4654.3(4)
Z	8	8
ρ_{calc}/g cm^{-3}	1.505	1.475
μ/mm^{-1}	1.185	1.101
***F*(000)**	2016	2144
2θ range for data collection/°	3.46 to 61.264	3.502 to 52.982
Index Ranges	-14 ≤ h ≤ 14, -25 ≤ k ≤ 25, -33 ≤ l ≤ 33	-29 ≤ h ≤ 29, -12 ≤ k ≤ 12, -24 ≤ l ≤ 24
Reflections collected	151995	66730
Independent reflections	6627 [R_{int} = 0.0903, R_{sigma} = 0.0296]	4817 [R_{int} = 0.0395, R_{sigma} = 0.0168]
Data/restraints/parameters	6627/0/291	4817/0/310
Goodness of fit of F^2	1.055	1.023
Final R indexes [I ≥ 2σ (I)]	R_1 = 0.0381, wR_2 = 0.0978	R_1 = 0.0261, wR_2 = 0.0695
Final R Indexes [all data]	R_1 = 0.0487, wR_2 = 0.1039	R_1 = 0.0321, wR_2 = 0.0728
Largest diff. peak/hole/e Å^{-3}	0.69/-0.65	0.33/-0.34

3.2.2 Structure description

Both compounds crystallise in the orthorhombic crystal system in the space groups *Pbca* and *Pbcn* for **1** and **2**, respectively. The asymmetric unit (ASU) of both compounds consist of a Zn(II) cation coordinating to one neutral 1,2-bis(4-pyridyl)ethane (**bpe**) ligand and one fully deprotonated isophthalate ligand (**ia**) and 5-methoxyisophthalate ligand (**mia**) for **1** and **2**, respectively. Both ASUs contain a fully occupied, uncoordinated DMF molecule.

The coordination sphere around the Zn cation of **1** and **2** is a distorted tetrahedron. The Zn cation is singly coordinated to the nitrogen of the **bpe** and an oxygen on each carboxylate group of the **ia** and **mia** ligand in **1** and **2**, respectively. The 2+ charge on the metal cations is balanced by the 2- charge on the deprotonated **ia** and **mia** ligands in the respective systems. The metal-coordinating atoms for **1** are O1, $O4^{ii}$, N1 and $N2^{iii}$, where ii = 1+x, y, z and iii = x, 1/2-y, -1/2+z. The metal-coordinating atoms for **2** are O4, $O1^{ii}$, N1 and $N2^{iv}$, where ii = x,1+y, z and iv = 1/2+x,3/2-y,1-z. The angles present around the Zn cation range from 99.65(5)° – 116.47(6)° and 99.42(5)° – 120.03(5)° for **1** and **2**, respectively. These angles indicate a distorted tetrahedral geometry and is confirmed by the τ_4 parameter (as defined by Yang, Powell and Houser) being 0.91 for both compounds. Ideal square planar and tetrahedral geometries have τ_4 values of 0.00 and 1.00, respectively. [81]

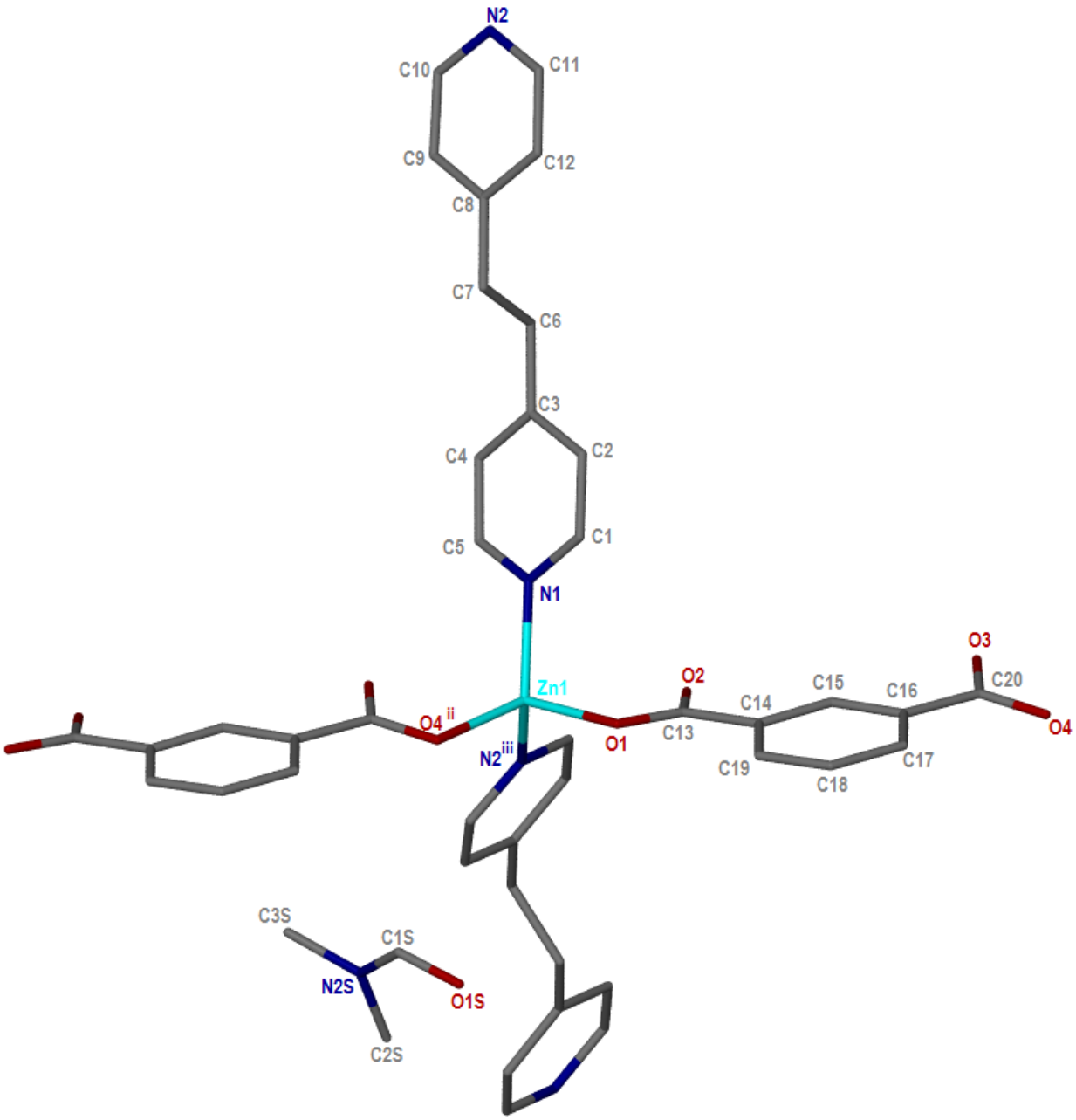

Figure 3.5 Full coordination sphere around the Zn(II) ion of **1**. Hydrogen atoms have been omitted for clarity.

Table 3.2 Summary of bond lengths involving atoms coordinated to Zn metal cation of **1**

Bond	Length (Å)
Zn–N1	2.0321(15)
Zn–N2^{iii}	2.0508(17)
Zn–O1	1.9751(13)
Zn–O4^{ii}	1.9760(13)

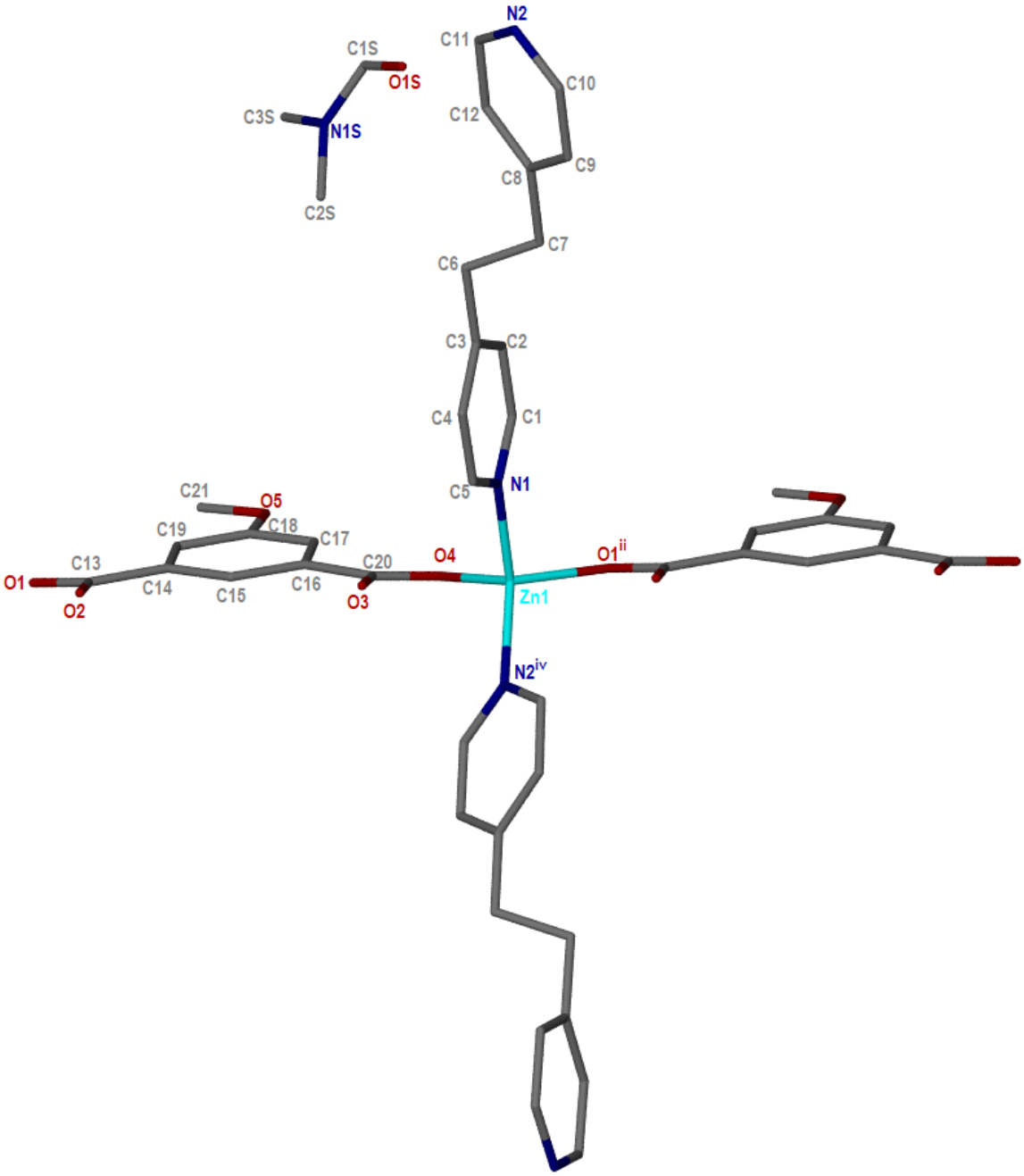

Figure 3.6 Full coordination sphere around the Zn(II) ion of **2**. Hydrogen atoms have been omitted for clarity.

Table 3.3 Summary of bond lengths involving atoms coordinated to Zn metal cation of **2**

Bond	Length (Å)
Zn–N1	2.0229(13)
Zn–N2^{iv}	2.0252(15)
Zn–O1^{ii}	1.9773(12)
Zn–O4	1.9853(11)

3.2.3 Crystal Packing

The extended frameworks of the compounds are also similar as each compound extends in 2 dimensions with the **bpe** extending the framework along the longest axis, 23.548 Å in **1** and 23.2656 Å in **2**, and the **ia** and **mia** extending the frameworks along the shortest axis, 10.1799 Å in **1** and 10.1523 Å in **2,** (**Figure 3.7**). A single framework is interpenetrated with the neighbouring framework to form a 2-fold interpenetrated bilayer. Neighbouring bilayers are interdigitated along the 17.9193 Å (**1**) and 19.7050 Å (**2**) axes with DMF solvent molecules contained in channels along the 10.1799 Å axis (**1**) and 10.1523 Å (**2**) axis (**Figure 3.8**).

(a) (b)

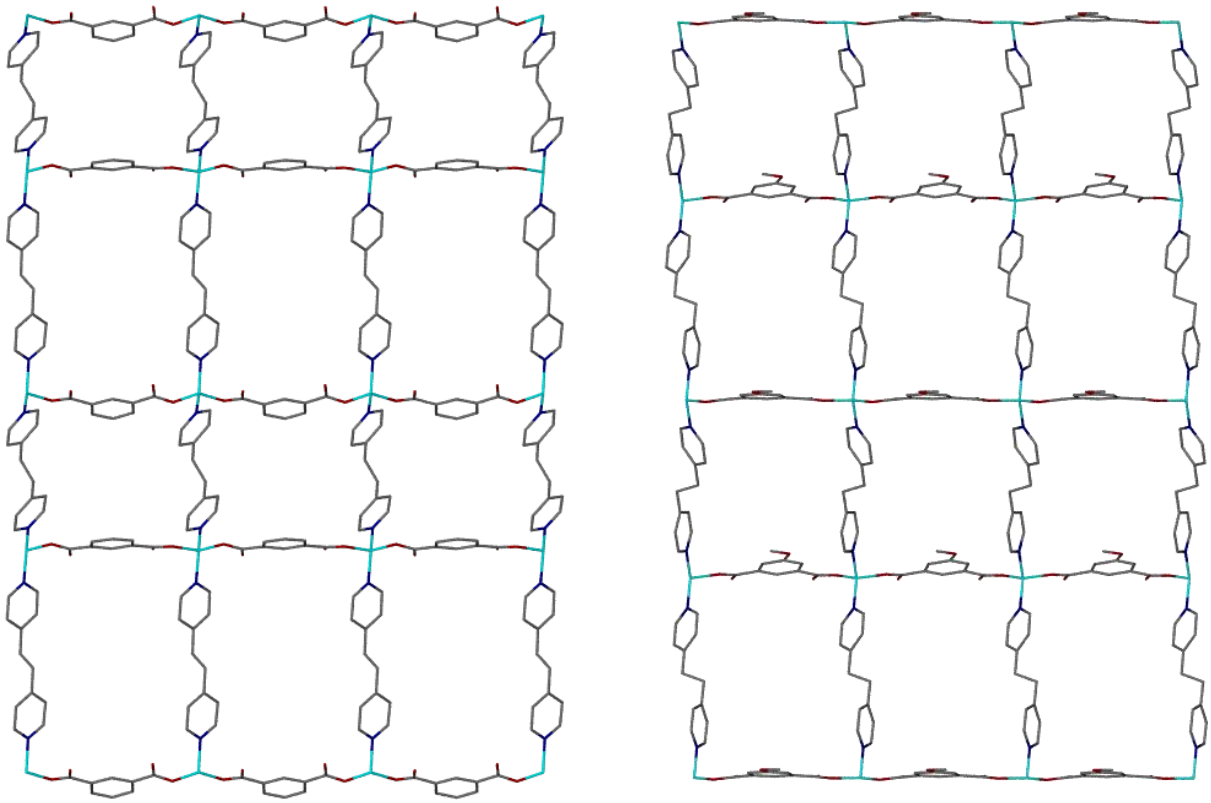

Figure 3.7 Sql motif of (a) **1** and (b) **2** to show extension of frameworks along **bpe** ligation and along **ia** and **mia** ligation in **1** and **2**, respectively.

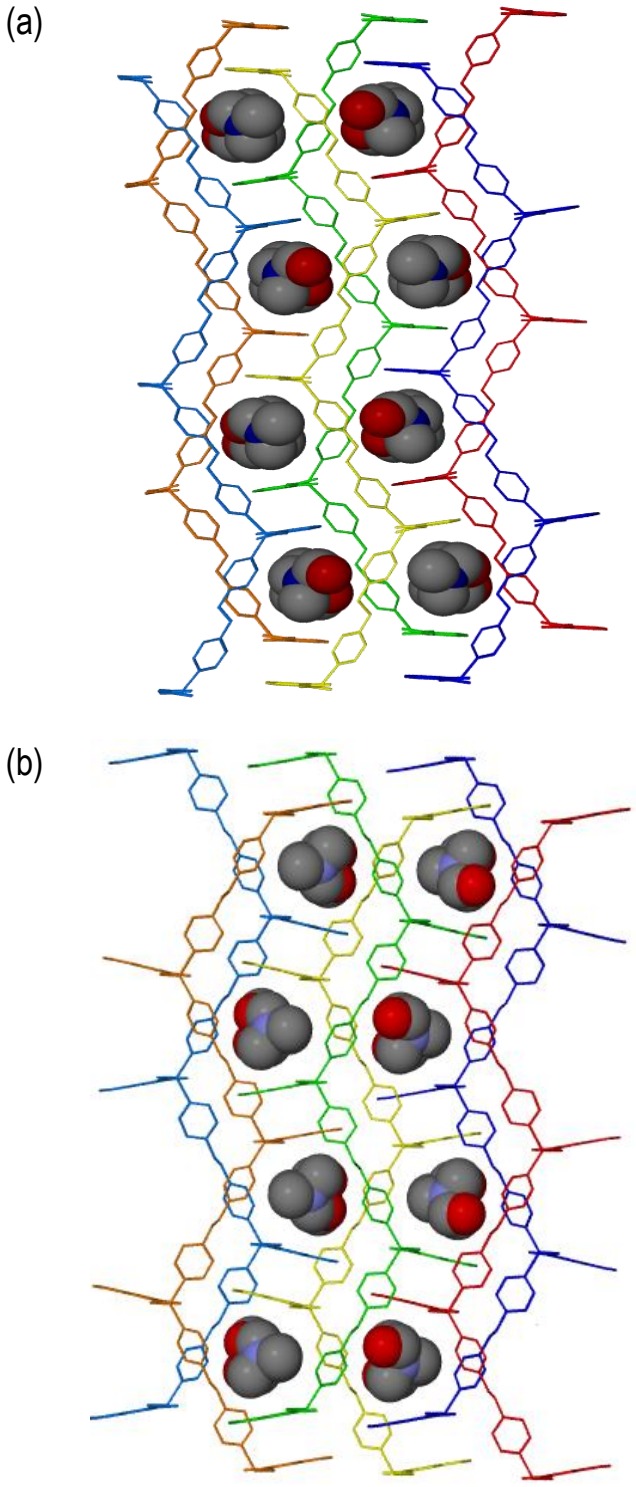

Figure 3.8 Packing diagram of (a) **1** and (b) **2** showing interpenetration of neighbouring frameworks (shown in stick model) with DMF (shown in space-fill model) contained in channels along the 10.1799 Å axis (**1**) and 10.1523 Å (**2**) axis.

The metal ions and centroids of the aromatic **ia** and **mia** rings were taken as nodes for the net for a simplified view (**Figure 3.9**). It was revealed that both compounds **1** and **2** consist of **sql** nets which are 2-periodic, 2D bilayers as described in a review by Carlucci, Proserpio and Blatov.[16]

(a)

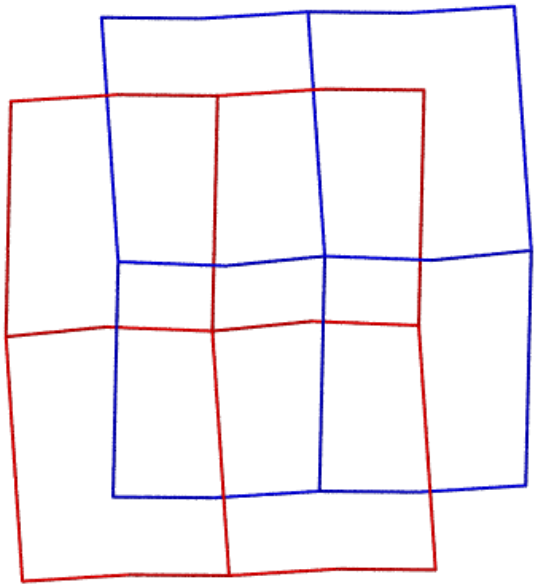

(b)

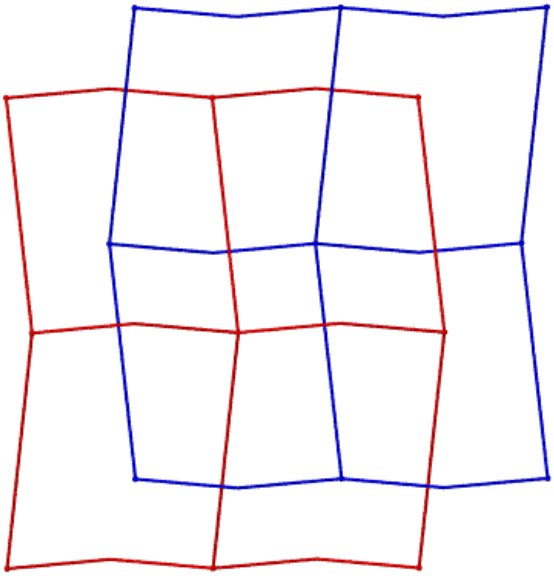

Figure 3.9 Sql lattice motif of adjacent bilayers of compound (a) **1** and (b) **2** along the 17.9193 Å and 19.7050 Å axes in **1** and **2**, respectively.

(a)

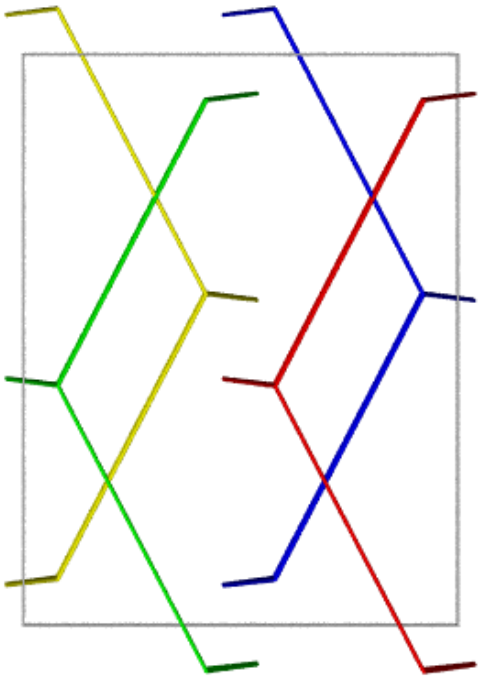

(b)

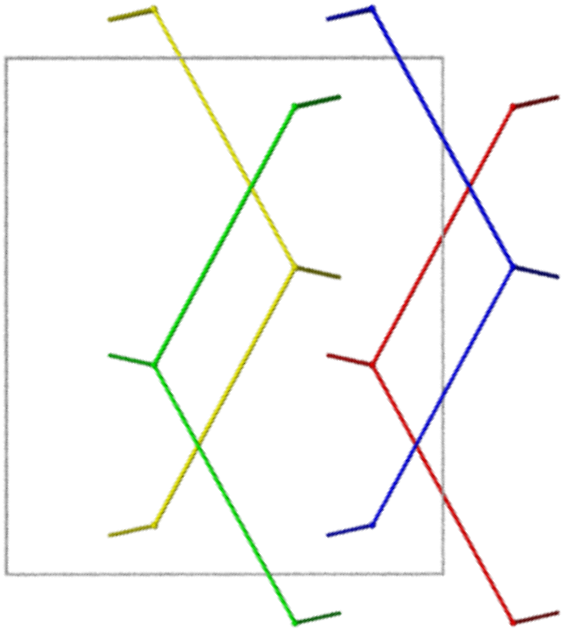

Figure 3.10 Node simplified side view of bilayers of (a) **1** and (b) **2** along the 10.1799 Å axis in **1** and 10.1523 Å axis in **2**.

Channels are formed down the shortest 10.1799 Å axis and 10.1523 Å axis in **1** and **2**, respectively, which are occupied by DMF (**Figure 3.8**). In the program Mercury, the DMF solvent molecules were artificially removed and a probe of radius of 1.2 Å was used to calculate the remaining potential void space per unit cell (**Figure 3.11**). The calculated void space was 18.6% (801 $Å^3$) and 18.3% (851 $Å^3$) for **1** and **2**, respectively.

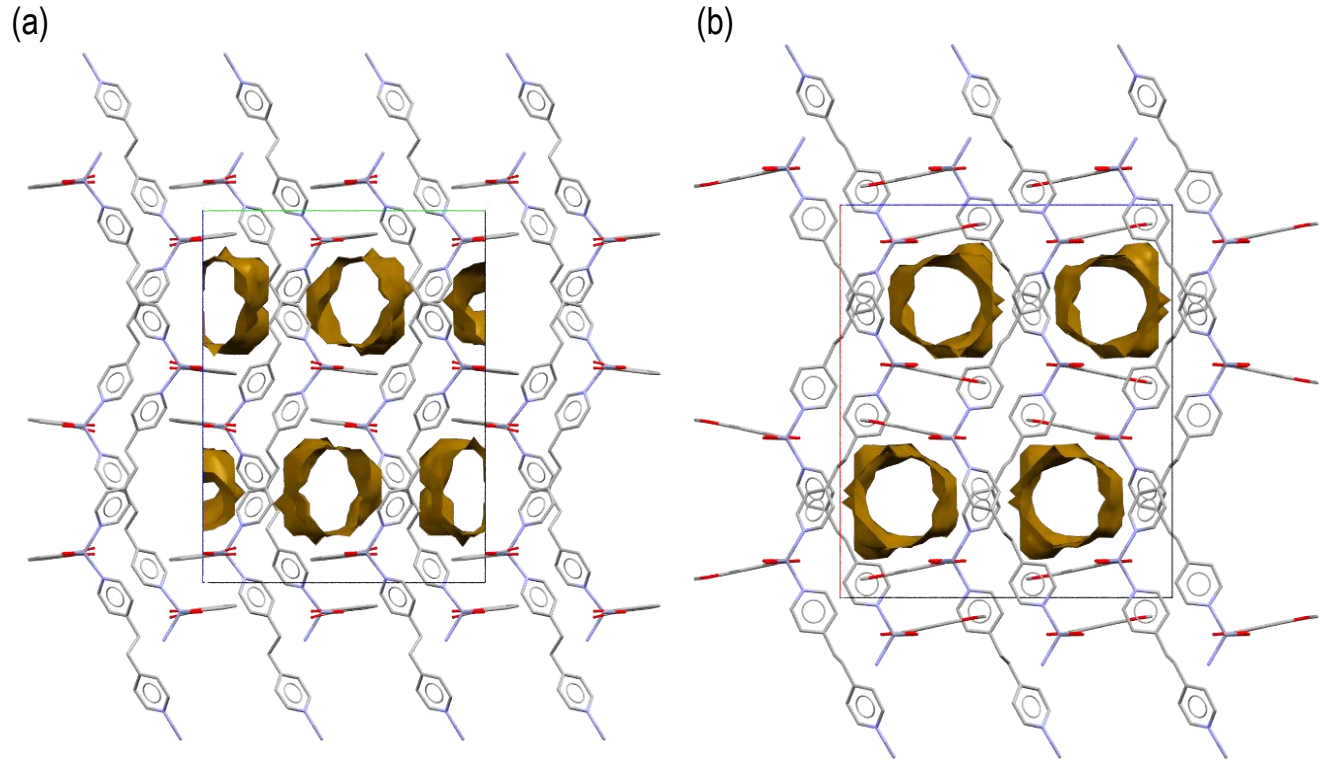

Figure 3.11 Crystal packing of (a) **1** and (b) **2** showing isolated channel voids along the *a*-axis and *b*-axis, respectively (DMF solvent molecules have been artificially removed).

3.3 Desolvation Studies

3.3.1 Variable-Temperature Powder X-Ray Diffraction Studies

The VT–PXRD pattern at 303 K showed a good match to the calculated pattern of **1** (**Figure 3.12**). Peaks seen in the calculated pattern at 7.5°, 9.8°, 12.4°, 14.9° and 17.6° – 20.5° 2θ matched those seen in the 303 K pattern at 7.3°, 9.6°, 12.1°, 14.8° and 17.2° – 20.4° 2θ. There is a peak, indicated with a blue asterisk at 11.4° 2θ in the calculated pattern that did not appear in the experimental VT–PXRD patterns and a double peak at 10.5° and 10.6° 2θ in the calculated pattern that appeared as several peaks in the 10.2° – and 10.4° 2θ range in the 303 K – 498 K VT–PXRD patterns indicated with an arrow above the 498 K PXRD pattern. Overall, there was a good match between the VT–PXRD patterns and the calculated pattern that shows that the selected single crystal was representative of the bulk material and that **1** retains crystallinity with desolvation up to 498 K. Note that the peak seen in the variable-temperature patterns at ~4.5° is the result of the VT–PXRD stage and will been ignored in all VT–PXRD studies.

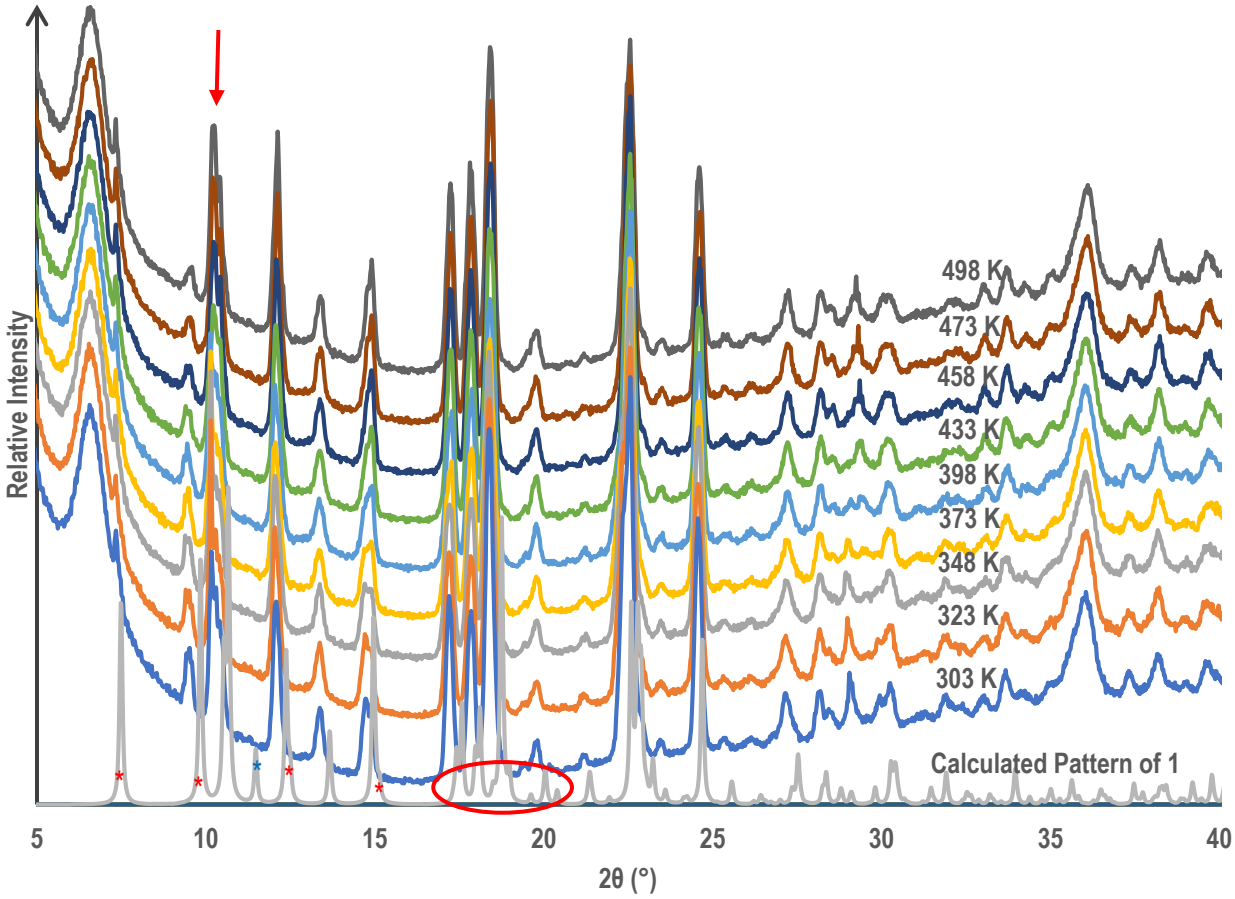

Figure 3.12 VT–PXRD patterns against calculated pattern for **1** in temperature range 303 – 498 K. Asterisks, circles and arrow indicate peaks specified in **section 3.3.1**.

The VT–PXRD pattern of **2** at 303 K shows a good match to that of the calculated pattern (**Figure 3.13**). Peaks at 7.6° – 10.5°, 11.7°, 12.4°, 14.5° – 15.3°, 16.4° and 17.7° – 18.4° 2θ in the calculated pattern match with peaks at 7.6° – 10.4°, 11.6°, 12.3°, 14.3° – 15.2°, 16.2° and 17.7° – 18.0° 2θ in the 303 K VT–PXRD pattern. There are some differences in the 303 K pattern as the peak at 7.6° has a shoulder at 7.5° as well as the peak 8.7° which has a shoulder at 8.6°. These shoulders are not present in the calculated pattern at corresponding peaks. Overall, the PXRD pattern at 303 K was a good match for the calculated pattern of **2** indicating that the single crystal selected was representative of the bulk material. The PXRD patterns at elevated temperatures show that the sample retains crystallinity with desolvation up to 528 K.

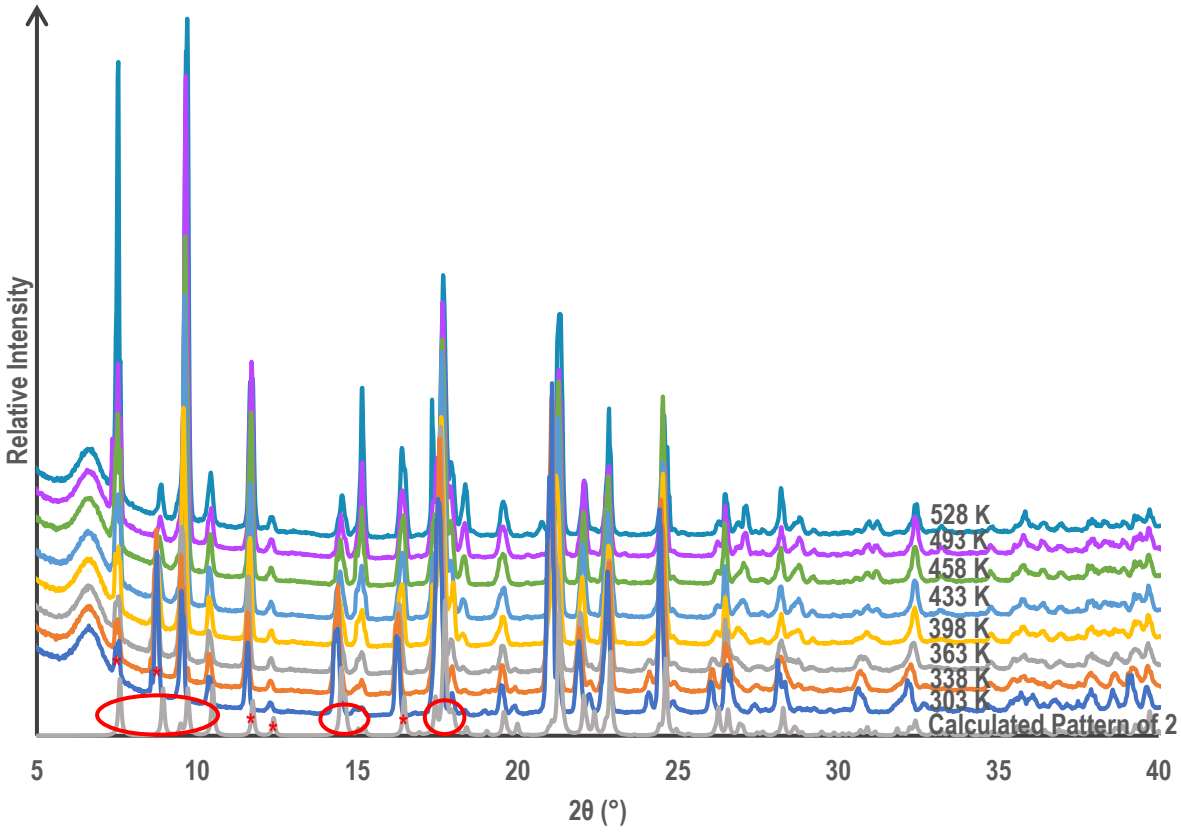

Figure 3.13 VT–PXRD patterns against calculated pattern for **2** in temperature range 303 – 528 K. Red asterisks and circles indicate selected peaks and peak ranges as specified in **section 3.3.1**.

3.3.2 Thermal Analysis

3.3.2.1 Thermogravimetric and Differential Scanning Calorimetry Analysis

Thermogravimetric analysis (TGA) and differential scanning calorimetry (DSC) were employed to investigate the thermal stability of **1** and **2**. Both compounds were confirmed to be highly thermally stable up to high temperatures. The TGA thermogram of **1** (**Figure 3.14**) shows a gradual, one-step mass loss of 13.72% in the temperature range of 292 K – 558 K, representing the loss of one DMF molecule (calculated 14.91%). Structural decomposition is indicated by the remainder of the TGA thermogram. The DSC thermogram for **1** shows a broad endotherm of 136.04 J g^{-1} with an onset temperature of 340 K and a peak temperature at 407 K corresponding to desolvation. This broad peak is followed by a sharp

endotherm of enthalpy 55.76 J g^{-1} with an onset of 569 K and a peak of 575 K which corresponds with the onset of decomposition in the TG analysis.

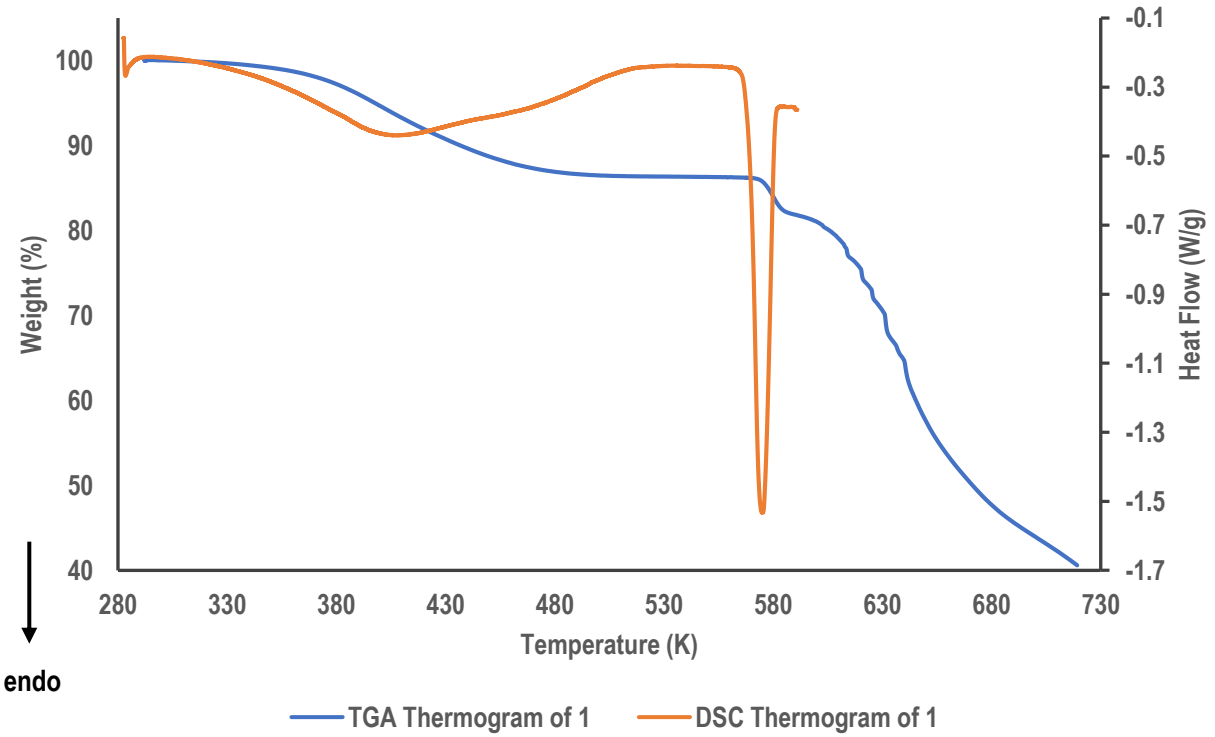

Figure 3.14 Overlay of the TGA (blue) and DSC (orange) thermograms for **1**.

Similarly, the TGA thermogram of **2** (**Figure 3.15**) showed a gradual, one-step mass loss of 13.62% in the range 290 K – 540 K, corresponding to the loss of one DMF molecule from the ASU (calculated 14.47%). As in **1**, this mass loss was followed by the multi-step decomposition event for the remainder of the TG analysis. The DSC for **2** shows two overlapping endothermic events of 163.67 J g^{-1} consisting of a broad peak with a peak temperature of 414 K followed by another endothermic peak with a peak temperature of 497 K. This endothermic event, that corresponds to the solvent loss event seen in the thermogram, indicates that the desolvation event for **2** is more complex than for **1**. A second, sharper endotherm of 67.75 J g^{-1} occurs at onset temperature of 552 K and peak temperature of 560 K that corresponds with the multi-step decomposition process seen in TGA in the same temperature range.

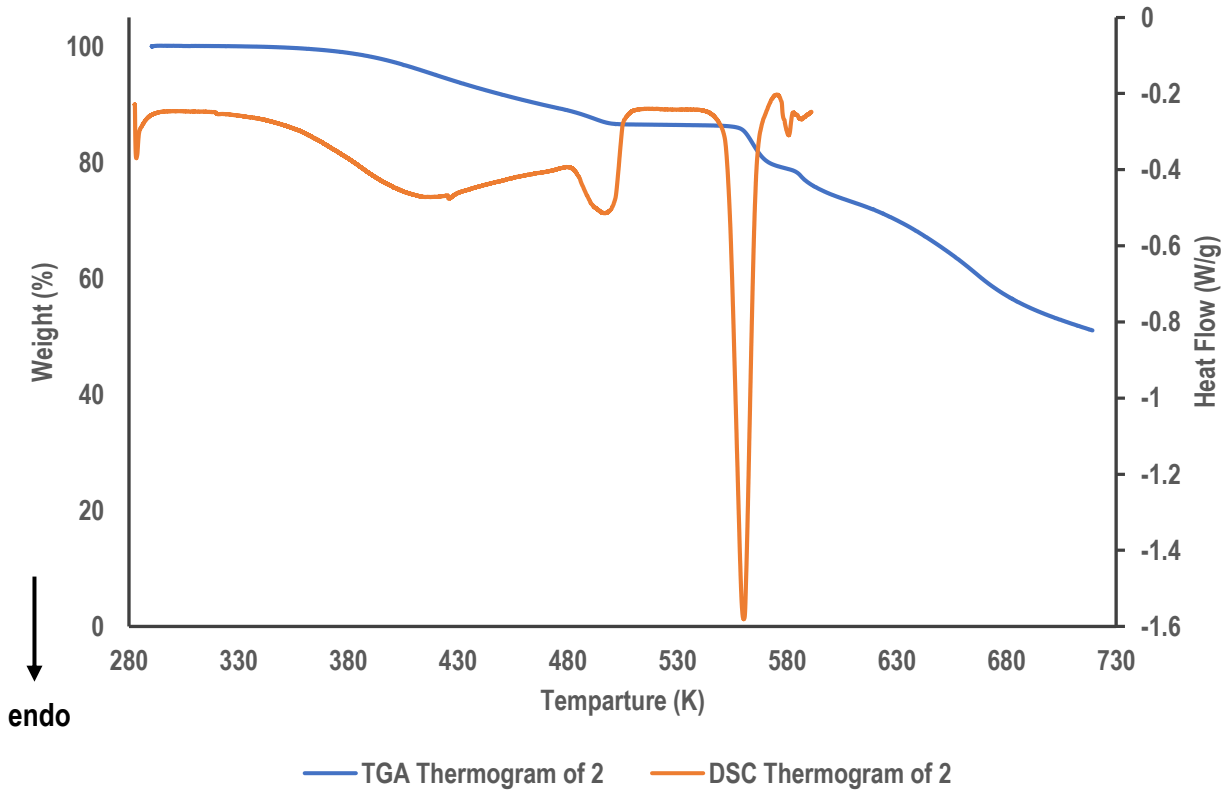

Figure 3.15 Overlay of the TGA (blue) and DSC (orange) thermograms for **2**.

3.3.2.2 Hot Stage Microscope Analysis

Crystals of **1**, for (hot stage microscope) HSM analysis, were covered in silicon oil to allow solvent loss to be observed (as bubbling) over the temperature range of 296 K – 603 K (**Figure 3.16**). The crystal begins to become opaque with heating to 417 K (b) before the onset of solvent bubbling at 452 K (c) and continued until the onset of crystal decomposition at 577 K (e). The crystal was completely decomposed by the end of heating at 603 K (f).

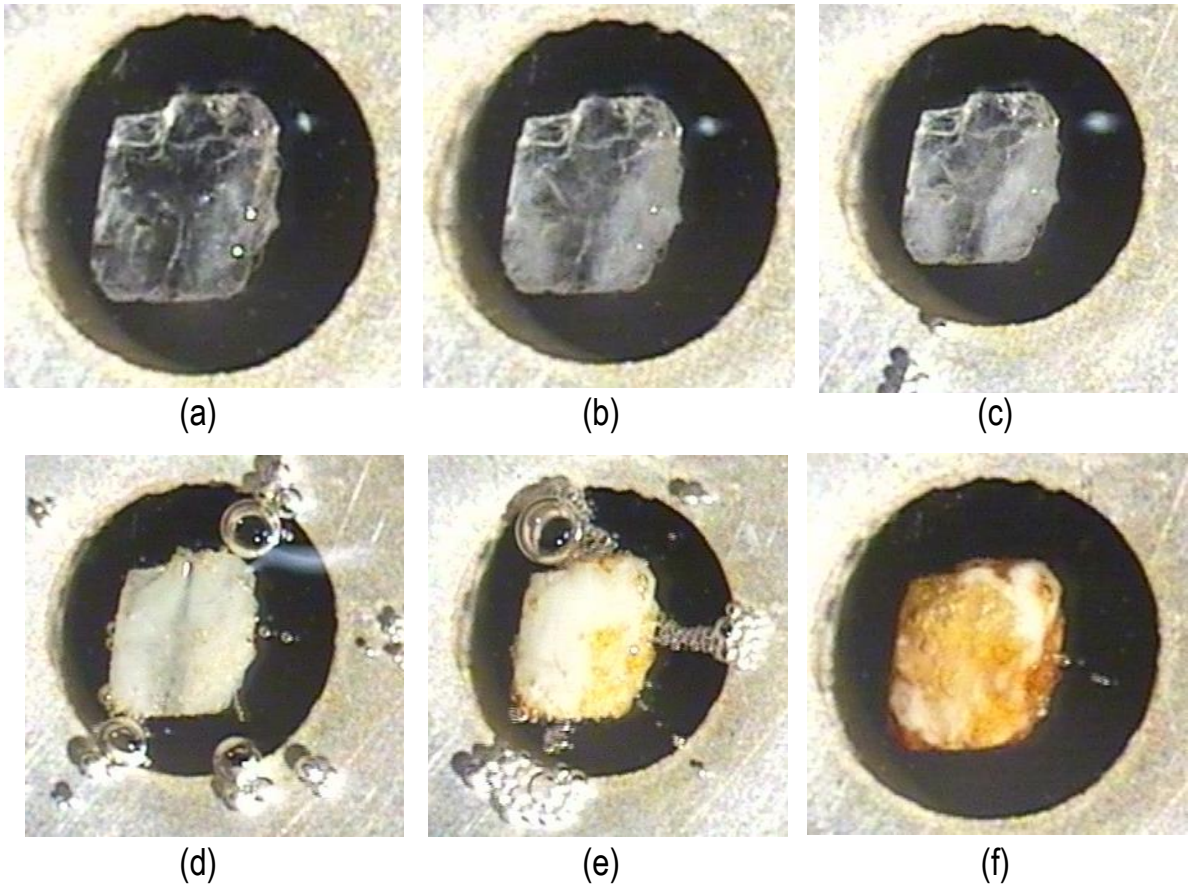

Figure 3.16 HSM images of **1** at (a) 296 K, (b) 417 K, (c) 452 K, (d) 545 K, (e) 577 K and (f) 603 K.

For **2** (**Figure 3.17**) the heating range was 301 K – 633 K. The onset of desolvation, accompanied by fine crystal cracking, was 494 K (c). Desolvation (seen as bubbling) occurred throughout the remainder of the analysis. The onset of decomposition was 555 K (d) and the crystal became opaque at 614 K (e). The crystal was completely decomposed by the end of the HSM experiment at 633 K (f).

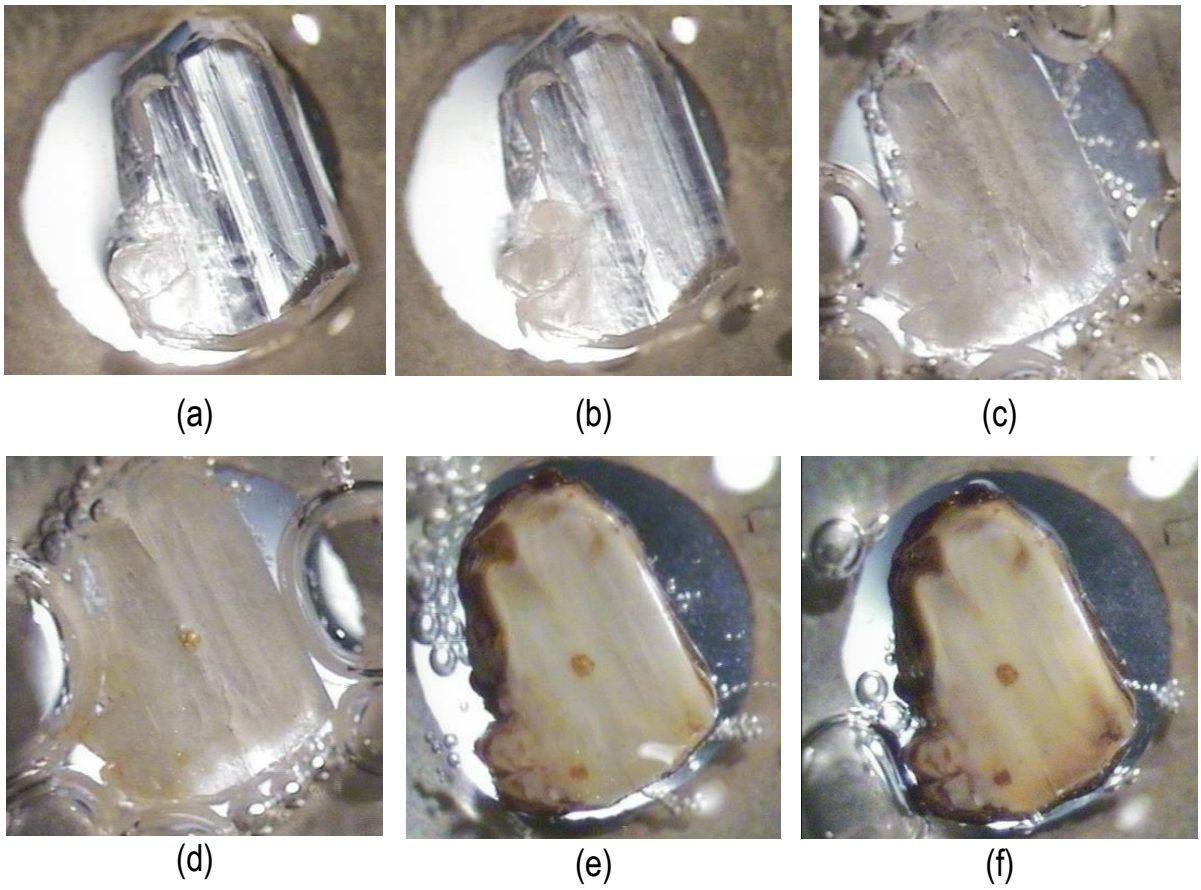

Figure 3.17 HSM images of **2** at (a) 301 K, (b) 413 K, (c) 494 K, (d) 555 K, (e) 614 K and (f) 633 K.

3.3.3 Single-crystal-to-single-crystal Desolvation Studies

3.3.3.1 TGA Dehydration and Rehydration Studies

Through HSM studies, it was noted that crystals of both compounds retained some transparency with the onset of desolvation. Despite the onset of crystal cracking with desolvation, it was suspected that both compounds may undergo a single-crystal-to-single-crystal (SC-SC) transformation. Through SC-SC transformations, a study into the changes in the crystal structure with desolvation could be conducted.

It was observed through TG analysis that both compounds absorbed water molecules when exposed to atmosphere for 10 min. In separate experiments, previously desolvated samples of **1** and **2**, which had then collected water from the atmosphere, were heated to 473 K to remove the atmospheric water molecules. Thereafter, the sample was exposed to open atmosphere for 10 min to allow the samples to

reabsorb atmospheric water molecules. The samples were then heated to 473 K again to confirm all the water molecules had been reabsorbed for **1** (**Figure 3.18**) and **2** (**Figure 3.19**). The samples' affinity for water was confirmed as the thermogram of the sample containing atmospheric water molecules before and after evacuation were superimposable for both samples.

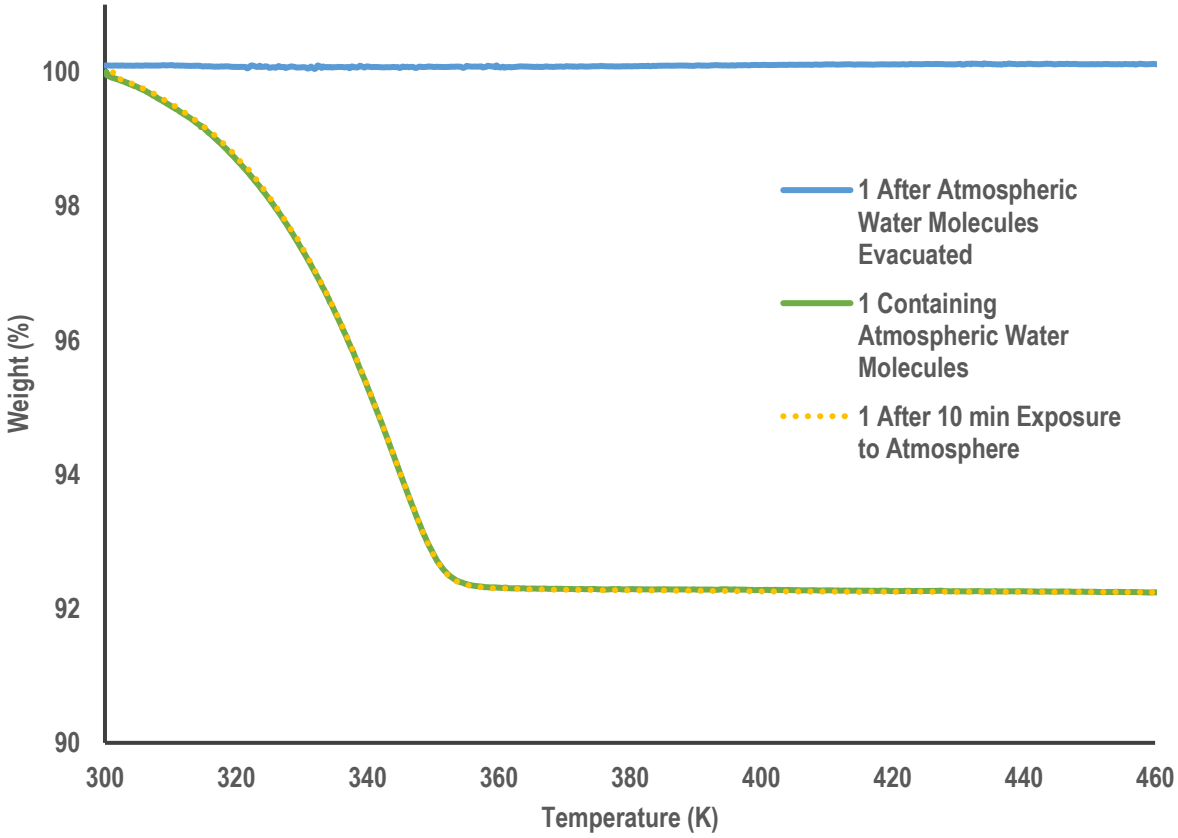

Figure 3.18 Dehydration and rehydration experiments to show the sorption of atmospheric water by **1**.

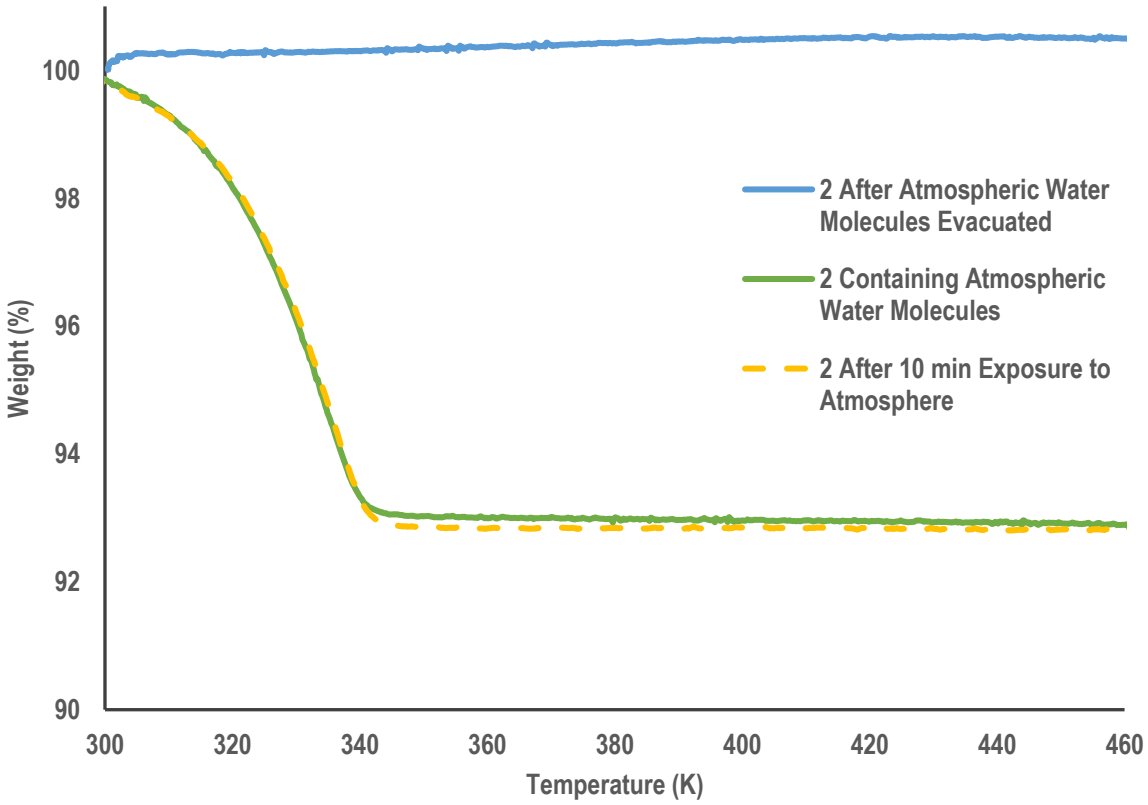

Figure 3.19 Dehydration and rehydration experiments to show the sorption of atmospheric water by **2**.

3.3.3.2 Water Exchange and Desolvation Studies for Variable-Temperature Single Crystal X-ray Diffraction

Exchange of DMF with water for **1** and **2** was achieved by two different routes (**Scheme 3.1**). The route for **1** was more indirect as crystals of **1** that were heated on a hot stage to 573 K then exposed to atmosphere for 24 h were found, through SCXRD analysis, to have adsorbed water from the atmosphere. These crystals of **1** will hereafter be referred to as **1W**. Thereafter, a crystal of **1W** underwent *in situ* heating on the diffractometer to 393 K to remove the adsorbed water and produce evacuated crystals (hereinafter **1'**).

Heating of crystals of **2** resulted in polycrystalline material and therefore single crystals of **2W** could not be accessed in the same manner as **1W**. Instead, **2W** was accessed through more direct means as as-synthesised crystals of **2** were placed in pure water for 2 weeks to undergo complete solvent exchange.

Solvent exchange through repetition of the same experiment with crystals of **1** occurred over only one day. Crystals of **2** containing water as confirmed through SCXRD analysis, i.e. **2W**, underwent *in situ* removal of adsorbed water to 393 K to produce evacuated crystals (hereinafter **2'**). Hence, desolvated structures for both compounds were accessed through the path **1**→**1W**→**1'** and **2**→**2W**→**2'**.

There were no conformational or connectivity changes to either compounds' structure. Desolvated structures were collected at 195 K and 298 K for direct comparison to temperatures of water vapour and carbon dioxide gas sorption studies. The full SCXRD collection and unit cell data for **1W**, **2W**, **1'** and **2'** are presented for both compounds in **Table 3.4**.

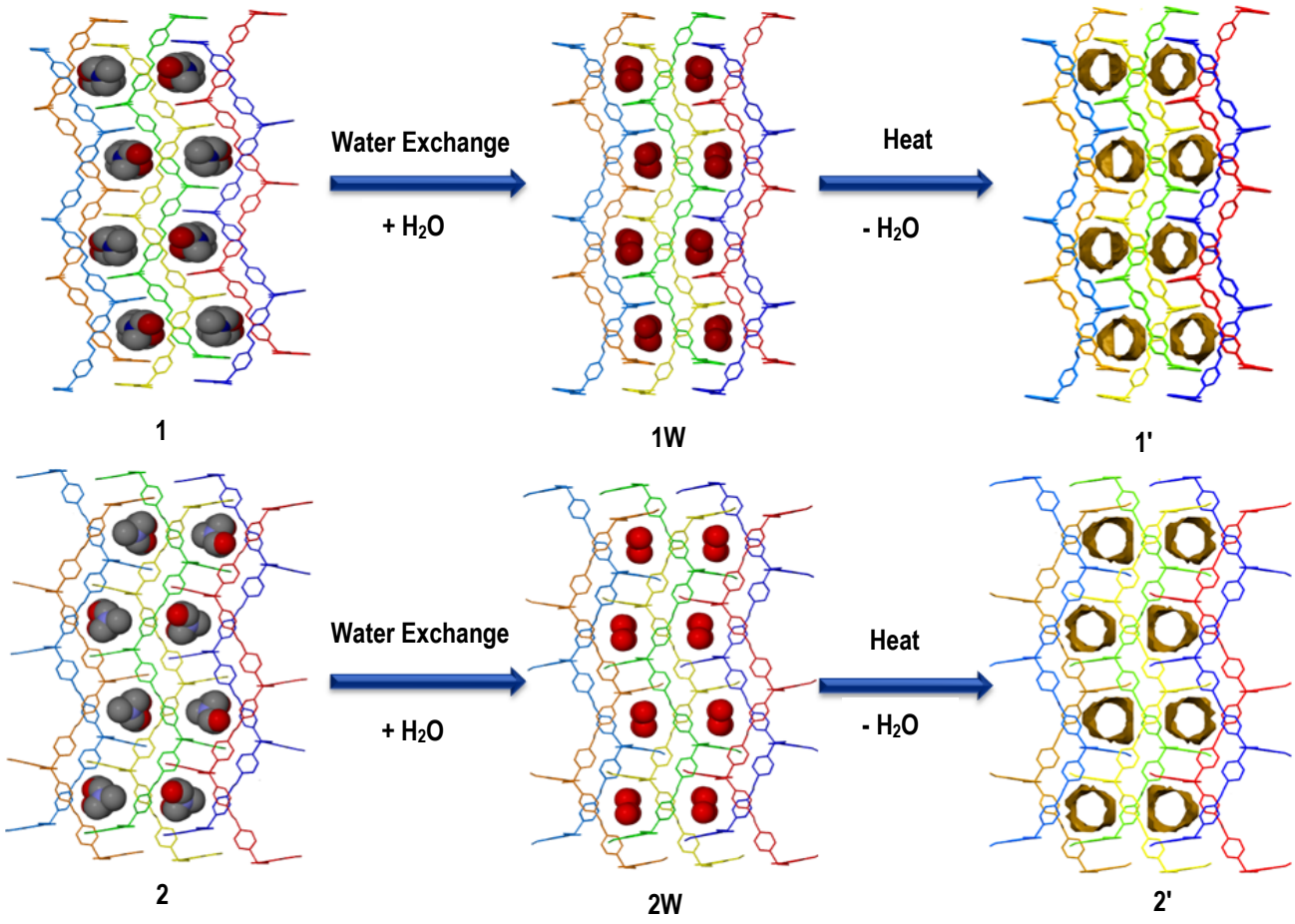

Scheme 3.1 Crystal packing diagrams of the as-synthesised MOFs **1** and **2** at 100 K (left), their water exchanged structures at 100 K (middle) and subsequent dehydrated structures at 195 K showing their mapped void spaces in orange (right).

Table 3.4 Crystal data and refinements for compounds **1W**, **2W**, **1'** and **2'**

	1W	**1' (195 K)**	**1' (298 K)**	**2W**	**2' (195 K)**	**2' (298 K)**
ASU formula	$C_{20}H_{20}N_2O_6Zn$	$C_{20}H_{16}N_2O_4Zn$	$C_{20}H_{16}N_2O_4Zn$	$C_{21}H_{22}N_2O_7Zn$	$C_{21}H_{18}N_2O_5Zn$	$C_{21}H_{18}N_2O_5Zn$
Formula weight	449.75	413.72	413.72	479.77	443.74	443.74
Temperature/K	100(2)	195(2)	298(2)	100(2)	195(2)	298(2)
Crystal system	orthorhombic	orthorhombic	orthorhombic	orthorhombic	orthorhombic	orthorhombic
Space group	*Pbca*	*Pbca*	*Pbca*	*Pbcn*	*Pbcn*	*Pbcn*
***a* / Å**	10.113(2)	10.154(3)	10.134(3)	23.1978(11)	23.2246(13)	23.236(2)
***b* /Å**	17.913(3)	17.786(4)	17.966(5)	10.1635(5)	10.1622(6)	10.1511(9)
***c* / Å**	23.299(4)	23.447(6)	23.416(7)	19.3156(10)	19.4663(12)	19.5507(19)
***α* / °**	90	90	90	90	90	90
***β* / °**	90	90	90	90	90	90
***γ* / °**	90	90	90	90	90	90
Volume/Å^3	4220.8(13)	4234.6(18)	4263(2)	4554.1(4)	4594.3(5)	4611.4(7)
Z	8	8	8	8	8	8
ρ_{calc}/g cm^{-3}	1.416	1.298	1.289	1.400	1.283	1.278
μ/mm^{-1}	1.201	1.184	1.176	1.121	1.100	1.095
F(000)	1856.0	1696.0	1696.0	1984.0	1824.0	1824.0
2θ range for data collection / °	4.944 to 52.644	3.474 to 56.458	3.478 to 52.68	3.512 to 52.812	3.508 to 52.872	3.506 to 52.882
Index ranges	-5 ≤ h ≤ 12, -22 ≤ k ≤ 14, -28 ≤ l ≤ 14	-7 ≤ h ≤ 13, -14 ≤ k ≤ 23, -13 ≤ l ≤ 31	-12 ≤ h ≤ 6, -14 ≤ k ≤ 22, -29 ≤ l ≤ 12	-20 ≤ h ≤ 29, -12 ≤ k ≤ 10, -24 ≤ l ≤ 17	-20 ≤ h ≤ 29, -10 ≤ k ≤ 12, -21 ≤ l ≤ 24	-29 ≤ h ≤ 20, -10 ≤ k ≤ 12, -24 ≤ l ≤ 21
Reflections collected	11967	13315	11366	15985	16181	16305
Independent reflections	4284 [R_{int} = 0.0692, R_{sigma} = 0.0754]	5199 [R_{int} = 0.1098, R_{sigma} = 0.1278]	4325 [R_{int} = 0.1186, R_{sigma} = 0.1232]	4674 [R_{int} = 0.0369, R_{sigma} = 0.0370]	4702 [R_{int} = 0.0441, R_{sigma} = 0.0453]	4725 [R_{int} = 0.0506, R_{sigma} = 0.0504]
Data/restraints/parameters	4284/0/265	5199/0/244	4325/0/244	4674/0/287	4702/0/263	4725/0/263
Goodness-of-fit on F^2	1.186	0.911	0.919	1.014	1.043	0.928
Final R indexes [I>=2σ (I)]	R_1 = 0.1044, wR_2 = 0.2162	R_1 = 0.0702, wR_2 = 0.1533	R_1 = 0.0707, wR_2 = 0.1548	R_1 = 0.0415, wR_2 = 0.1319	R_1 = 0.0418, wR_2 = 0.1068	R_1 = 0.0443, wR_2 = 0.1301
Final R indexes [all data]	R_1 = 0.1421, wR_2 = 0.2300	R_1 = 0.1833, wR_2 = 0.2053	R_1 = 0.1906, wR_2 = 0.2108	R_1 = 0.0565, wR_2 = 0.1442	R_1 = 0.0638, wR_2 = 0.1172	R_1 = 0.0751, wR_2 = 0.1521
Largest diff. peak/hole/e Å^{-3}	1.81/-1.38	0.57/-0.49	0.45/-0.35	1.47/-0.63	0.56/-0.38	0.58/-0.30

3.3.3.3 Void Space Analysis

Void space analysis was explored as a means of correlating the observed sorption characteristics with structural characteristics of **1** and **2**. Comparisons were made between the potential void spaces per unit cell, i.e. when the solvents were artificially removed from **1**, **1W**, **2** and **2W** and the actual void spaces per unit cell of desolvated **1'** and **2'** collected at 195 K and 298 K (**Table 3.5**). The actual void space analysis serves as a direct comparison with sorption studies of the activated MOFs at 195 K and 298 K while the potential void space analysis serves as a reference for conclusions based on the as-synthesised MOFs.

It was observed that the potential void spaces per unit cell for **1** (18.6%, 801 $Å^3$) and **2** (18.3%, 851 $Å^3$) were larger than those of, **1W** (14.5%, 614 $Å^3$) and **2W** (14.2%, 646 $Å^3$), respectively. This suggests that **1** and **2** undergo a degree of 'breathing' upon solvent exchange with water. It is also observed that the void space per unit cell in **2'** is larger than that of **1'**. It is expected that the substitution of a hydrogen atom in the **ia** ligand of **1** with the bulkier methoxy group in the **mia** ligand of **2** would reduce the cavity size, however, the methoxy group in **2** is oriented such that it does not protrude into the cavity while causing the bilayers to be further apart as indicated by an ~ 2 Å increase in the common axis from **1** (~17 Å) to **2** (~19 Å). The changes in void space per unit cell for the different structures are largely due to the bilayers moving closer together or further apart. This conclusion is based off the observation that the stacking direction axes in both compounds (~17 Å and ~19 Å in **1** and **2**, respectively) underwent the greatest changes in length, indicating that the MOFs can 'breathe' or structurally adjust to their environments without changing connectivity. The void spaces per unit mass for each structure has been determined to relate the pore volumes to the sorption study results which are typically reported in amount or volume of adsorbed gas per unit mass of activated material. The void space per unit cell of **2'** was found to be large enough to offset its slightly higher molar mass. The void spaces per unit mass of **2'** is 5.3% larger at 195 K and 2.5% larger at 298 K than that of **1'**, hence it is expected that the sorption of **2'** would be higher, by mass, than those of **1'** for a given gas or vapour.

Table 3.5 Void space analyses of potential void and actual void spaces of MOFs **1** and **2**

	1* (100 K)	**2*** (100 K)	**1W*** (100 K)	**2W*** (100 K)	**1'** (195 K)	**2'** (195 K)	**1'** (298 K)	**2'** (298 K)
Void space percent per unit cell (%)	18.6	18.3	14.5	14.2	14.9	15.5	15.4	15.6
Absolute void space per unit cell ($Å^3$/ unit cell)	801	851	614	646	631	712	655	719
Volume of unit cell ($Å^3$)	4296	4654	4221	4554	4235	4594	4263	4611
Atomic mass unit (amu) per unit cell	3309.8	3549.9	3309.8	3549.9	3309.8	3549.9	3309.8	3549.9
Void space per atomic mass ($Å^3$ / amu)	0.242	0.240	0.186	0.182	0.191	0.201	0.198	0.203
Void space per gram of MOF (cm^3 / g)	0.145	0.143	0.111	0.109	0.114	0.120	0.118	0.121

***** solvent molecules are deleted

3.4 Gas Sorption Studies

Gas and water vapour sorption studies were conducted to determine the ability of **1'** and **2'** to adsorb different gases. Gas sorption studies were also used to determine the BET surface area and isosteric heats of adsorption of each compound. Compounds **1** and **2** were heated to 473 K to activate the MOFs for subsequent hydrogen (77 K), nitrogen (77 K), carbon dioxide (195 K and 298 K) and water vapour (298 K) sorption.

Nitrogen and Hydrogen Sorption

Although the hydrogen sorption of **2'** was higher than that of **1'**, the sorption of hydrogen was still considered moderate. Typically, nitrogen sorption is used to calculate BET surface areas, however, the sorption of nitrogen did not conform to that of a type-I isotherm for either compound. The calculated BET surface areas of 40 $m^2 g^{-1}$ and 72 $m^2 g^{-1}$ for **1'** and **2'**, respectively, are relatively low indicating an inability for the N_2 to penetrate the structure of either compound despite the open channels.

Carbon Dioxide Sorption

The sorption of carbon dioxide for samples **1'** and **2'** was tested at 298 K and 195 K (**Figure 3.20**). Carbon dioxide sorption was also tested over a range of temperatures to determine the isosteric heats of adsorption (Q_{st}). The carbon dioxide sorption isotherms for 298 K exhibit a type-I isotherm showing appreciable CO_2 for both **1'** and **2'**. Study of the sorption isotherms shows higher maximum sorption for **2'** as expected from void space analysis, despite an initial lag. The maximum sorption for **2'** is 39.3 cm^3 (STP) g^{-1} corresponding to 0.78 CO_2 molecules per ASU while the maximum sorption for **1'** was 29.8 cm^3 (STP) g^{-1} corresponding to 0.55 CO_2 molecules per ASU at 795 mmHg pressure.

At 195 K, the sorption of **2'** is initially higher than that of **1'** as expected from the trend seen at 298 K. At a pressure of 236 mmHg, the sorption of **2'** is 64.4 cm^3 (STP) g^{-1} (1.28 CO_2 molecules per ASU) while the sorption of **1'** is 53.6 cm^3 (STP) g^{-1} (0.99 CO_2 molecules per ASU). However, after 275 mmHg, an inflection point occurs in the isotherm of **1'** which results in a sharp increase in the adsorption of CO_2 up

to 444 mmHg before reaching a plateau with a maximum sorption of 99.9 cm^3 (STP) g^{-1} (1.84 CO_2 molecules per ASU) at 709 mmHg, nearly double the amount of CO_2 adsorbed by **2'** at this pressure. Inflection points typically indicate some structural change which may serve as an explanation for the sorption behaviour of **1'**. The sorption isotherm of **2'** lacks a point of inflection and plateaus to a lower maximum sorption.

Intuitively, this behaviour suggests there may be some separation of bilayers in **1'** that does not occur in **2'** to accommodate the adsorption of more CO_2. However, structural analysis of the 195 K structures shows common C-H···O interactions, C1-H1···O4 and C5-H5···O4 in **1'** and **2'**, respectively, between neighbouring bilayers (**Table 3.6** and **3.7**). Counterintuitively, **1'** has an additional C-H···π interaction (C19-H19···N1-C1-C2-C3-C4-C5) between neighbouring bilayers, which is absent in **2'**. To further explore this phenomenon, *in situ* data collections would need to be performed during CO_2 sorption, which were not performed in this study due to lack of suitable experimental set up.

The desorption isotherms for **1'** and **2'** also behaved in dissimilar ways as **2'** exhibited a desorption isotherm that followed the same path as the adsorption isotherm, typical of a type-I isotherm. However, **1'** exhibited large hysteresis, with a longer return plateau to 92.2 cm^3 (STP) g^{-1} (1.70 CO_2 molecules per ASU) at 83 mmHg before a sharp decrease in sorption to 53.6 cm^3 (STP) g^{-1} (0.99 CO_2 molecules per ASU) and the lower plateau at 55 mmHg. At lower pressures, the desorption isotherm overlaps with the adsorption isotherm.

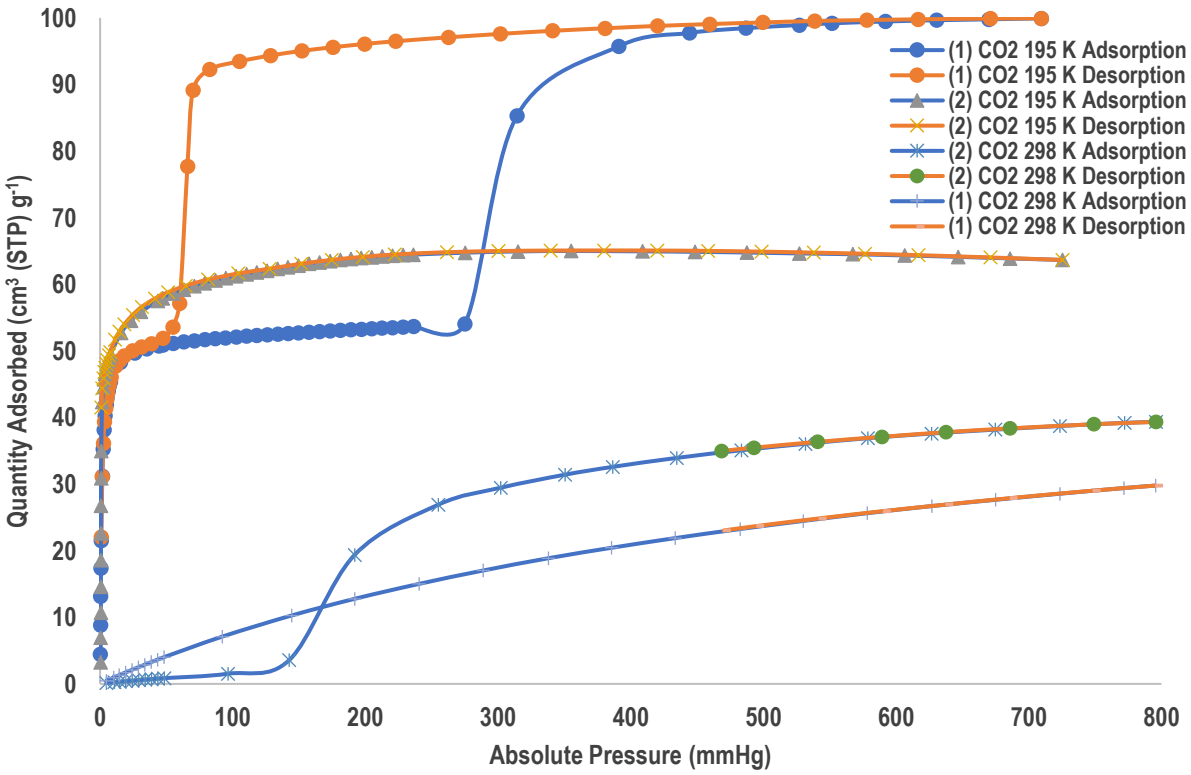

Figure 3.20 Adsorption and desorption isotherms for carbon dioxide sorption for **1'** and **2'** collected at 195 K (upper two graphs) and 298 K (lower two graphs).

Table 3.6 Hydrogen bonding parameters as obtained from PLATON for MOF **1'**

Hydrogen bonding atoms	D-H / Å	H···A / Å	D-H···A / Å	Symmetry operators
C1-H1···O4 (inter-bilayer)	0.95	2.53	3.181(7)	-x,1-y,1-z
C4-H4···O2	0.95	2.54	3.452(7)	½-x, ½-y,1-z
C15-H15···O2	0.95	2.48	2.801(7)	
C19-H19··· N1-C1-C2-C3-C4-C5				

Table 3.7 Hydrogen bonding parameters as obtained from PLATON for MOF **2'**

Hydrogen bonding atoms	D-H / Å	H···A / Å	D-H···A / Å	Symmetry operators
C5-H5···O4 (inter-bilayer)	0.93	2.41	3.245(4)	1-x, 1+y, ½-z
C2-H2···O2	0.93	2.54	3.234(4)	1-x,1-y,1-z
C6-H6A···O2	0.97	2.43	3.330(4)	1-x,1-y,1-z

The isosteric heats of adsorption (Q_{st}) (**Table 3.8**), were calculated using sorption for CO_2 at 273 K, 278 K, 283 K, 288 K and 298 K (**Figure 3.21**). Comparing the values over the same coverage range, of 0 – 29.7 cm^3 (STP) g^{-1}, it was observed that the Q_{st} values for **1'** ranged from 27.8 to 28.2 kJ mol^{-1} whilst those for **2'** started at a lower 25.1 kJ mol^{-1} but increased to a higher 29.7 kJ mol^{-1}. These observations are consistent with the observation that the sorption isotherms of **2'** lag behind those of **1'** before eventually surpassing the latter.

Table 3.8 Isosteric Heat of Adsorption (Q_{st}) for **1** and **2**

MOF	**1'**	**2'**
Coverage Range (cm^3 (STP) g^{-1})	0 – 29.7	0 – 29.7
Q_{st} Range (kJ mol^{-1})	27.8 – 28.2	25.1 – 29.7

(a)

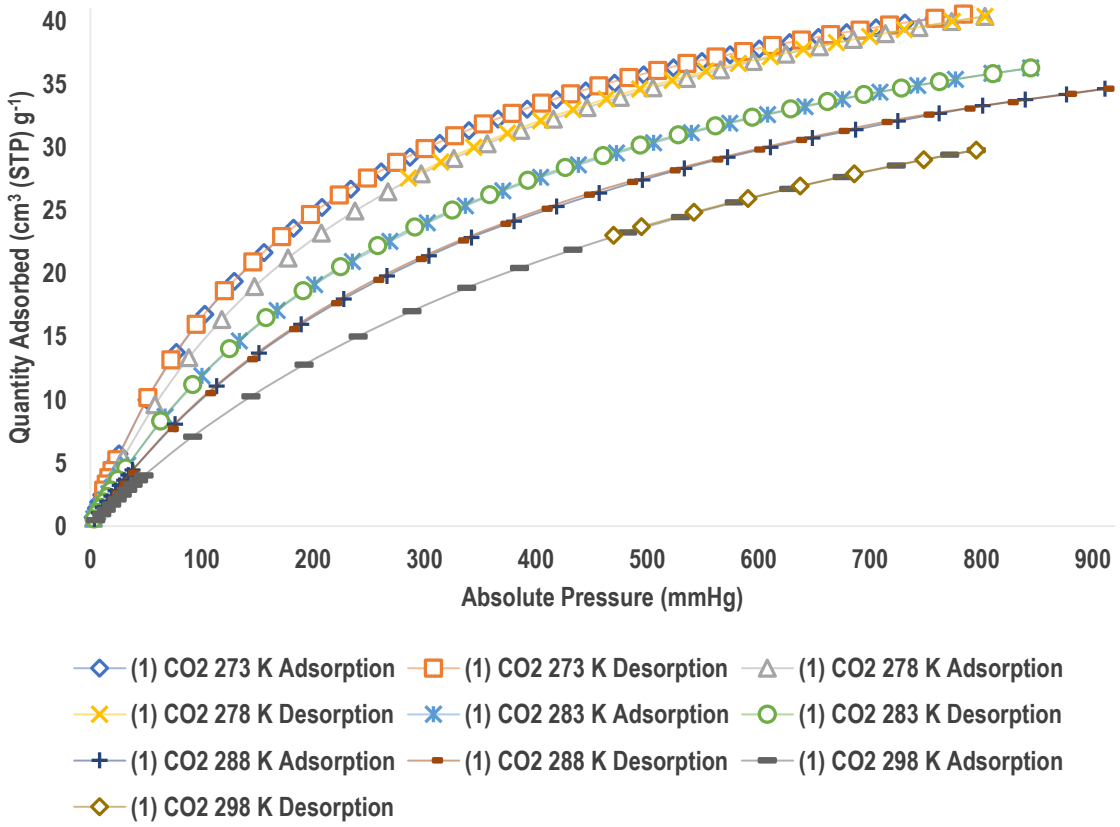

(b)

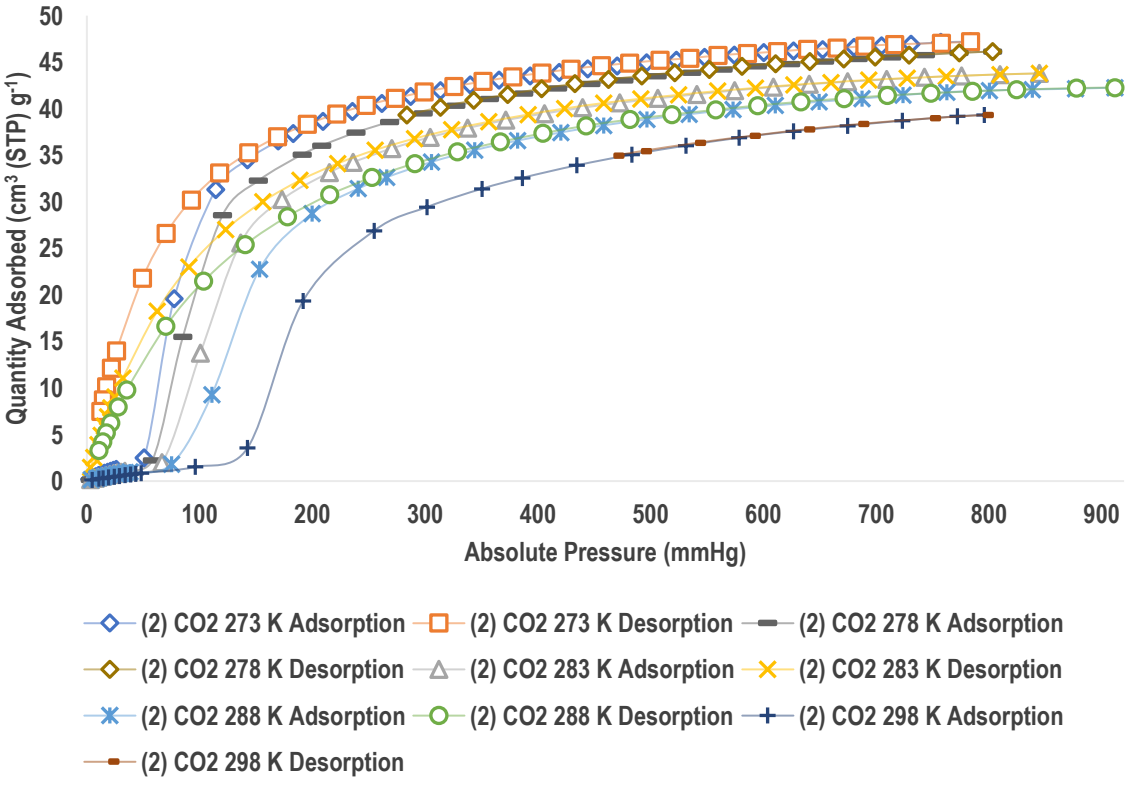

Figure 3.21 Adsorption and desorption isotherms for (a) **1'** and (b) **2'** for CO_2 (273 K – 298 K)

Bae et al. showed that in the absence of reliable nitrogen sorption data, the carbon dioxide sorption data at 273 K could be used to calculate BET surface areas of microporous MOFs with a pore diameter of less than 7 Å, although there is some controversy around the use of CO_2 sorption to determine BET surface areas.[82,83] The BET surface areas of **1'** was 187 $m^2 g^{-1}$ and 188 $m^2 g^{-1}$ using the carbon dioxide 273 K sorption isotherm data. The higher values for surface areas based on CO_2 sorption data, when compared to those obtained from N_2 data, supports the conclusion that N_2 was not able to penetrate the structures.

Hirshfeld Surface Analysis

Hirshfeld surface analysis may provide some insight for the different carbon dioxide sorption behaviours of **1'** and **2'** at 195 K. Analysis of the Hirshfeld surface of the ASUs of the MOFs at 195 K showed a greater percentage contribution of H···H interactions in **1'** than in **2'** (36.9% vs 35.4%) and a lower percentage contribution of C···H interactions in **1'** than in **2'** (22.4% vs 23.3%) (**Table 3.9**). H···H interactions are considered generally repulsive while C···H are considered generally attractive.

Table 3.9 Summary of the intermolecular surface contact contributions in **1'** (195 K) and **2'** (195 K)

Contact	Contribution% 1' (195 K)	Contribution% 2' (195 K)
H···H	36.9	35.4
N···H	3.0	1.7
C···H	22.4	23.3
O···H	23.4	26.8
C···C	2.6	2.7
C···N	0.0	0.1
C···O	2.1	0.1
N···O	1.6	1.6

Further analysis through mapping of the curvedness property onto the Hirshfeld surfaces indicated a red region over the phenyl ring of **mia** in **2'**, which is indicative of closer π-π stacking interactions (**Figure 3.22** (a) and (b)). It was observed that the phenyl rings in both structures are the sections in the bilayers that interdigitate with those of the neighbouring bilayers. Measurement of the distance between

the centroids of the closest, interdigitated phenyl rings on neighbouring bilayers showed a shorter distance in **2'** (3.843 Å) than in **1'** (4.054 Å) which supports the observation from the curvedness plot. The fingerprint plot of the Hirshfeld surfaces shows that **2'** has a 'lighter blue' colour at d_i and d_e of ~2.0 Å than **1'**. This indicates a larger percentage of interactions at distances associated with the π-π stacking regions (**Figure 3.22** (c) and (d)). The absence of these π-π interactions in **1'** may facilitate the movement of the bilayers to allow a second carbon dioxide molecule per ASU to be adsorbed.

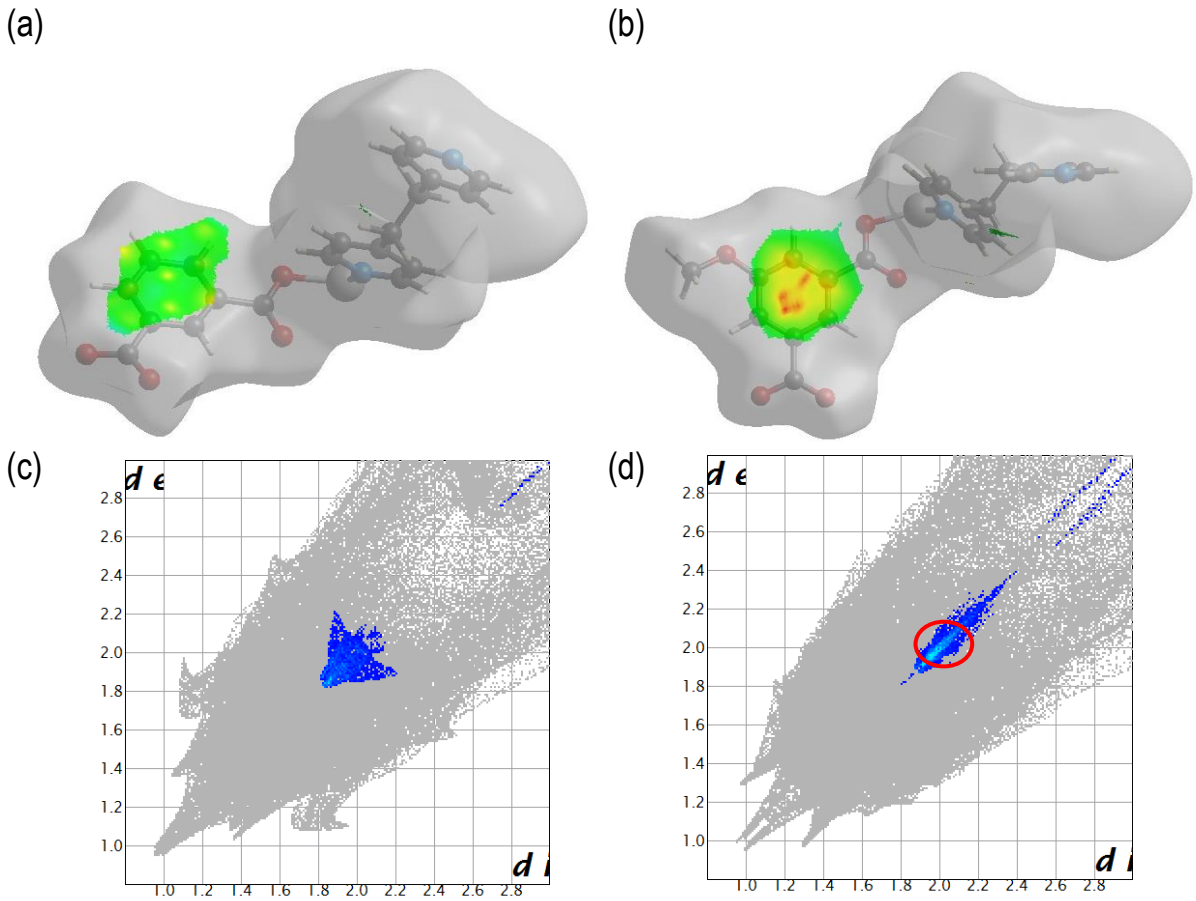

Figure 3.22 C···C isolated interactions for curvedness property plotted onto Hirshfeld surface of (a) **1'** (195 K) and (b) **2'** (195 K) and fingerprint plots for (c) **1'** (195 K) (d) **2'** (195 K)

Water Vapour Sorption

1' and **2'** both show a high affinity for water vapour sorption, as evidenced by the TG analysis done after the samples had been exposed to atmosphere for 10 min. Gas sorption studies revealed that both samples have the highest sorption capacity for water vapour with maximum water sorption of 115.7 cm^3 (STP) g^{-1} at P/P_o = 0.81 (2.14 water molecules per ASU) and 105.6 cm^3 (STP) g^{-1} at P/P_o = 0.82 (2.09 water molecules per ASU) for **1'** and **2'**, respectively. Interestingly, although there were some similarities in their water vapour sorption graphs, there were also some intriguing differences. Both graphs gradually increase before reaching an inflection point, after which the sorption sharply increases. All points mentioned in text are indicated by red (adsorption) and green (desorption) asterisks (**Figure 3.23**). Compounds showed water vapour sorption graphs with inflection points in their sorption isotherms. However, compound **1'** shows a moderate and gradual increase in sorption until P/P_o = 0.13 where it has adsorbed 18.7 cm^3 (STP) g^{-1} (0.34 water molecules per ASU). Thereafter, there was a sharp increase in water sorption at P/P_o = 0.14 which shows sorption of 53.7 cm^3 (STP) g^{-1} (0.99 water molecules per ASU). Sorption continued to increase moderately before hitting an inflection point, indicating a structural change to accommodate more water vapour, at P/P_o = 0.17 of sorption 66.5 cm^3 (STP) g^{-1} (1.23 water molecules per ASU). The next recorded point, at P/P_o = 0.19 showed sorption of 99.6 cm^3 (STP) g^{-1} (1.78 water molecules per ASU). The sample subsequently adsorbed water in a gradual plateau to the maximum sorption of 115.7 cm^3 (STP) g^{-1} at P/P_o = 0.81 (2.14 water molecules per ASU). The desorption isotherm is virtually superimposable on the adsorption isotherm, showing no signs of hysteresis.

The water sorption for **2'** shows a similar trend to that of **1'** but with some distinct differences, especially in the desorption isotherm. The first significant accelerated increase in sorption occurs at P/P_o = 0.09 where **2'** had adsorbed 17.2 cm^3 (STP) g^{-1} (0.34 water molecules per ASU). However, unlike in **1'**, this sorption increase was modest. The major inflection point occurs at P/P_o = 0.16 for 29.4 cm^3 (STP) g^{-1} sorption (0.58 water molecules per ASU) after which there was a sharp increase in sorption until the

isotherm started to plateau at P/P_o = 0.24, sorption 93.7 cm^3 (STP) g^{-1} (1.84 water molecules per ASU). Thereafter, the sorption plateaus to the maximum sorption value of 105.6 cm^3 (STP) g^{-1} at P/P_o = 0.77 (2.09 water molecules per ASU). It is observed that the pores of **2'** are more hydrophilic than those of **1'** as the same amount of water vapour is adsorbed by **2'** at lower relative pressures than **1'** (**1'** and **2'** adsorbed 0.34 molecules of water per ASU at P/P_o = 0.13 and P/P_o = 0.09, respectively), indicating that the pores of **2'** are more polar.[36,84] This is possibly as a result of the additional methoxy group creating a more polar environment. The desorption isotherm of **2'** shows hysteresis not seen in the desorption isotherm of **1'** and could explain why CO_2 sorption is higher for **2'** than for **1'**, based off void space per unit mass ratios alone, except at 195 K where structural changes of **1'** cause higher sorption. The desorption isotherm shows gradual decrease until P/P_o = 0.10 for sorption 84.2 (STP) g^{-1} (1.67 water molecules per ASU) followed by a sharp decrease to P/P_o = 0.09 for sorption 24.9 cm^3 (STP) g^{-1} (0.49 water molecules per ASU) before gradually decreasing to the end of the desorption isotherm.

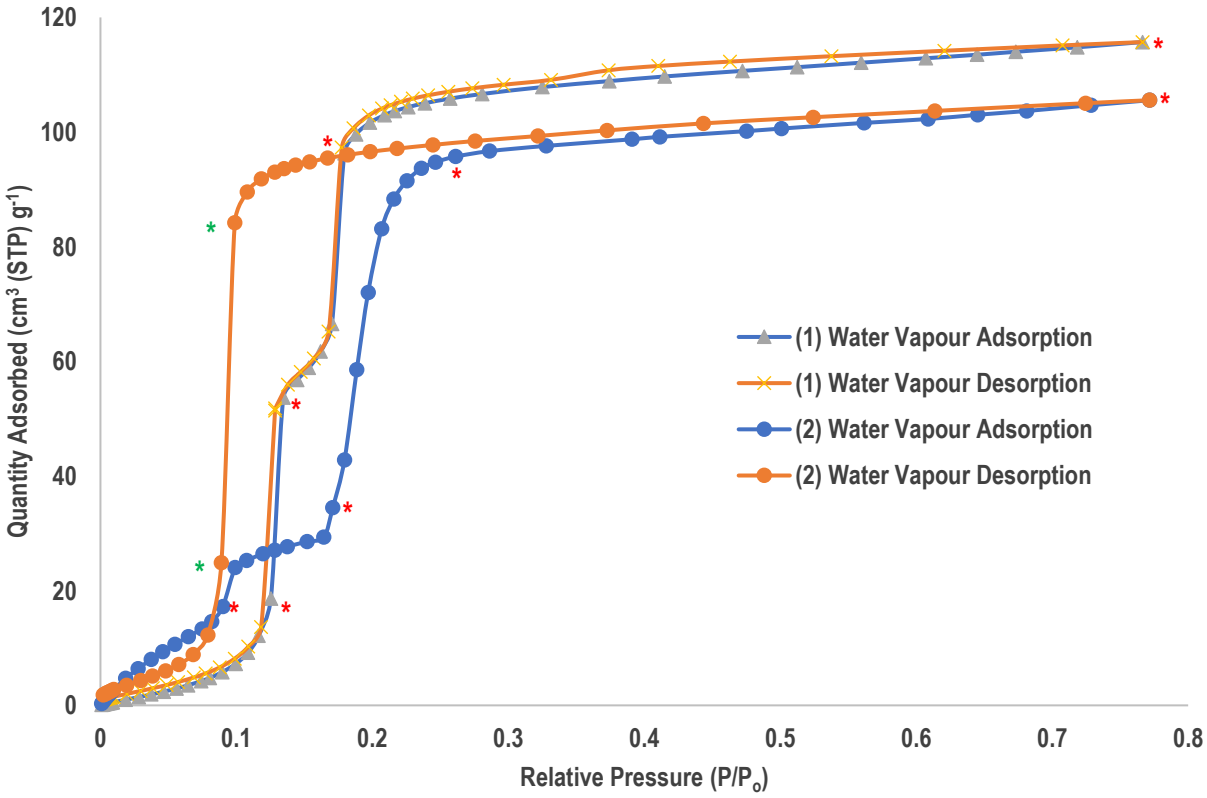

Figure 3.23 Adsorption and desorption isotherms for water vapour sorption for **1'** and **2'**. Red asterisks indicate the points specified along the adsorption isotherm and green asterisks indicate the points specified along the desorption path in the **Water Vapour Sorption** studies section.

VT–PXRD was used to further test the samples' high affinity for water sorption. *In-situ* studies of both evacuated samples while they were exposed to the atmosphere revealed slight peak differences as the samples transitioned from the hydrated samples, labelled as 298 K heating, to the evacuated samples, labelled as 393 K cooling, back to the hydrated samples, labelled as 298 K cooling. The PXRD patterns were compared to those of the calculated pattern as determined from solvent exchange with water. Due to the rapid nature of water sorption, only peaks in the 2θ range of 7 – 12.5° were measured to visualise the peak at ~9.9° (**1W**, **Figure 3.24**) and ~9.2° (**2W**, **Figure 3.25**) at 373 K which appeared in the presence of water vapour and greatly diminished with desolvation through heating. These small peak changes support data from VT–SCXRD and gas sorption which indicate slight structural changes in the sample as water molecules are allowed into and evacuated from the samples. This supports that

activated samples for gas sorption first went through a hydrated phase as samples were inevitably exposed to the atmosphere when weighed after heating and just before the commencement of the gas sorption experiments. Thus, the pathway for as-synthesised to activated samples are **1** / **2** → **1W** / **2W** → **1'** / **2'**.

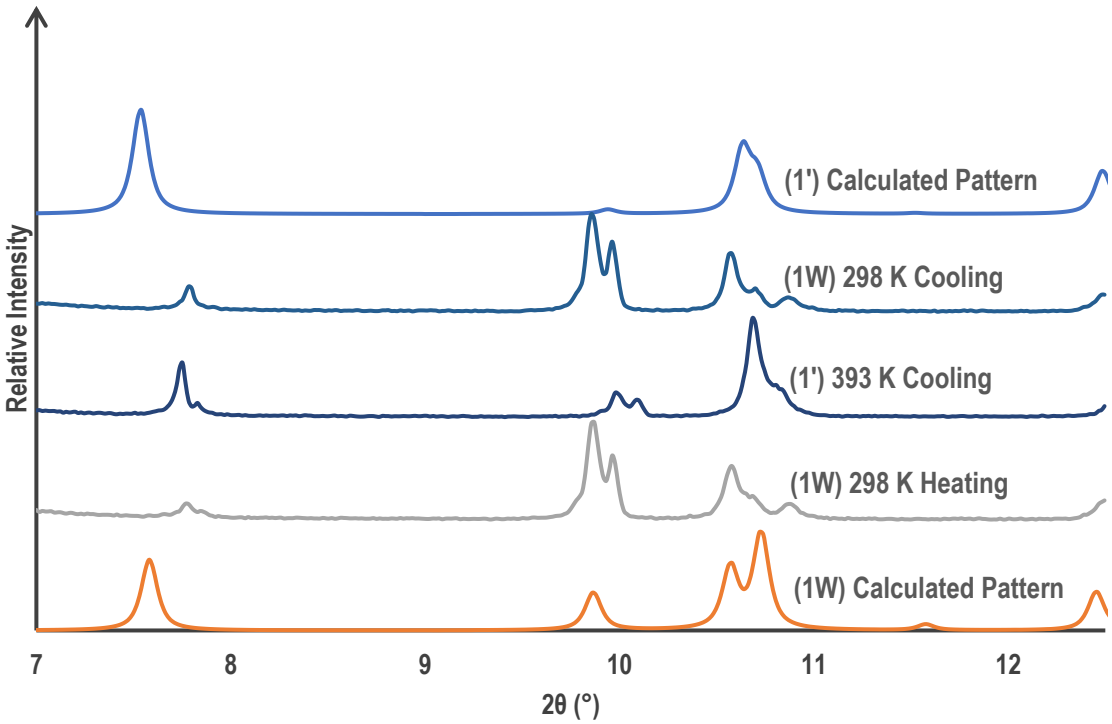

Figure 3.24 Water vapour sorption and desorption VT–PXRD pattern for **1** in 2θ range 7 – 12.5° to track increase and decrease in peak intensity of peak ~9.9°

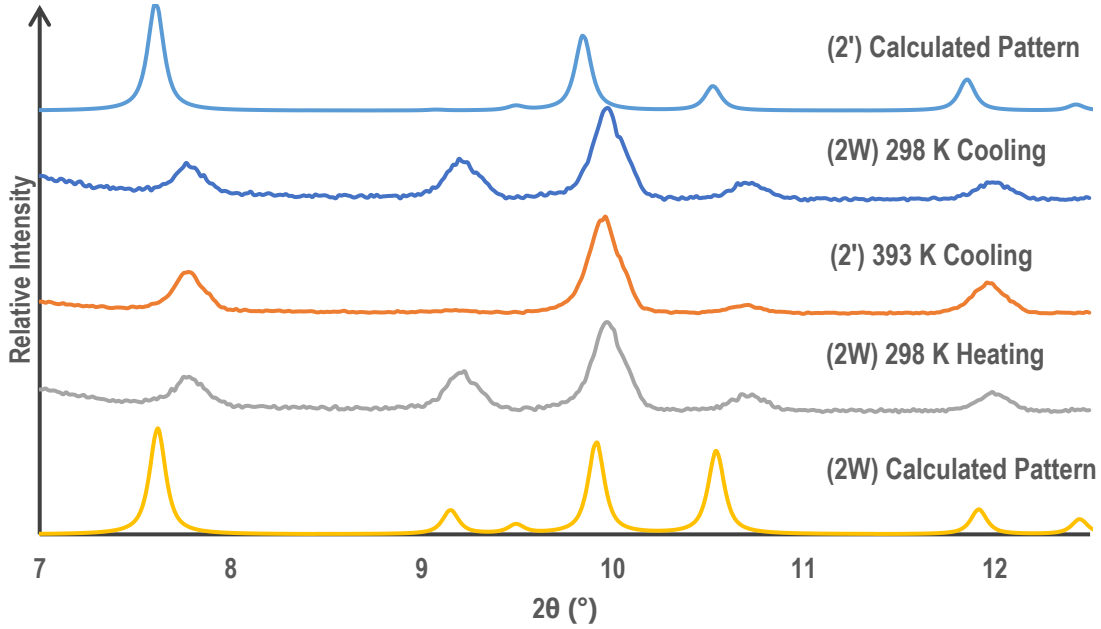

Figure 3.25 Water vapour sorption and desorption VT–PXRD pattern for 2 in 2θ range 7 – 12.5° to track increase and decrease in peak intensity of peak ~9.2° .

Chapter 4:

Cd Metal-Organic Frameworks

Two, novel Cd mixed-ligand MOFs with formula [Cd(μ_2-**mia**)(μ_2-**bpe**)$_{1.5}$]$_n$·n(DMF)$_{0.5}$$n$(H$_2$O)$_{0.5}$ (**3**) and [Cd(μ_2-**nia**)(μ_2-**bpee**)$_{1.5}$]$_n$·nDMF (**4**) were synthesised. Both compounds exhibit **sql** lattice, 2-periodic 3D net coordination layers. The structures were compared to an isoreticular structure from the literature. The compounds were characterised fully through X-ray diffraction (SCXRD, VT–SCXRD, PXRD and VT–PXRD) and thermal analysis (HSM, DSC and TGA). The chapter is divided according to each characterisation technique wherein the analytical results for each compound are discussed. Liquid sorption experiments were conducted on the synthesised MOFs. The compounds were tested for their gas and water vapour sorption capabilities to determine their porosity.

4.1 Synthesis

4.1.1 Preparation of [Cd(μ_2-mia)(μ_2-bpe)$_{1.5}$]$_n$·n(DMF)$_{0.5}$$n$(H$_2$O)$_{0.5}$ (3)

4.1.1.1 Solvothermal Synthesis

The metal salt, $Cd(NO_3)_2{\cdot}4H_2O$ (100 mg, 0.43 mmol), was dissolved in 3 mL H_2O and then stirred for 10 min. The organic ligands, 1,2-bis(4-pyridyl)ethane (117 mg, 0.65 mmol) and 5-methoxyisophthalic acid (84 mg, 0.43 mmol) were dissolved in 6 mL of *N,N'*-dimethylformamide (DMF) then stirred for 10 min. The solution of organic ligands was mixed with the metal salt solution, in a 1.5:1:1 (L1:L2:M^{2+}) molar ratio, with continuous stirring followed by the addition of 0.2 μl H_2SO_4 (3M) to aid dissolution. The resulting clear solution was sealed in a 25 mL vial then heated in an oven at 90 °C for 48 hours. Inspection of the solution vial after 48 h showed crystals to be present. Thereafter, the solution was cooled slowly up to 30 °C at a rate of 10 °C per hour.

4.1.1.2 Liquid-Assisted Grinding

LAG experiments were attempted as a means of mechanochemical synthesis to determine if **3** could be synthesised using the more rapid and high yield technique. The starting materials comprised of the same organic ligands, H_2**mia** and **bpe**, and $Cd(NO_3)_2{\cdot}4H_2O$ metal salt as used in the solvothermal synthesis. The organic ligands and metal salt were combined in a 1:1:1 ratio and ground together for 20 min with a mortar and pestle. A 1:1 mixture of DMF and H_2O was added dropwise to assist the grinding process. The PXRD pattern of the LAG product was compared to that of the calculated pattern for **3** obtained from SCXRD studies (**Figure 4.1**). The LAG product was completely amorphous proving LAG to be an unsuccessful synthetic technique for the formation of **3**.

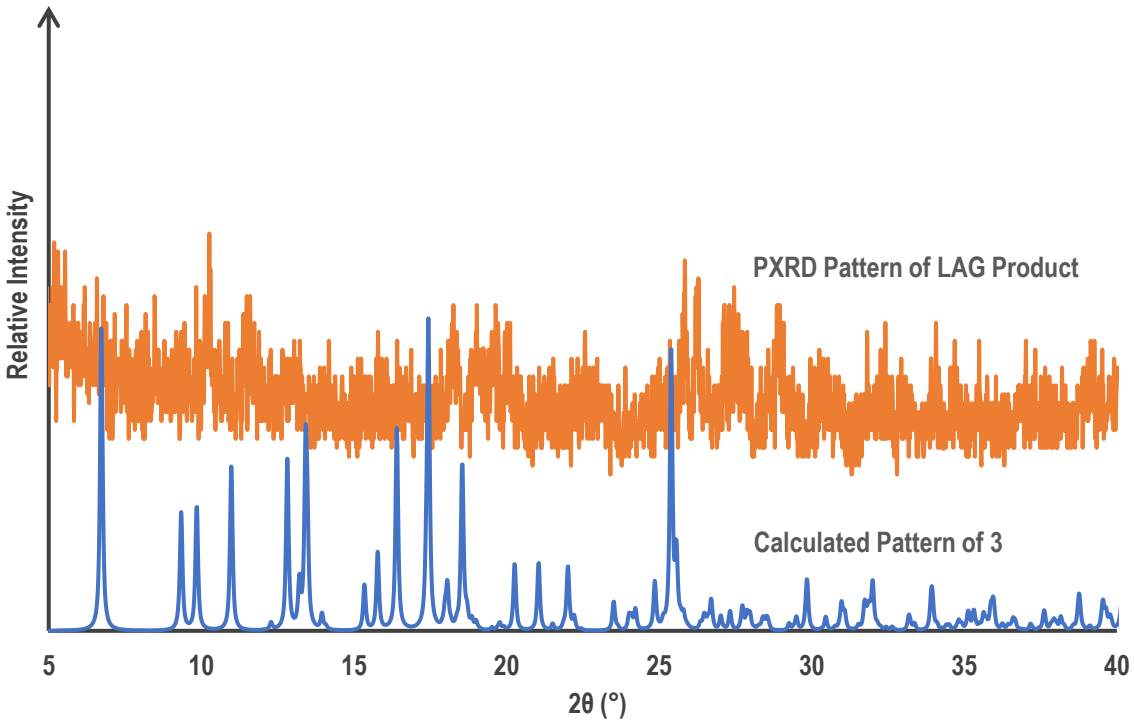

Figure 4.1 PXRD patterns of the LAG product and calculated pattern for **3**.

The PXRD pattern of the LAG product of **3** was also compared to the powder pattern of its starting materials (**Figure 4.2**). The amorphous nature of the compound made finding corresponding peaks difficult. It is possible that the LAG product was an amorphous coordination compound, however, because the powder pattern of the LAG product did not match that of the calculated pattern of **3** and solvothermal techniques proved to be a more reliable synthetic method, further experimentation on the cogrinding product was not done.

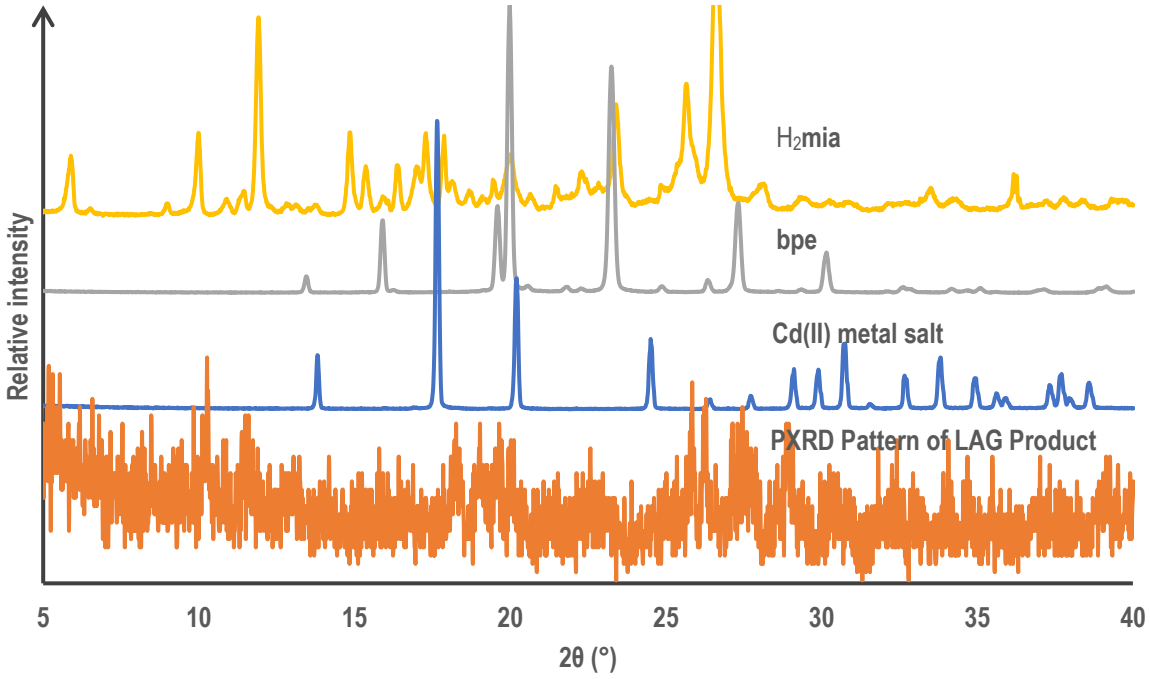

Figure 4.2 PXRD patterns of the LAG product and starting material for **3**.

4.1.2 Preparation of [Cd(μ_2-nia)(μ_2-bpee)$_{1.5}$]$_n$·*n*DMF (4)

4.1.2.1 Solvothermal Synthesis

The metal salt, $Cd(NO_3)_2{\cdot}4H_2O$ (100 mg, 0.43 mmol), was dissolved in 3 mL H_2O and stirred for 10 min. The organic ligands, 1,2-bis(4-pyridyl)ethylene (117 mg, 0.65 mmol) and 5-nitroisophthalic acid (90 mg, 0.43 mmol) were dissolved in 6 mL of *N,N'*-dimethylformamide (DMF) then stirred for 10 min. The solution of organic ligands was mixed with the metal salt solution, in a 1.5:1:1 (L1:L2:M^{2+}) molar ratio. The resulting clear solution was heated in an oven at 90 °C for 24 hours. Inspection of the solution vial after 48 h showed crystals to be present. Thereafter, the solution was cooled slowly up to 30 °C at a rate of 10 °C per hour.

4.1.2.2 Liquid-Assisted Grinding

LAG was also attempted to determine whether this technique could be used to rapidly synthesise **4** in high yield. The method of synthesis was as outlined for **3** in **section 4.1.1.2**, however, the ligand H_2**nia** was used instead of H_2**mia.** The PXRD pattern of the LAG product was compared to that of the calculated pattern for **4** (**Figure 4.3**) and the powder patterns of its starting materials (**Figure 4.4**). When compared to the calculated pattern of **4**, the powder pattern of the LAG product of **4** was found to be a different product with several mismatched peaks. Peaks at 8.1°, 8.6°, 9.0°, 11.8°, and 14.5° in the LAG pattern are not present in the calculated pattern indicating that the LAG product was different from that of solvothermal synthesis.

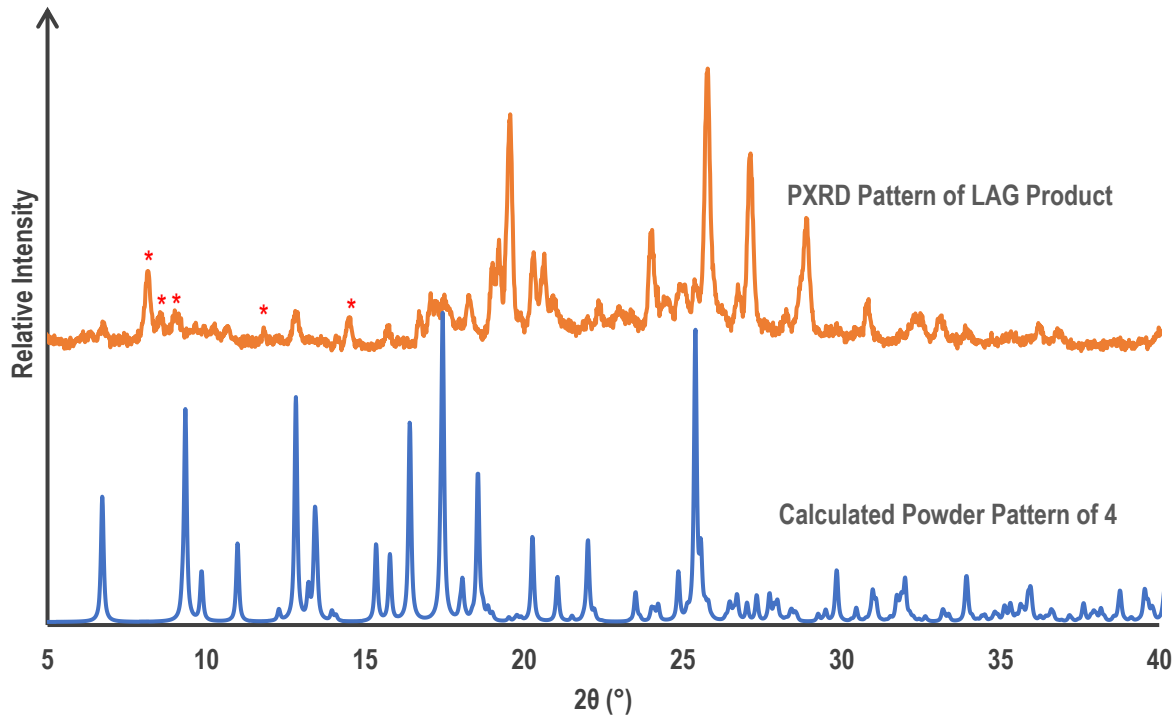

Figure 4.3 PXRD patterns of the LAG product and calculated pattern for **4**. Red asterisks indicate selected peaks specified in **section 4.1.2.2**.

When comparing the powder pattern of the LAG product of **4** to the powder patterns of its starting materials, peaks are shared with **bpee** at 12.7°, 15.7°, 17.0° and 17.4°, indicated on the **bpee** pattern,

and with H_2**nia** in the 2θ range of 20.3° – 20.8°, indicated on the H_2**nia** pattern. However, the LAG product had new peaks at 8.1°, 14.4° and 18.3° suggesting some new product has been formed. The new peaks, however, did they match those of the calculated pattern of **4**, hence, LAG was not employed as a synthetic means to produce **4** in bulk.

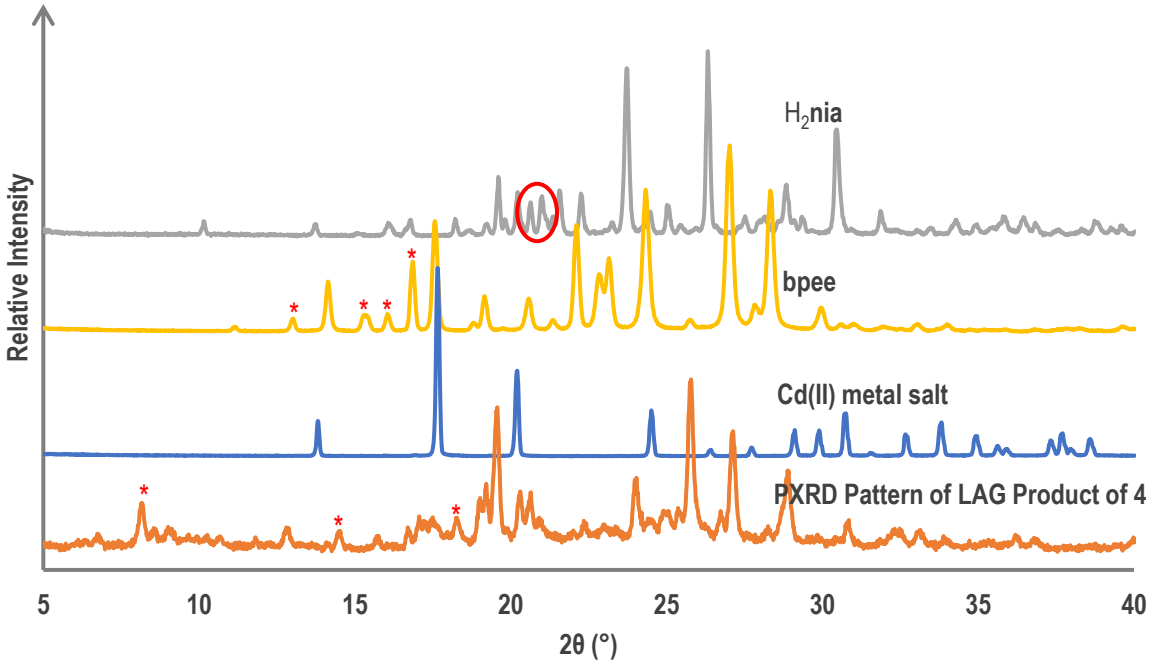

Figure 4.4 PXRD patterns of the LAG product and starting materials. Red asterisks and circles indicate selected new peaks and peak regions specified in **section 4.1.2.2**.

4.2 Single Crystal X-ray Diffraction

4.2.1 Structure Solution and Refinement

A crystal of each compound was selected from the mother liquor and placed on the Bruker DUO Apex II CCD diffractometer for data collections. The data collection procedure is outlined in **section 2.3.1**. Comparisons are made between the Cd MOFs and a previously reported Cd MOF $[Cd(bpe)_{1.5}(nbdc)]_n \cdot n$DMF collected at 104 K which will be referred to by its CSD reference code **JECRAN**.[85] The full SCXRD collection and unit cell data are presented for all three compounds in **Table 4.1**.

For **3**, the SIMU and RIGU SHELX restraints have been placed on the O5 and C27 atoms of the methoxy group on the **mia** ligand. The geometry of the C8A, C9A, C10A, N2A, C11A and C12A, as well as the C8B, C9B, C10B, N2B, C11B and C12B atoms have been restrained to ideal geometry with the AFIX 66 SHELX restraint. The atoms C8A, C9A, C10A, N2A, C11A and C12A, as well as the C8B, C9B, C10B, N2B, C11B and C12B atoms have been modelled isotropically.

For **4**, the SIMU and RIGU SHELX restraints have been placed on atoms N2A, C9A, C10A, C11A, C12A, C13A, C14A, C15A, C16A, C17A, C18A, C19A, C20A, C21A and N3A as well as atoms N2B, C9B, C10B, C11B, C12B, C13B, C14B, C15B, C16B, C17B, C18B, C19B, C20B, C21B and N3B. The DFIX restraint of 1.2 Å has been placed on atoms C1SA and O1SA. Atoms N2A, C9A, C10A, C11A, C12A and C13A and N2B, C9B, C10B, C11B, C12B and C13B in the pyridyl rings of the **bpee** ligand have been restrained to ideal geometry with the AFIX 66 SHELX restraint.

Table 4.1 Crystal and refinement data for compounds **3** and **4** compared to **JECRAN**

	3	**4**	**JECRAN**[85]
Asymmetric Unit Formula	$C_{28.5}H_{28.5}CdN_{3.5}O_6$	$C_{29}H_{25}CdN_5O_7$	$C_{27.86}H_{25.34}CdN_{4.57}O_{6.62}$
Formula Weight/g mol^{-1}	628.45	667.94	643.19
Temperature/K	100(2)	100(2)	104(2)
Crystal System	monoclinic	monoclinic	triclinic
Space Group	*C2/c*	*C2/c*	*P*-1
***a* / Å**	26.912(2)	28.3265(12)	10.2340(5)
***b* / Å**	10.2026(8)	10.1606(4)	10.8368(6)
***c* / Å**	20.566(2)	20.4037(9)	13.8265(7)
***α* / °**	90	90	100.7670(10)
***β* / °**	110.102(2)	111.9870(10)	102.2560(10)
***γ* / °**	90	90	108.8430(10)
Volume/Å^3	5302.8(7)	5445.4(4)	1363.02(12)
Z	8	8	2
ρ_{calc}/g cm^{-3}	1.574	1.629	1.567
μ/mm^{-1}	0.873	0.860	0.854
***F*(000)**	2560	2704	652
2θ range for data collection/	3.224 to 56.748	3.102 to 56.65	3.136 to 61.31
Reflections collected	52398	66586	17010
Independent reflections	6621 [R_{int} = 0.0408, R_{sigma} = 0.0234]	6788 [R_{int} = 0.0634, R_{sigma} = 0.0319]	8338 [R_{int} = 0.0138, R_{sigma} = 0.0195]
Data/restraints/parameters	6621/24/358	6788/735/532	8338/652/432
Goodness of fit of F^2	1.054	1.042	1.141
Final R indexes [I ≥ 2σ (I)]	R_1 = 0.0448, wR_2 = 0.1104	R_1 = 0.0385, wR_2 = 0.0984	R_1 = 0.0355, wR_2 = 0.1057
Final R Indexes [all data]	R_1 = 0.0520, wR_2 = 0.1162	R_1 = 0.0504, wR_2 = 0.1065	R_1 = 0.0362, wR_2 = 0.1063
Largest diff. peak/hole/e Å^{-3}	3.61/-1.55	1.22/-0.84	2.63/-1.07

4.2.2 Structure description

4.2.2.1 [Cd(μ_2-mia)(μ_2-bpe)$_{1.5}$]$_n$·n(DMF)$_{0.5}$$n$(H$_2$O)$_{0.5}$ (3)

Compound **3** crystallises in the monoclinic crystal system in the space group *C*2/*c*. **Figure 4.5** shows the complete coordination sphere in which the asymmetric unit (ASU) atoms, except part B of the disordered component over half the **bpe** ligand, have been labelled. The full ASU comprises of a Cd(II) ion coordinated to one complete **bpe** ligand with disorder and one half **bpe** ligand as well as one fully deprotonated **mia** ligand. Part A of the disordered half of the **bpe** ligand has as s.o.f. of 0.50 and thus part B has a s.o.f. of 0.50 as well. The ASU also contains one, half-occupied, uncoordinated DMF and one, half-occupied, uncoordinated water molecule. The angles present around the Cd(II) cation range from 52.96(9)° – 174.76(16)°.

Cd1 exhibits distorted, pentagonal bipyramidal geometry and is coordinated equatorially to the oxygen atoms of both carboxylate groups of the **mia** ligand and to the pyridyl moiety of the **bpe** ligand in a bridging fashion. The metal ion is coordinated to the three nitrogen atoms, N1, N2A^{v} and N2B^{v} of the disordered **bpe** and to N3 of the non-disordered, half **bpe** as well as the four oxygen atoms O1, O2, O3^{i} and O4^{i} of the **mia** ligand (where i = x, -1+y, z and v = 1/2+x, 3/2-y, -1/2+z).

The deprotonated carboxylate groups on the **mia** ligand provide the 2- charge to balance the 2+ charge on the Cd(II) ion. The solvent molecules and the **bpe** ligand are both neutral. There are two high density peaks (3.61 Å^3 and 1.72 Å^3) near the methoxy group of the **mia** ligand that could not be properly assigned as the expected geometry around atom C22 is 120°, however, when the peaks were assigned as a disordered component of the methoxy group, the angle around the C22 atom was ~101° which is significantly smaller than the expected geometry. Without disordered components, the angle around the C22 atom is ~125°.

The disordered ring of the **bpe** was found near the solvent DMF and water molecules within the structure. The disordered rings suggest that the pyridyl ligand facilitates movement of the solvent molecules. The

equatorial half **bpe** ligand does not exhibit any disorder. The ASU contains one uncoordinated DMF and one uncoordinated water solvent molecule, depicted in stick model, both with 50% occupancy.

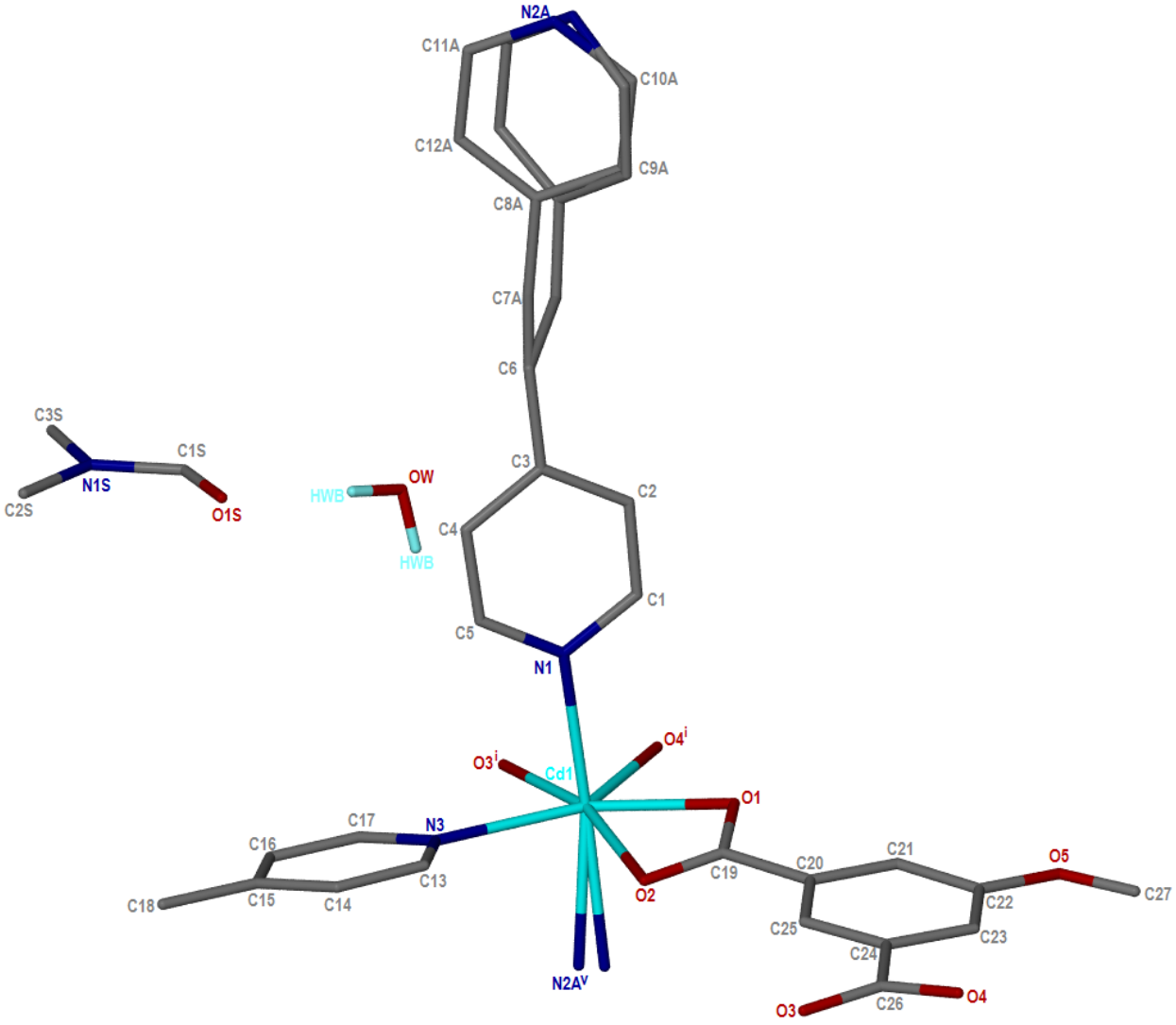

Figure 4.5 Full coordination environment of the Cd(II) ion of **3**. For clarity, all hydrogen atoms, except those found on the water molecules, have been removed. All atoms in the ASU have been labelled except those of part B of the disordered **bpe** ligand.

Table 4.2 Summary of bond lengths of atoms coordinated to Cd metal cation of **3**

Bond	Length (Å)	Bond	Length (Å)
Cd–O1	2.279(3)	Cd–N1	2.377(3)
Cd–O3^{i}	2.514(2)	Cd–N2B^{v}	2.408(6)
Cd–O2	2.650(2)	Cd–N2A^{v}	2.360(4)
Cd–O4^{i}	2.358(2)	Cd–N3	2.340(3)

4.2.2.2 $[Cd(\mu_2\text{-nia})(\mu_2\text{-bpee})_{1.5}]_n \cdot n$DMF (4)

The crystal structure obtained for **4** will be compared to **3** and to that of a similar compound $[Cd(bpe)_{1.5}(nbdc)]_n \cdot n$DMF (which will hereafter be referred to in this text by its CSD code **JECRAN**), reported by Tahier and Oliver.[85]

Compound **4** crystallised in the monoclinic crystal system and the space group *C*2/*c*. **JECRAN** is reported to crystallise in the triclinic crystal system and the space group *P*-1. **Figure 4.6** shows the complete coordination sphere of **4** in which only the asymmetric unit (ASU) atoms are labelled except part B of the disordered **bpee** ligand component. The ASU of **4** consists of a Cd(II) cation, one deprotonated **nia** ligand and one complete, disordered **bpee** ligand and one half, non-disordered **bpee** ligand. Part A of the disordered half of the **bpe** ligand has as s.o.f. of 0.49, thus part B has a s.o.f. of 0.51. The ASU also contains two uncoordinated, disordered DMF molecules with a s.o.f. of 0.52 and 0.48, respectively.

Cd1 exhibits a distorted octahedral coordination geometry and is coordinated to the O1, O2, $O4^{i}$ oxygen atoms on the carboxylate functional groups of the **nia** ligand and the N2B, $N3B^{vi}$, N2A, N4 and $N3A^{vi}$ nitrogen atoms on the **bpee** ligand (where i = x, -1+y, z and vi = 1/2+x, 3/2-y, 1/2+z). The 2+ charge on the Cd cation is counterbalanced by the 2- charge provided by the two, deprotonated carboxylate functional groups of the **nia** ligand. This coordination sphere is the same as that of **JECRAN** except that the bipyridyl ligand in **JECRAN** is one disordered and one half, non-disordered **bpe**. Both **4** and **JECRAN** show different coordination geometries to **3**. The angles present around the Cd cation of **4** range from 54.38(8)° – 173.9(7)°.

The DMF solvents are rotated around a 2-fold rotation axis with the C1SA and C3SA atoms of the DMF molecule labelled as Part A lying on the rotation axis. As a consequence of this symmetry, although there are two DMF molecules found within the structure, they occur with approximately 0.50 s.o.f. each to account for the single DMF in the formula of compound **4**.

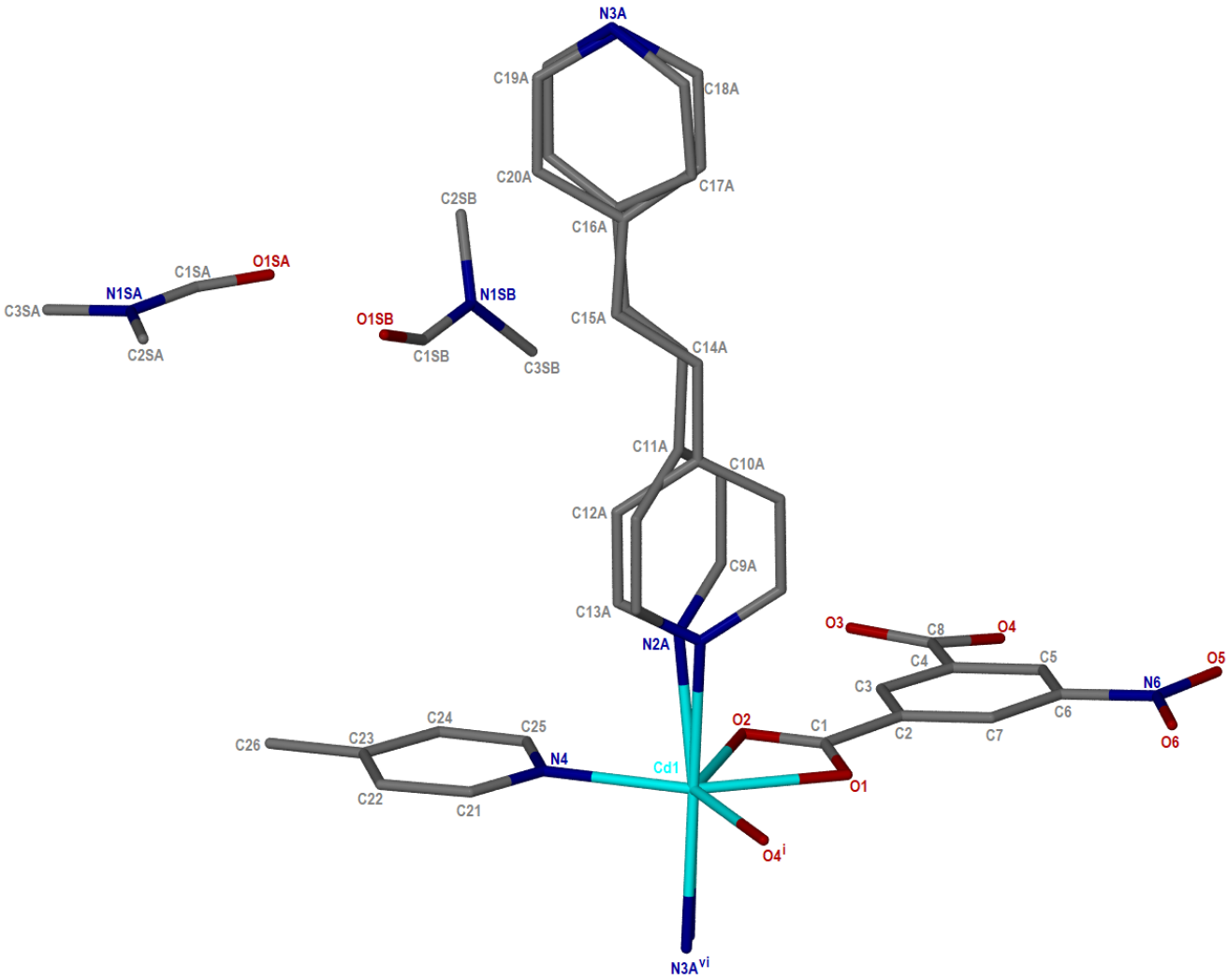

Figure 4.6 Full coordination environment of the Cd ion of **4**. For clarity, all hydrogen atoms have been removed. All atoms in the ASU have been labelled except those of part B of the disordered **bpee** ligand.

Table 4.3 Summary of bond lengths of atoms coordinated to Cd metal cation of **4**

Bond	Length (Å)	Bond	Length (Å)
Cd–O1	2.355(2)	Cd – N2B	2.329(5)
Cd–O2	2.481(2)	Cd – N2A	2.370(6)
Cd–O3^{i}	2.664(2)	Cd – N3A^{vi}	2.31(3)
Cd–O4^{i}	2.278(2)	Cd – N3B^{vi}	2.42(3)
Cd–N4	2.327(3)		

4.2.3 Crystal Packing

The extended frameworks of **3**, **4** and **JECRAN** are similar and can be described in conjunction. The Cd ion is coordinated to a bipyridyl ligand along the axial direction and to the carboxylate ligand along the equatorial direction to form a 2-periodic coordination layer. The single coordination layers are bridged to the neighbouring layer by the equatorially coordinated bipyridyl ligand. Coordination through the equatorial bipyridyl ligand is finite and limits extension to form a single bilayer (**Figure 4.7** and **Figure 4.8**). As the coordination environment allows for infinite extension in the direction of the equatorial carboxylate ligands and the axially coordinated bipyridyl ligands, but not in the direction of the equatorially coordinated bipyridyl ligands, these Cd MOFs are considered 2-periodic MOFs. However, the bilayers have a measure of 'thickness' through the finite coordination of the equatorial bipyridyl ligands, and are thus classed as 2-periodic, 3D MOFs (using the same convention as that of the review written by Carlucci, Proserpio, Blatov, et al.).[16]

These isoreticular structures have some conformational differences when viewed along their common views. The view along the edge-on direction of the bilayer (**Figure 4.7** (a) and **Figure 4.8** (a)) shows the rectangular channels along the direction of the equatorial carboxylate ligand. The dimensions of the channels, indicated on the figure, were measured from Cd to Cd along the axially and equatorially bridging bipyridyl ligands. In **3**, the channels (13.91 Å x 14.08 Å) are slanted when compared to **4** (14.03 Å x 14.04 Å) and **JECRAN** (13.83 Å x 14.09 Å). When the bilayers are rotated ~90° left around the vertical axis down the page, the face-on view (**Figure 4.7** (b) and **Figure 4.8** (b)) through which the **sql** motif can be seen, shows a distinct conformational difference in the axial bipyridyl ligands on the MOFs. In **3** the axial **bpe** ligands show distinct alternating left/right rotation over half the ligand, while the common view of **4** shows that the alternating **bpee** also shows slight comparatively left/right conformational changes. These conformational changes in axial bipyridyl ligands do not occur in **JECRAN.** The length when measured from Cd to Cd through the carboxylate ligand is 10.20 Å, 10.16 Å and 10.23 Å in **3**, **4** and **JECRAN**, respectively. The edge-on view along the third common view shows

the hexagonal channels propagating along the direction of the carboxylate ligands in **3** and **4** (**Figure 4.7** (c) and **Figure 4.8** (c)).

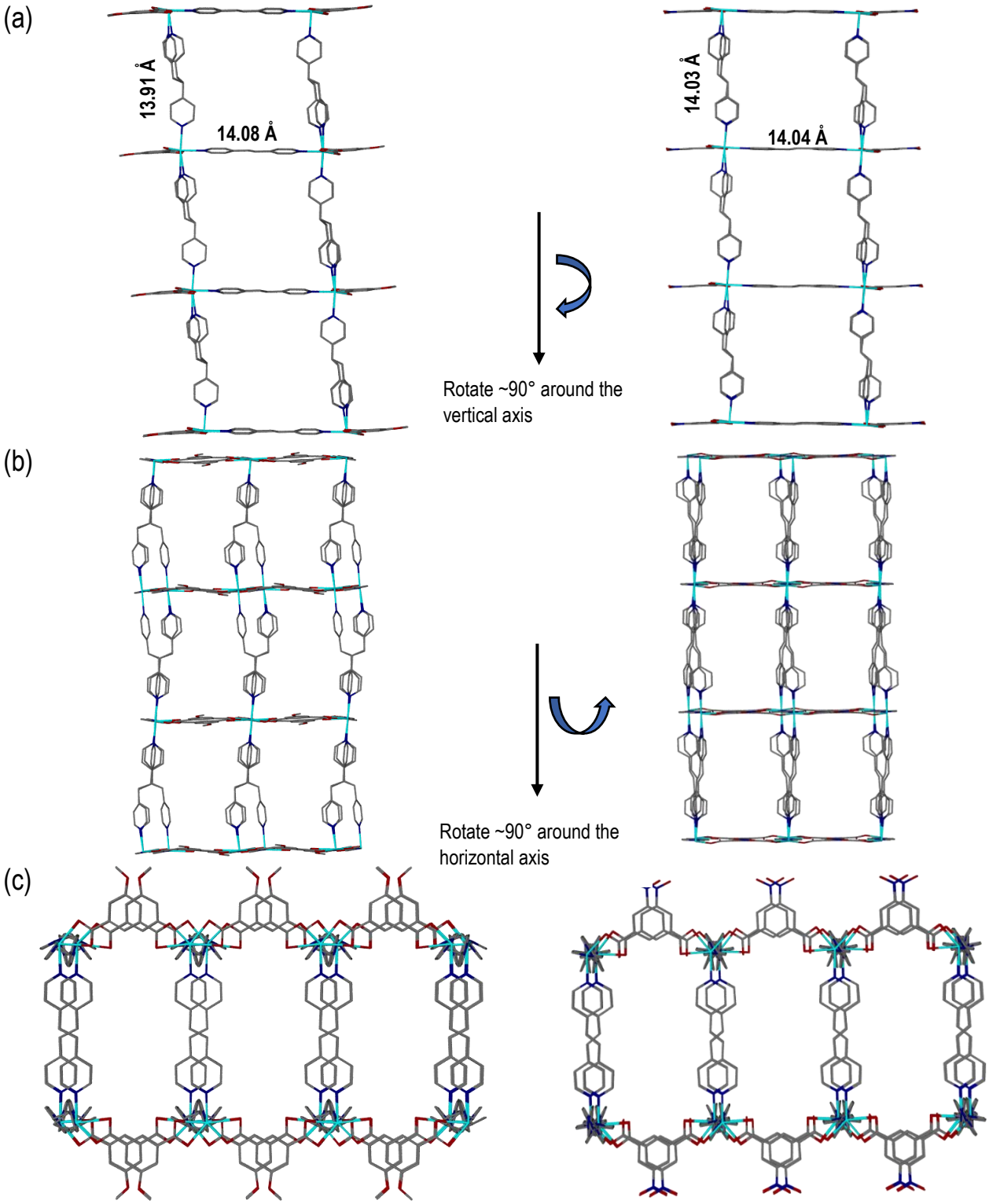

Figure 4.7 Packing diagram of the common view of a single bilayer of **3** (left) and **4** (right) showing the (a) edge-on view depicting the rectangular channels, (b) face-on view showing the **sql** motif and (c) edge-on view showing the hexagonal channels. Hydrogen atoms and solvents have been removed for clarity.

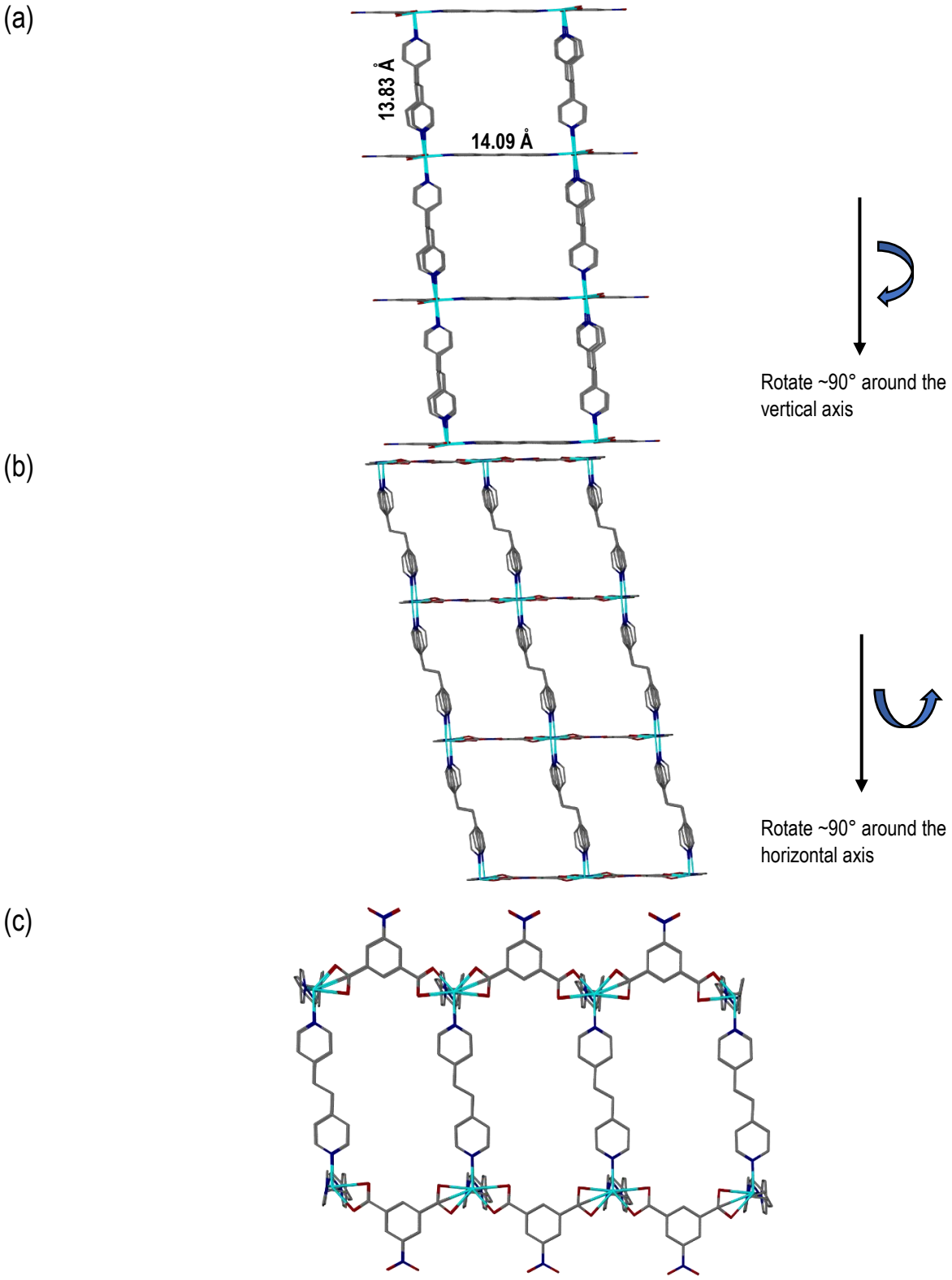

Figure 4.8 Packing diagram of **JECRAN** showing the (a) edge-on view depicting the rectangular channels, (b) face-on view showing the **sql** motif and (c) edge-on view showing the hexagonal channels. Hydrogen atoms and solvents have been removed for clarity.

To simplify crystal packing analysis and description, the node and spacer convention has been used. The centroids of the benzene rings in the **mia** and **nia** ligands as well as the Cd(II) ion centres have been taken as the nodes while the bonds connecting the metal centres to the carboxylate ligands' centroids and to neighbouring metal centres are considered as spacers.

The entanglement of **3**, **4** and **JECRAN**, which can be compared to the links of a chain, shows that one bilayer is catenated with one bilayer to its left and another bilayer to its right (**Figure 4.9**). Hence, the number of motifs with which one bilayer is catenated, i.e. the degree of catenation (Doc) is 2 and the number of motifs that need to be removed to separate the array into 2 distinct parts, i.e. the Index of separation (Is) is 1.

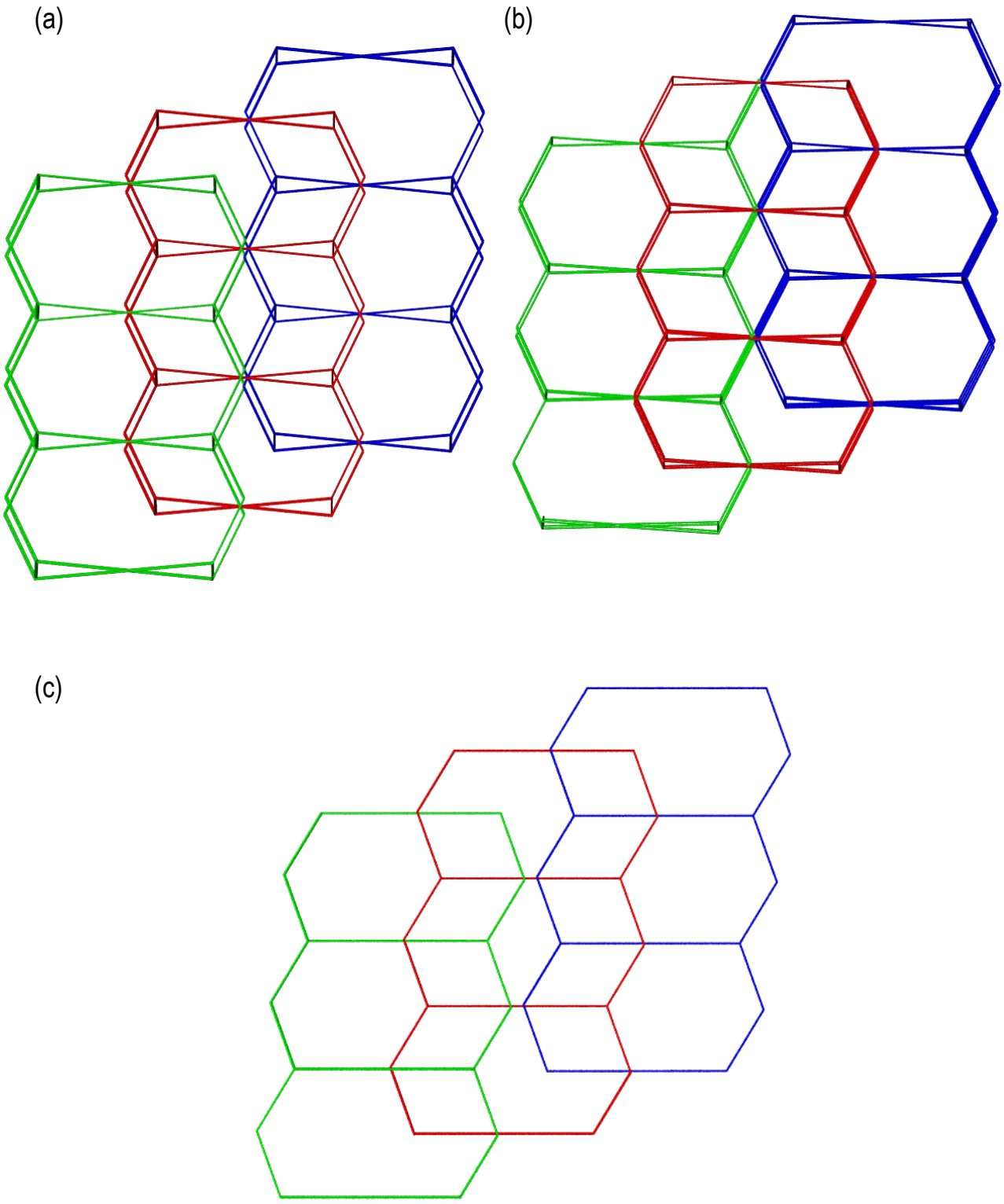

Figure 4.9 Node and spacer depiction of the entanglement of (a) **3**, (b) **4** and (c) **JECRAN** along hexagonal channels.

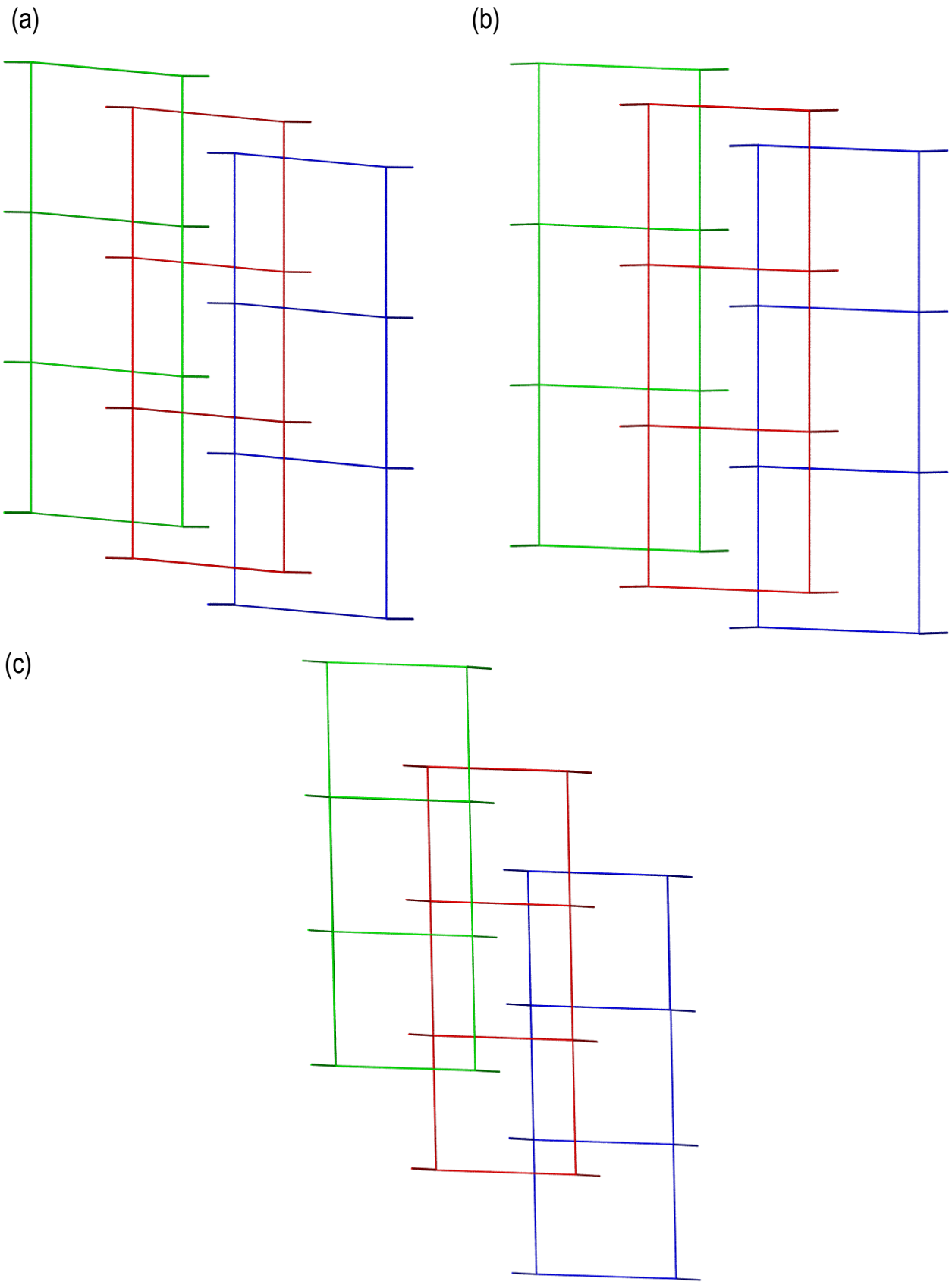

Figure 4.10 Node and spacer depiction of the edge-on view of the rectangular channels of (a) **3**, (b) **4** and (c) **JECRAN**.

4.2.4. Void Space Analysis

Despite the similar crystal packing and network topologies, SCXRD analysis revealed differences in the potential void spaces amongst all the compounds (**Table 4.4**). SCXRD analysis revealed that compound **3** has solvent molecules occupying isolated, single pockets within the structure while **4** has solvent molecules occupying isolated, double pockets when disordered component A is isolated or channels when disordered component B is isolated. This result is surprising as the SCXRD analysis reported for **JECRAN** shows that DMF molecules are contained within long channels along the *b*-axis of the structure. Given that the difference between **4** and **JECRAN** is a double or single bond, respectively, in the bipyridyl ligand, and the difference between **3** and **JECRAN** is a methoxy- or nitro- functional group, respectively, in the 5-position of carboxylate ligand, the marked difference in void space is somewhat unexpected. The program MERCURY was used to model the void space per unit cell (using a probe of radius 1.2 Å) described above when the solvent was artificially removed. The individual disordered components of each compound were also isolated using MERCURY.

The potential void spaces per unit cell in **3**, found to be isolated single pockets, are larger when the disordered **bpe** ligand component part A was isolated (10.1%; 534 $Å^3$) (**Figure 4.11**) than they are when the disordered **bpe** ligand component part B is isolated (7.4%; 390 $Å^3$). In **4**, the isolated double pocket potential void spaces are smaller for the disordered **bpee** ligand component Part A (10.2%; 554 $Å^3$) (**Figure 4.12** (a)). Interestingly, in **4**, the potential void spaces that formed in long channels along the *c*-axis when the disordered **bpee** ligand component part B was isolated (17.9%; 977 $Å^3$) (**Figure 4.12** (b)) also had the largest void space of **3**, **4** and **JECRAN**. The potential void spaces of **JECRAN**, which formed as channels along the *b*-axis, were largest for the disordered **bpe** ligand component part A (13.4%, 182 $Å^3$) when compared to the disordered **bpe** ligand component part B (11.4%, 159 $Å^3$).

Table 4.4 Table to summarise potential void spaces for **3**, **4** and **JECRAN**

Compound	**3**		**4**		**JECRAN**	
Volume of unit cell (Å^3)	**5302.81**		**5445.36**		**1363.02**	
Disordered component	**A**	**B**	**A**	**B**	**A**	**B**
s.o.f. of disordered component	**0.50**	**0.50**	**0.49**	**0.51**	**0.61**	**0.39**
Description	Isolated single pockets		Isolated double pockets	Channels along *c*-axis	Channels along *b*-axis	
Potential void space percentage per unit cell (%)	10.1	7.4	10.2	17.9	13.4	11.4
Potential void space per unit cell (Å^3)	534	390	554	977	182	159
Weighted Average potential void space per unit cell (%, Å^3)	8.8, 462		14.1, 770		12.6, 173	

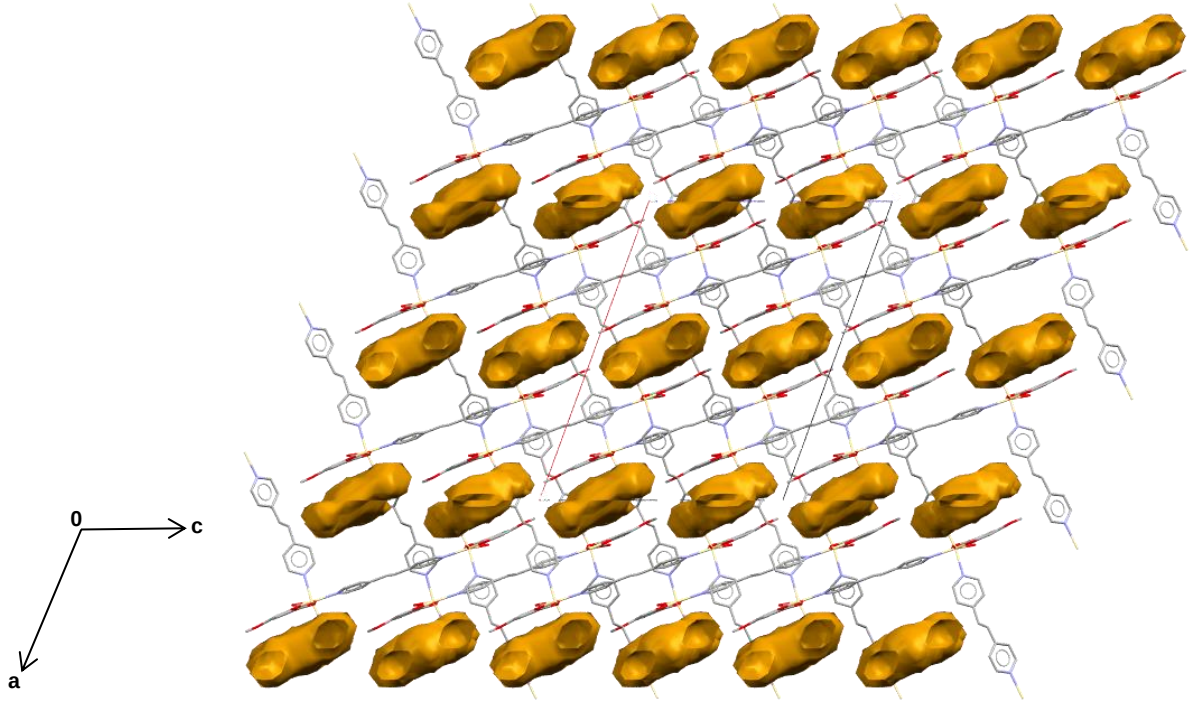

Figure 4.11 Crystal packing for **3** showing potential void map of isolated single pockets along the *c*-axis for when **bpe** disordered ligand component B is isolated. Hydrogen atoms have been omitted for clarity.

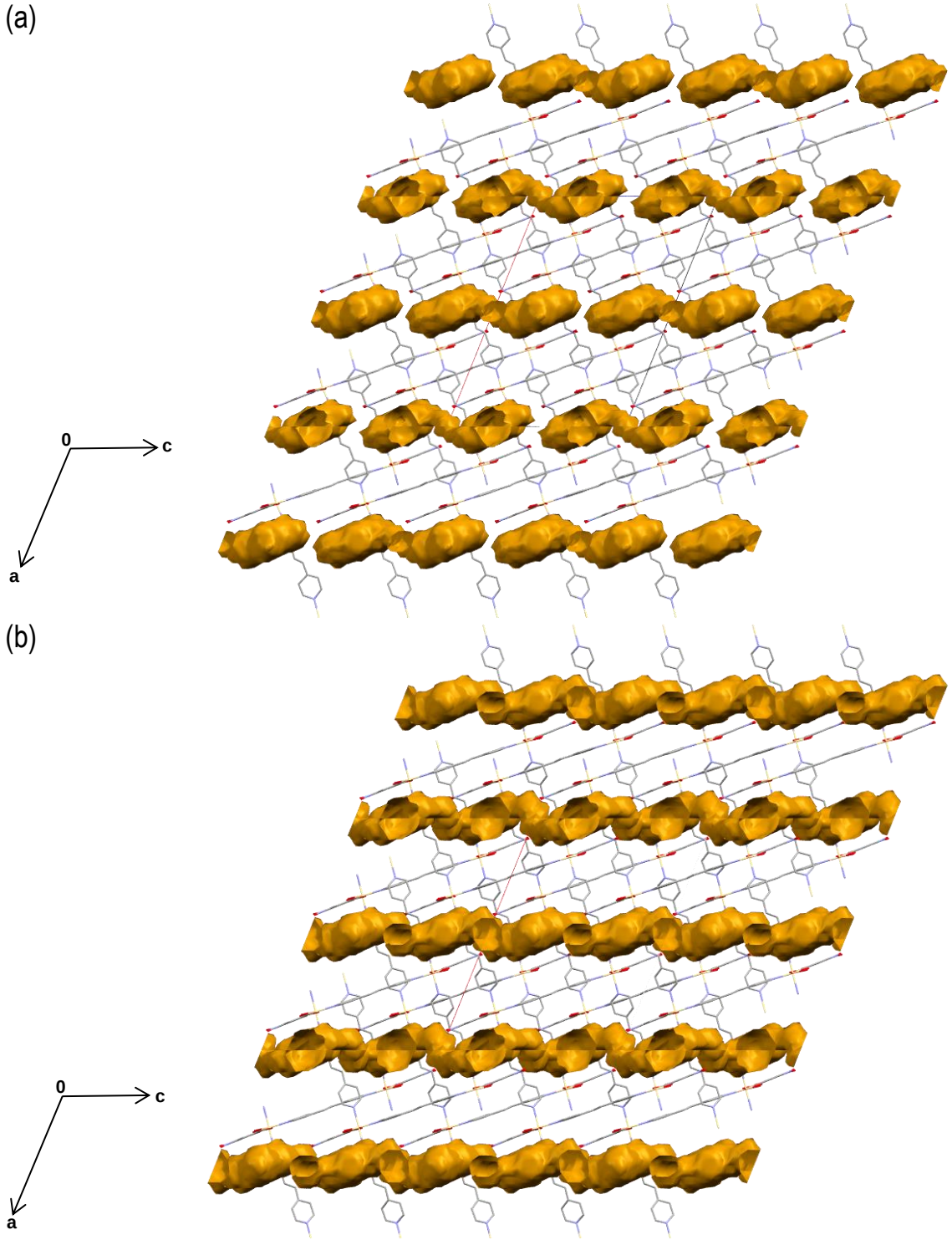

Figure 4.12 Crystal packing for **4** showing potential void map of (a) isolated double pockets along *c*-axis for disordered **bpe** ligand component A and (b) channels along *c*-axis for disordered **bpe** ligand component B. Hydrogen atoms have been omitted for clarity.

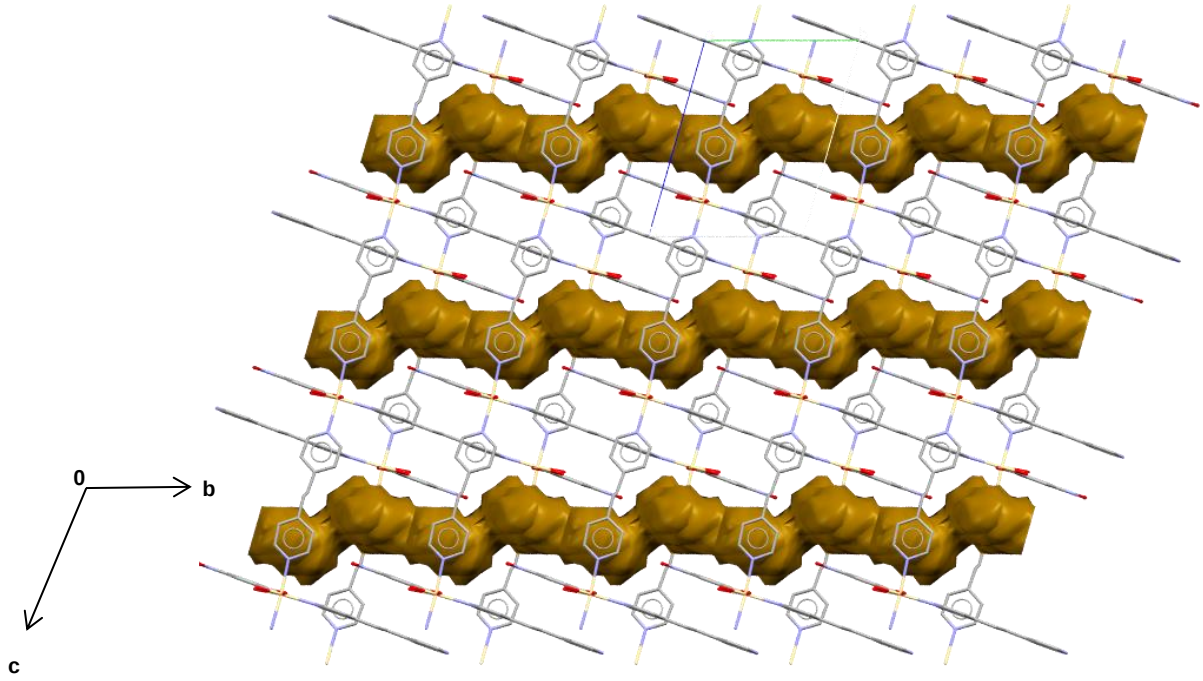

Figure 4.13 Crystal packing for **JECRAN** showing potential void map of channels along *b*-axis for disordered **bpe** ligand component A. Hydrogen atoms have been omitted for clarity.

4.2.5 Hydrogen Bonding

Assessment of the hydrogen bonding environment in **3** revealed hydrogen bonding between the uncoordinated solvent water molecule and the uncoordinated DMF solvent molecule as well as the carboxylate functional group in the **mia** ligand. Hydrogen bonding occurred between the framework and the water molecule *via* OW–HWB···O3 while hydrogen bonding occurred between the solvent molecules *via* OW–HWA···OS1 as depicted in **Figure 4.14**.

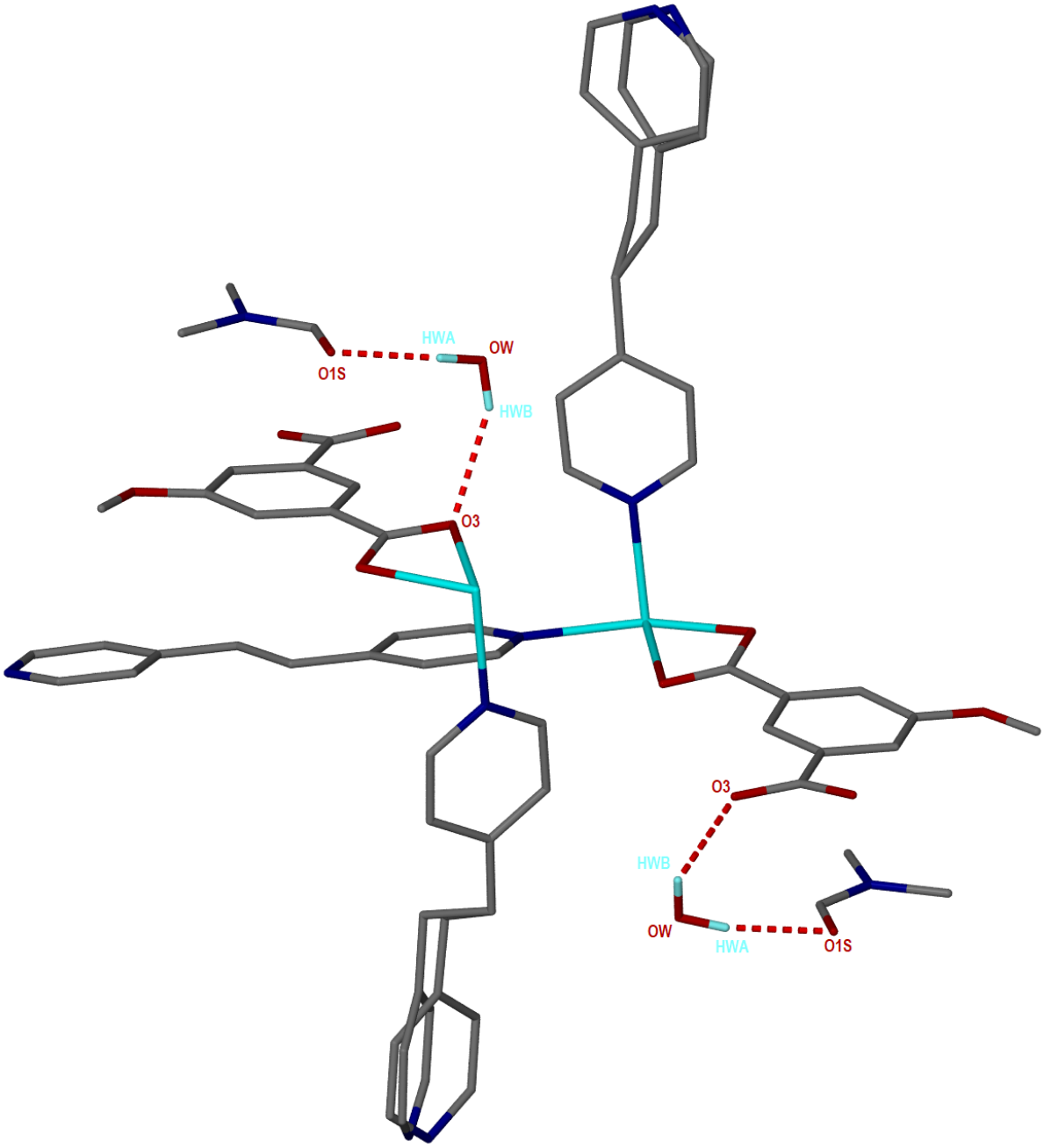

Figure 4.14 Hydrogen bonding in structure of **3** showing uncoordinated water molecules hydrogen bonding to uncoordinated DMF molecules and the carboxylate functional group in **mia** ligand.

PLATON analysis indicated no classical hydrogen bonding between the solvent and framework of **4** which is similar to what was found in **JECRAN**. Intermolecular and intramolecular bonds, thought to impart geometry and stability to the frameworks, are detailed in **Table 4.5.1** – **Table 4.5.3**. It is noteworthy that the intermolecular and intramolecular interactions are largely C–H···O interactions in **3**, **4** and **JECRAN**.

Table 4.5.1 Hydrogen bond distances and angles for **3**

Donor–H···Acceptor	D-H···A (Å)	H···A (Å)	D···A (Å)	D–H···A (°)
OW–HWA···O1S	0.87	2.07	2.918(9)	166
OW–HWB···O3	0.87	2.26	3.050(7)	151
C2S–H2SC···O1S	0.98	2.41	2.83(1)	105
C2S–H2SA···O5	0.98	2.54	3.44(1)	152
C2S–H2SC···O1S (intra)	0.98	1.84	2.34(1)	108
C2–H2···O4	0.95	2.52	3.455(4)	166
C10B–H10B···O1S	0.95	2.35	3.07(1)	133
C5–H5···N3 (intra)	0.95	2.59	3.237(4)	125
C11B–H11B···O2 (intra)	0.95	2.48	3.168(8)	129
C7B–H7BA···N3	0.99	2.50	3.302(9)	138
C13–H13···O2 (intra)	0.95	2.42	3.157(5)	134
C17–H17···O3 (intra)	0.95	2.46	3.168(4)	131

Table 4.5.2 Hydrogen bond distances and angles for **4**

Donor–H···Acceptor	D-H···A (Å)	H···A (Å)	D···A (Å)	D–H···A (°)
C14B–H14B···O1	0.95	2.46	3.39(2)	168
C18B–H18B···O4	0.95	2.58	3.21 (1)	124
C21–H21···O3 (intra)	0.95	2.43	3.182(4)	136
C25–H25···O2 (intra)	0.95	2.43	3.147(5)	133

Table 4.5.3 Hydrogen bond distances and angles for **JECRAN**[85]

Donor–H···Acceptor	D-H···A (Å)	H···A (Å)	D···A (Å)	D–H···A (°)
C4A–H4A···O1S1	0.95	2.60	3.418(2)	153
C12A–H12A···O1S1	0.95	2.48	3.3735(2)	156
C5A–H5A···O6D	0.95	2.40	3.1510(2)	136
C9A–H9A···O4D	0.95	2.48	3.4117(2)	168
C1–H1C···O2D (intra)	0.95	2.39	3.1114(2)	132
C5–H5C···O3D (intra)	0.95	2.41	3.1704(2)	137

4.3 Desolvation Studies

4.3.1 Variable-Temperature Powder X-Ray Diffraction Studies

The PXRD pattern of **3** at 303 K was a good match with the calculated pattern of **3** indicating the single crystal was representative of the bulk material (**Figure 4.15**). However, a peak at 10.9° in the calculated pattern did not appear in the experimental pattern and double peaks at 15.5° and 15.6° were more intense in the calculated pattern but diminished in the 303 K experimental pattern and were no longer present in the 363 K – 453 K PXRD patterns. There were also additional peaks in the VT–PXRD patterns from 16.1° – 17.6°, indicated on the 303 K PXRD pattern, which appeared as only three peaks in the calculated pattern 16.6° – 18.0°. In this region, the number and intensity of peaks can be seen to increase with increased temperature from 303 K – 453 K (indicated on the 423 K pattern) then reduce from 483 K – 508 K (indicated on the 483 K pattern). This suggests that the loss of solvent occurs with some structural change as reflected by the increased number of peaks. Peaks in the region 9.1° – 9.6° 2θ (indicated on the 303 K pattern) seen up to 453 K reduce to a single peak at 9.3° in the 508 K PXRD pattern while new peaks in the region 11.0° – 13.1° 2θ (indicated on the 453 K pattern) appear in experimental patterns from 453 K – 508 K. The sample retained crystallinity with desolvation up to 508 K. The calculated pattern of **3** was a good match for the 303 K experimental pattern indicating the single

crystal to be representative of the bulk material. **3** retained crystallinity with desolvation up to 508 K. The change in pattern at elevated temperatures indicates a structural change as the sample undergoes desolvation.

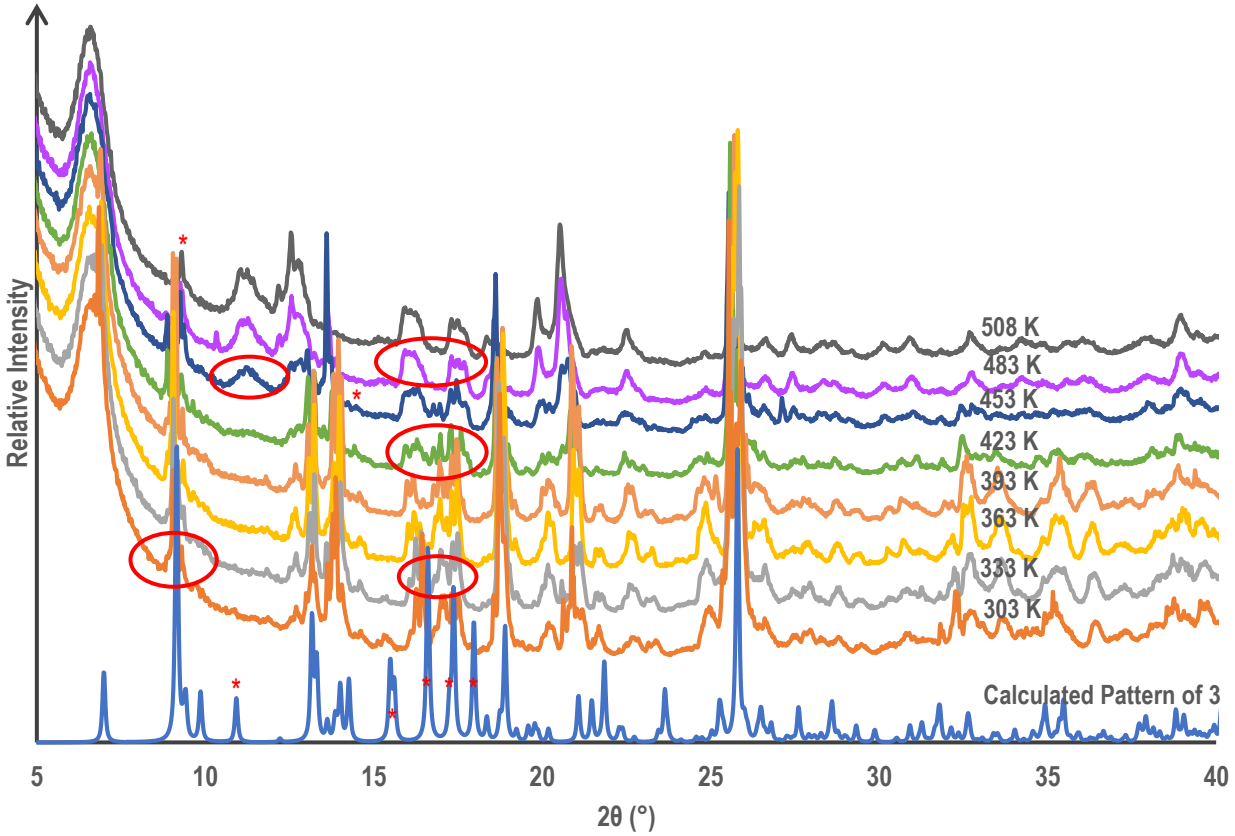

Figure 4.15 VT–PXRD patterns against the calculated pattern for **3** in temperature range 303 – 508 K. Red asterisks and circles indicate selected peaks and peak ranges specified in **section 4.3.1**.

Comparison of the VT–PXRD patterns from 303 K – 323 K and the calculated pattern of **4** (**Figure 4.16**) correspond well besides a peak at 15.9° and a small shoulder at 17.4° in the 303 K pattern not visible in the calculated pattern. Changes in the PXRD profile can be seen from 363 K with decreased intensity for the peaks at 9.9°, 10.9°, 15.3°, 16.4° and 17.9° (indicated with red asterisks) and increased intensity for the peaks at 11.4°, 15.2°, 16.0° and 17.0° (indicated with blue asterisks). This trend of these specific peaks increasing, and decreasing can be seen as temperature increases until 523 K where the specified

decreasing peaks are completely diminished and increasing peaks are more intense than at 303 K or in the calculated pattern. The calculated pattern of **4** was a good match for the 303 K experimental pattern indicating the single crystal to be representative of the bulk material. **4** retained crystallinity with desolvation up to 523 K. The change in pattern at elevated temperatures indicates a structural change as the sample undergoes desolvation.

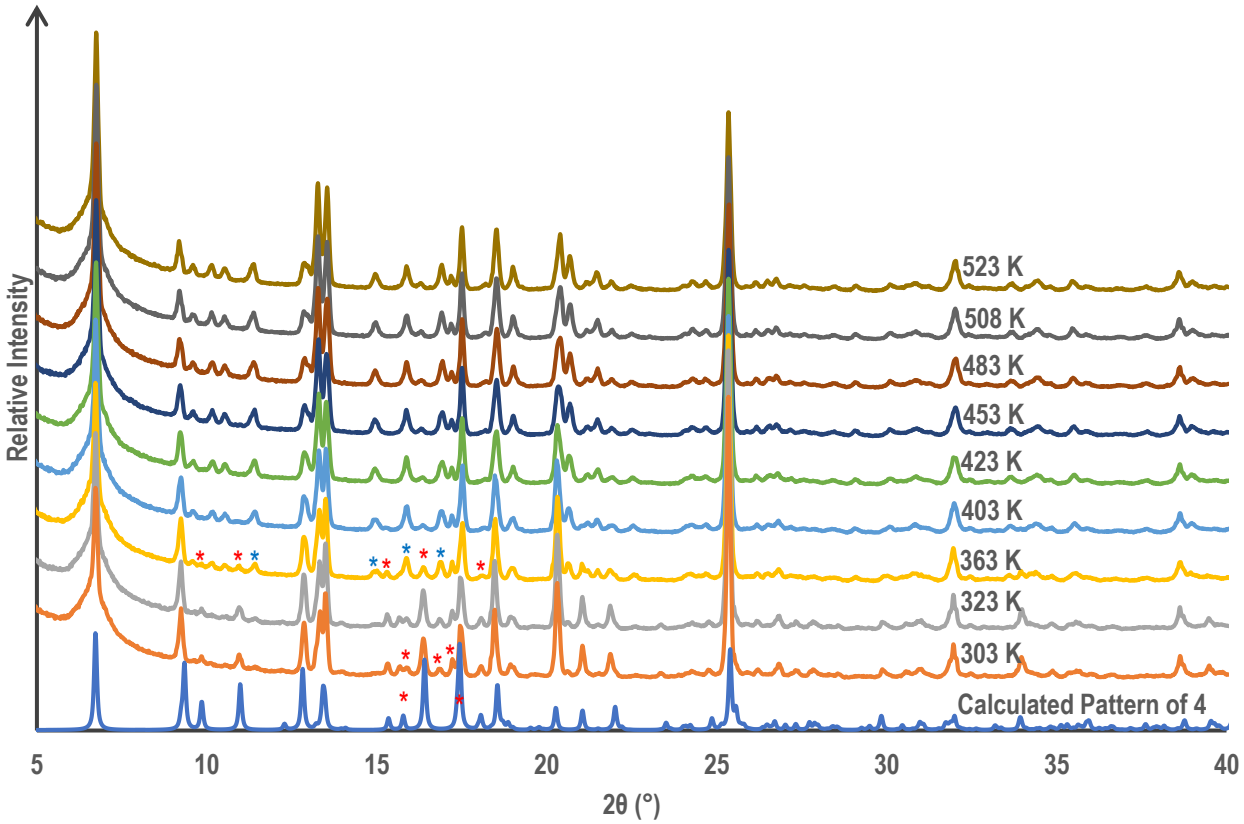

Figure 4.16 PXRD patterns against calculated pattern for **4** in temperature range 303–523 K. Red asterisks indicate selected peaks as specified in **section 4.3.1**. For clarity, increasing peaks specified for 363 K have been indicated with blue asterisks.

4.3.2 Thermal Analysis

4.3.2.1 Thermogravimetric and Differential Scanning Calorimetry Analysis

Thermogravimetric analysis (TGA) and differential scanning calorimetry (DSC) were employed to investigate the thermal stability of **3** and **4**. The overlay of the thermograms of these experiments for **3** can be seen in **Figure 4.17**. The TGA thermogram shows a gradual mass loss of 7.1% within the temperature range of 303 K– 522 K. This accounts for the total loss of half a DMF molecule and half a water molecule as is present within the ASU (calculated 7.2%). Thereafter, decomposition occurred over the remainder of the analysis. The first endothermic event in the DSC thermogram is a two-step endotherm of 68.39 J g^{-1} with temperatures peak at 369 K and 436 K. The next endotherm occurred with an onset of 523 K, ~100 K before the onset of decomposition in the TG thermogram. This endotherm is possibly an indication of a phase change associated with desolvation. The DSC analysis was not allowed to continue until decomposition, hence the total heat input g^{-1} of the endotherm could not be accurately reported. Nonetheless, the temperatures of the endotherms confirm the observations from TG analysis.

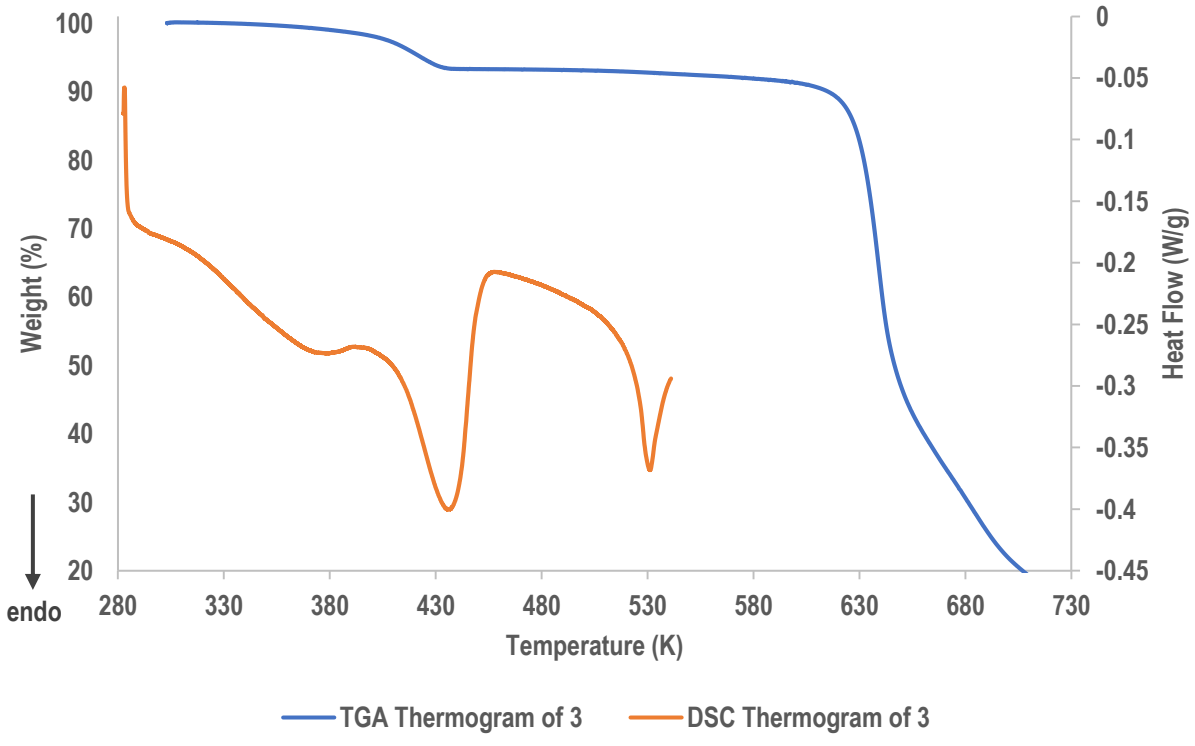

Figure 4.17 Overlay of the TGA (blue) and DSC (orange) thermograms for **3**.

In the case of **4**, the single crystal data showed the presence of two half occupied DMF solvent molecules which accounted for 10.9% of the ASU mass. TG analysis revealed a gradual mass loss of the expected 10.9% in the temperature range of 293 K – 586 K (**Figure 4.18**). Thereafter, decomposition occurred throughout the remainder of the analysis. DSC analysis confirms this observation as the DSC thermogram shows a broad endotherm throughout the entire analysis ranging from 293 – 611 K. The DSC was halted before the onset of decomposition.

Comparatively, the TGA thermogram of **JECRAN** showed a one-step mass loss of its DMF solvent over a reported temperature range of 323 K – 513 K with multistep endotherm peaks in the DSC over the range 348 K – 533 K attributed to possible structural changes as observed through changes in its VT–PXRD patterns.[86]

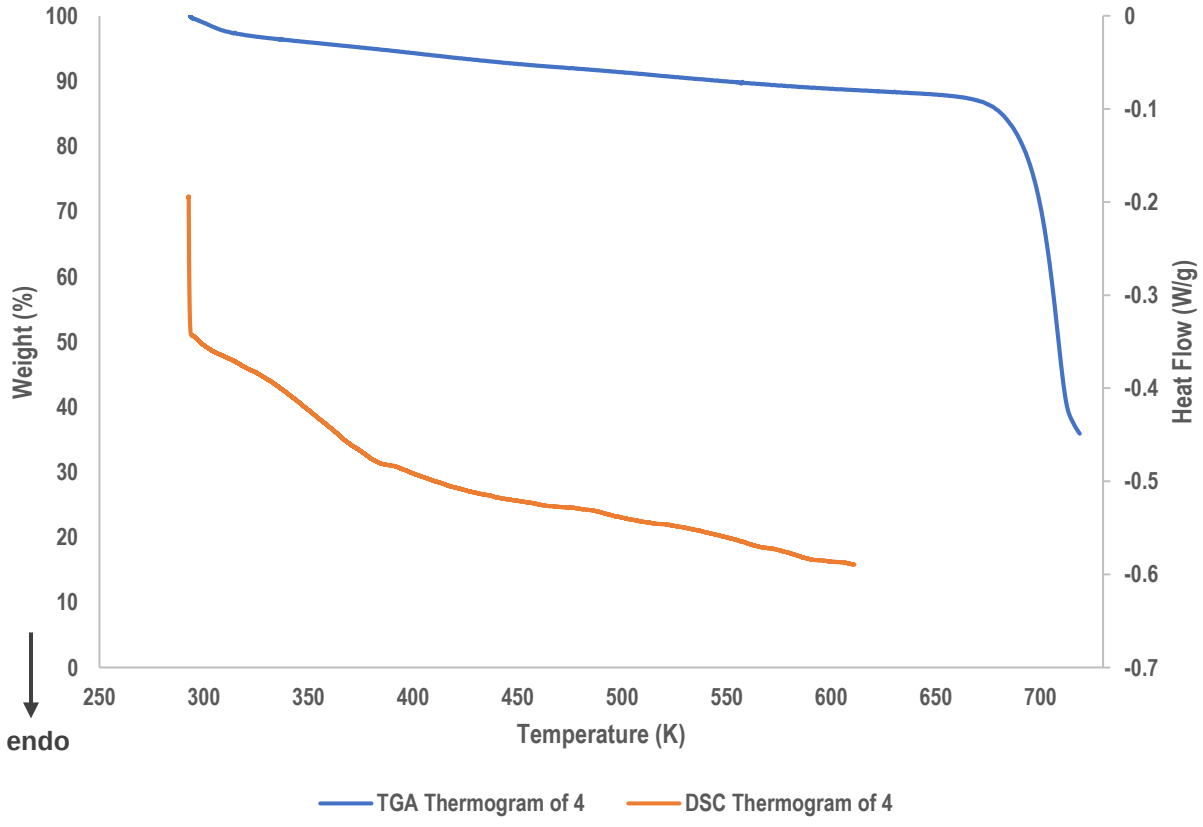

Figure 4.18 Overlay of the TGA (blue) and DSC (orange) thermograms for **4**.

4.3.2.2 Hot stage microscope analysis

Crystals of **3** were covered in silicon oil to allow solvent loss to be observed (as bubbling) over a heating temperature range of 297 K – 654 K (**Figure 4.19**). As heating occurred, the crystal showed longitudinal cracks at 407 K (b) before desolvation bubbling at 423 K (c). At 459 K (d), the crystals were completely opaque and beginning to disintegrate. The crystals continued to collapse until bubbling stopped at 567 K (e), where after, the onset of decomposition is evident at 654 K (f). HSM confirmed the observation of an ~100 K difference in temperature between the end of desolvation and the onset of decomposition of **3**.

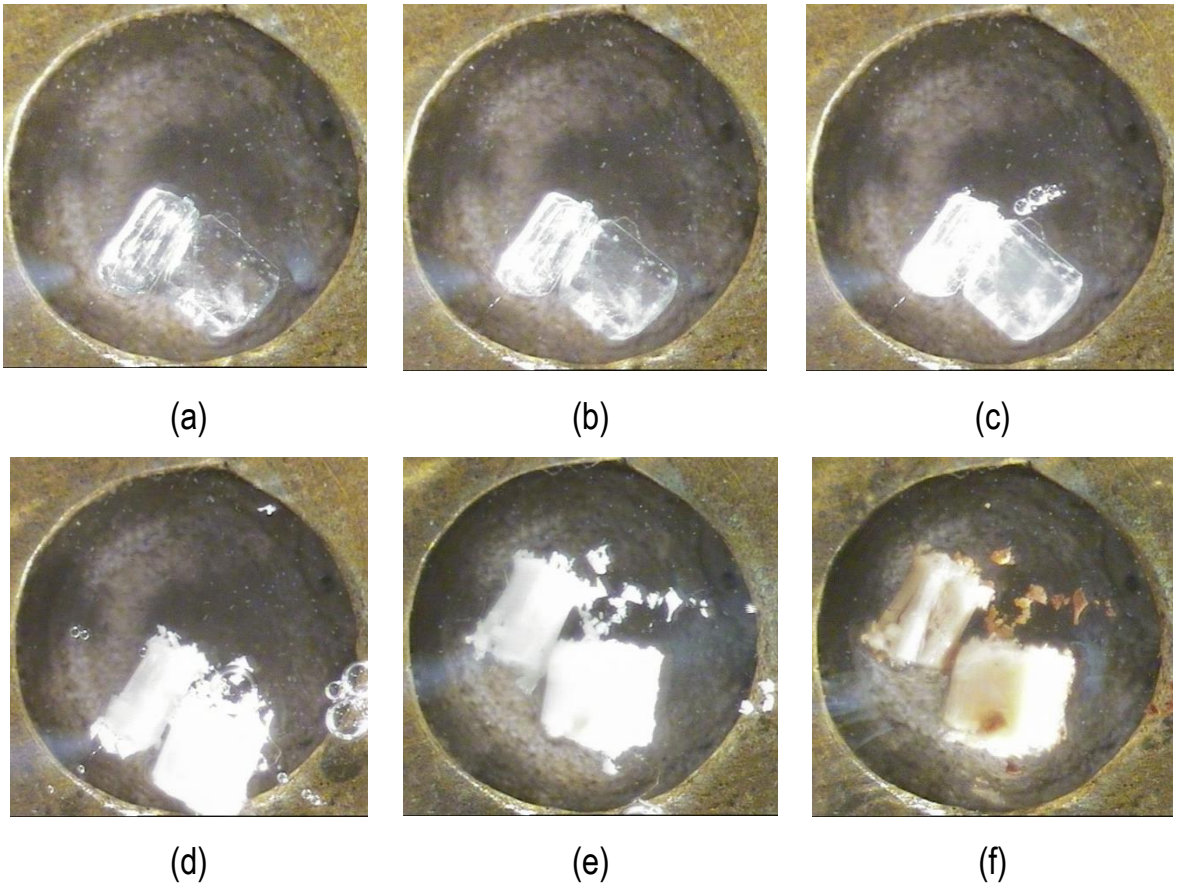

Figure 4.19 HSM images of **3** at (a) 297 K, (b) 407 K, (c) 423 K, (d) 459 K, (e) 567 K and (f) 654 K

Crystals of **4** were covered in silicon oil to allow solvent loss to be observed over a heating temperature range of 297 K – 677 K (**Figure 4.20**). As heating occurred, the crystal shows longitudinal cracks at 375 K (b). Although not seen as bubbling, the longitudinal cracking continued throughout the desolvation

temperature range (as determined through TGA) and is taken as indication of desolvation. This observation coincides with observation in TG analysis as desolvation occurs gradually over a long heating range without a definitive step. Interestingly, at 473 K (c) many longitudinal cracks disappeared, and the crystal becomes clearer. At 517 K (d) crystal cracking continued with a loss in transparency. The crystals began to decompose, as evidenced by crystal browning, at 614 K (e) with decomposition visible by 677 K (f). The HSM analysis seems to confirm observations from the TGA and DSC thermograms which show gradual mass loss over the desolvation heating range before decomposition.

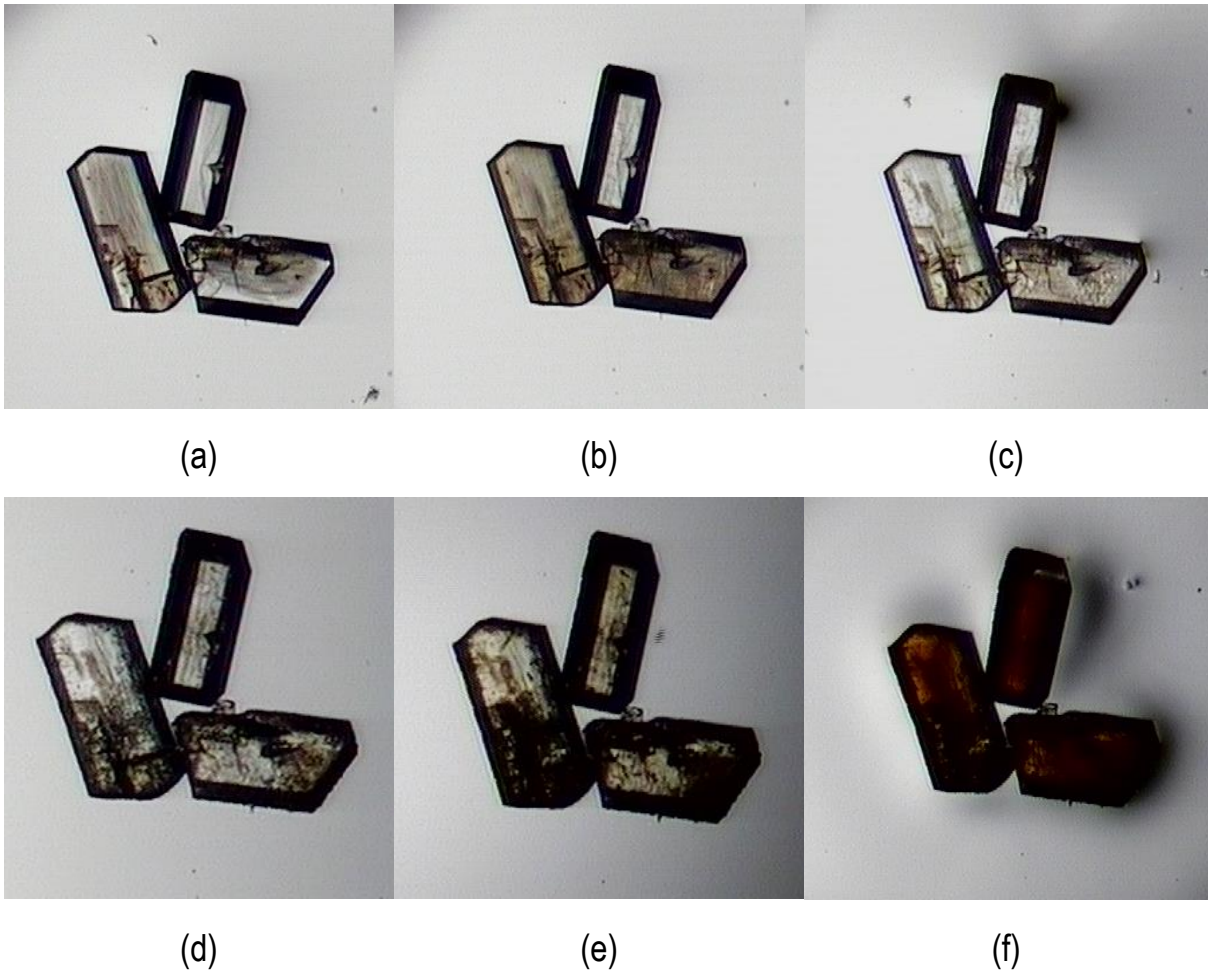

Figure 4.20 HSM of **4** at (a) 297 K, (b) 375 K, (c) 473 K, (d) 517 K, 614 K (e) and 677 K (f)

4.3.3 Single-crystal-to-single-crystal Desolvation Studies

HSM studies indicated that crystals of **4** retained some transparency with the onset of desolvation while crystals of **3** did not. It was suspected that **4** may undergo single-crystal-to-single-crystal transformations that may allow the determination of the evacuated MOF structure.

To access the desolvated samples, crystals of **3** and **4** were heated through various means. Repeated attempts at heating using TGA and HSM equipment as well as heating under vacuum proved unsuccessful for **3** as confirmed through SCXRD which revealed that the DMF molecule was still present within the framework. However, *in situ* heating to 473 K using TGA equipment allowed access to the desolvated structure of **4** as confirmed through SCXRD analysis. The desolvated form of **JECRAN** was acquired through *in situ* heating of a single crystal to 373 K during X-ray data collection.

4.3.3.1 Comparison of desolvated MOF 4 and $[Cd(bpe)_{1.5}{\cdot}nbdc]_n$ (JECROB)

A crystal of desolvated compound **4**, $[Cd(\mu_2\text{-nia})(\mu_2\text{-bpee})_{1.5}]_n$ (**4'**), was selected after evacuation *via* TGA equipment and placed on the Bruker DUO Apex II CCD diffractometer for data collections in the procedure outlined in **section 2.3.1**. The crystal of **4'** collected at 173 K cracked due to desolvation and had to be refined as non-merohedral twin. The twin fraction (BASF value) refined to 0.457. The space group suggested by XPREP for **4'** was *P*-1. The reported space group for **JECRAN** when partially desolvated was *P*-1 collected at 104 K, 298 K and *C2/c* when completely at 373 K. However, the structure of **4'** will be compared to that of the desolvated form of **JECRAN**, $[Cd(bpe)_{1.5}{\cdot}(nbdc)]_n$, hereafter referred to by its CSD reference code **JECROB**, collected at 373 K, as this was the temperature at which **JECROB** was completely desolvated.[85] The full SCXRD collection and unit cell data are presented for both compounds in **Table 4.6**.

Table 4.6 Crystal data and refinements for compounds **4'** and **JECROB** at **373 K**.

	4'	**JECROB (373 K)**[85]
ASU formula	$C_{26}H_{18}N_4O_6Cd$	$C_{26}H_{21}N_4O_6Cd$
Formula weight	594.84	597.87
Temperature/K	173(2)	373(2)
Crystal system	triclinic	monoclinic
Space group	*P*-1	*C2/c*
***a* / Å**	10.1549(12)	27.330(6)
***b* /Å**	11.0157(13)	10.234(2)
***c* / Å**	14.0424(17)	20.922(5)
***α* / °**	108.540(3)	90
***β* / °**	94.696(3)	110.635(7)
***γ* / °**	111.064(2)	90
Volume/Å^3	1355.2(3)	5476(2)
Z	2	8
ρ_{calc}/g cm^{-3}	1.458	1.45
***μ*/mm^{-1}**	0.851	0.842
F(000)	596.0	2408
2θ range for data collection/°	3.138 to 56.776	3.184 to 61.286
Index ranges	-13 ≤ h ≤ 13, -14 ≤ k ≤ 13, 0 ≤ l ≤ 18	-38 ≤ h ≤ 36, -14 ≤ k ≤ 14, -29 ≤ l ≤ 27
Reflections collected	36795	23205
Independent reflections	6393 [R_{int} = n/a R_{sigma} = 0.0475]	8102 [R_{int} = 0.0709, R_{sigma} = 0.0894]
Data/restraints/parameters	6393/0/335	8102/1080/516
Goodness-of-fit on F^2	1.039	1.017
Final R indexes [I>=2σ (I)]	R_1 = 0.0412, wR_2 = 0.1015	R_1 = 0.0608, wR_2 = 0.1558
Final R indexes [all data]	R_1 = 0.0531, wR_2 = 0.1070	R_1 = 0.1198, wR_2 = 0.1884
Largest diff. peak/hole/e Å^{-3}	0.91/-0.74	1.53/-1.10

The space group of **4** changed from *C*2/*c* to *P*-1 with a unit cell volume that quartered, affected by a reduction of the ~20 Å and ~27 Å axes to approximately half their values, when desolvated to **4'**. The ASU of **4'** shows the same connectivity as the ASU of **4** except, whereas **4** showed disorder in the **bpee** ligand with a s.o.f. of 0.49 and 0.51, **4'** shows no disordered component. The dimensions of the framework when measured from Cd to Cd along the axial **bpee** and the equatorial **bpee** showed no significant change, 14.03 Å x 14.04 Å and 14.04 Å x 14.09 Å in **4** (**Figure 4.21** (a)) and **4'** (**Figure 4.21** (b)), respectively, while the dimension when measured from Cd to Cd along the **nia** ligand was 10.16 Å for both structures. There is, however, a more significant change in the hexagonal channels with desolvation to **4'**. The equatorial **bpee** ligands that showed alternating conformation in **4** have just one conformation in **4'** (**Figure 4.23** (a) and (b)). **4'** retained the same **sql** lattice, 2-periodic, 3D motifs with A Doc of 2 and an Is of 1 for **4**.

Similar changes occur in **JECRAN** with desolvation, however, they occur in the opposite way. The space group change for **JECRAN** with desolvation to **JECROB** is *P*-1 to *C2/c* with a quadrupling of the unit cell volume affected by the approximate doubling of the ~13 Å axis as well as the independent doubling associated with the lattice change from a primitive triclinic to *C*-centred monoclinic unit cell. The **bpe** ligand shows disorder in the solvated structure and in the desolvated structure which also shows additional disorder in the carboxylate ligand (probably due to the high temperature data collection). This additional disorder in the carboxylate ligand is not present in **4** and **4'**. The dimensions of the lattice when measured from Cd to Cd along the axial **bpe** and the equatorial **bpe** showed slightly more change, 13.83 Å x 14.09 Å and 14.01 Å x 14.04 Å (**Figure 4.21** (c) and (d)), while the dimension when measured from Cd to Cd along the **nia** ligand was 10.23 Å in **JECRAN** and **JECROB**. Furthermore, whereas the solvated structure showed no alternation in the conformation of the equatorial **bpe** ligand (**Figure 4.23** (c)), the desolvated structure **JECRAN** showed a change in the hexagonal channels along the common view (**Figure 4.22** (d)) effected by the alternation of the conformation of the equatorial **bpe** ligands.

JECROB retained the same **sql** lattice, 2-periodic, 3D motif with Doc = 2 and Is = 1 as described for **4** and **JECRAN**.

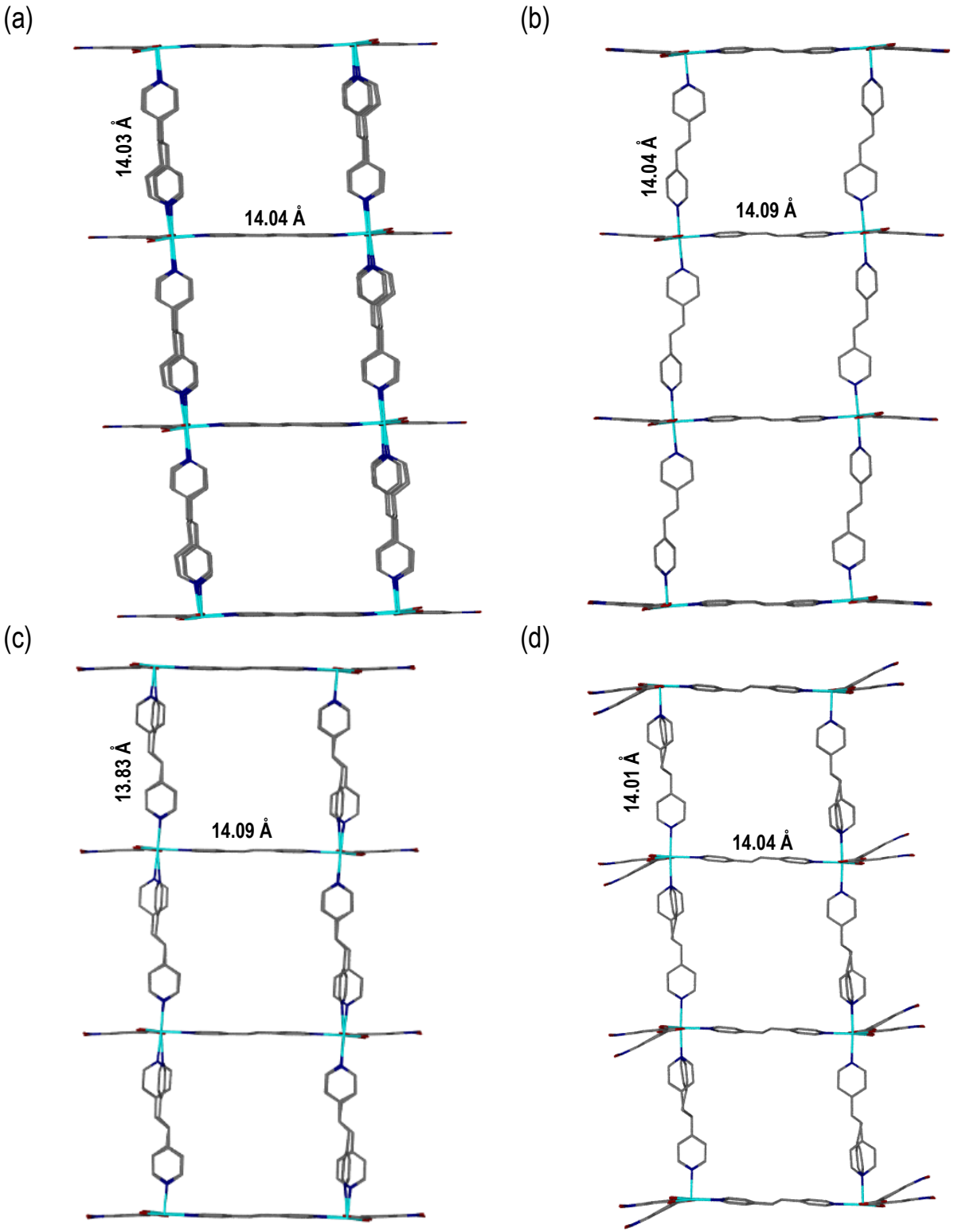

Figure 4.21 Common, edge-on view of **sql** motif of (a) **4**, (b) **4'**, (c) **JECRAN** (104 K) and (d) **JECROB** (373 K). Solvent molecules in (a) and (c) and the hydrogen atoms of all MOFs have been removed for clarity.

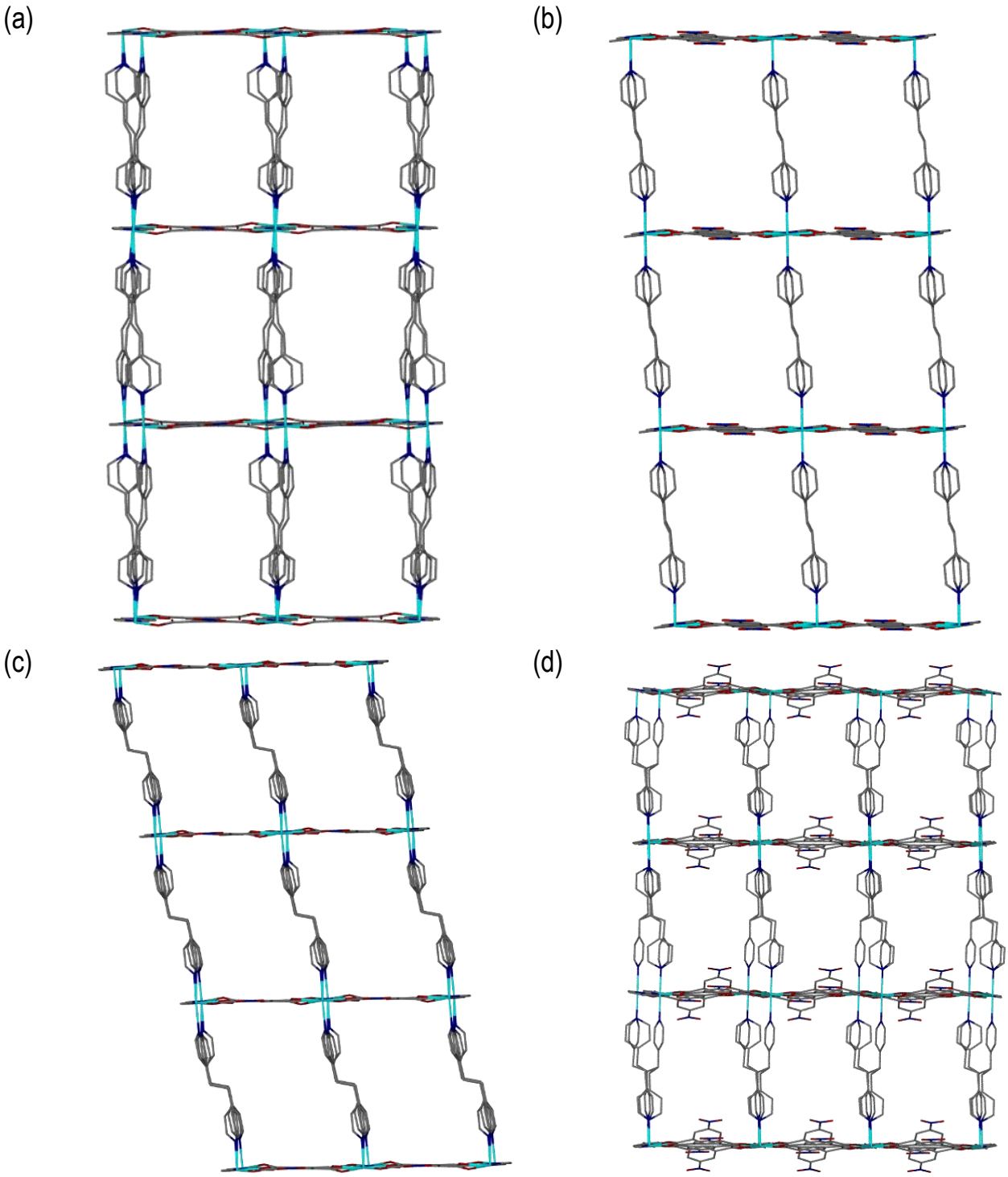

Figure 4.22 Common, face-on view of **sql** motif of (a) **4**, (b) **4'**, (c) **JECRAN** (104 K) and (d) **JECROB** (373 K). Solvent molecules in (a) and (c) and the hydrogen atoms of all MOFs have been removed for clarity.

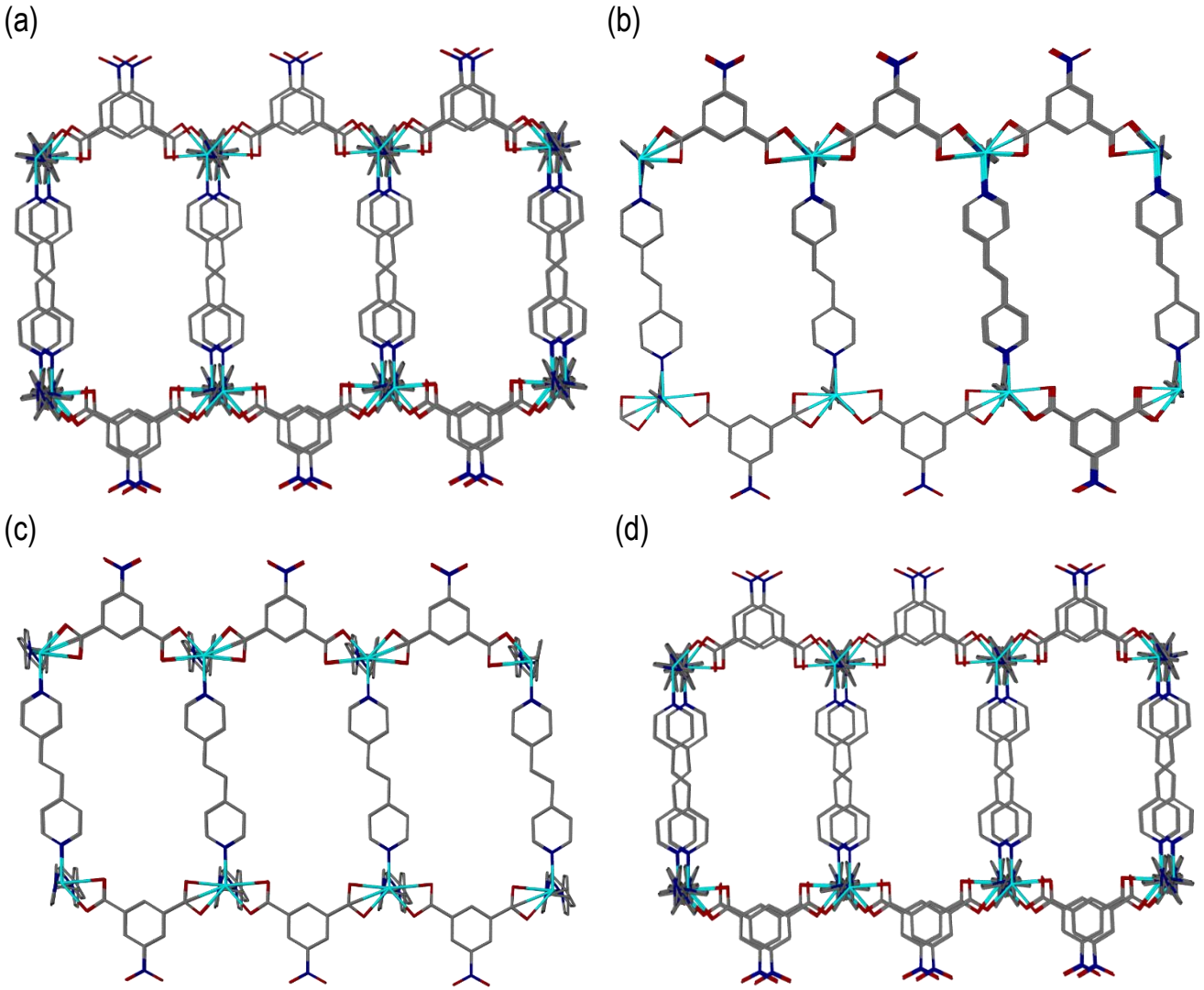

Figure 4.23 Common, edge-on view of hexagonal channels of (a) **4**, (b) **4'**, (c) **JECRAN** (104 K) and (d) **JECROB** (373 K). Solvent molecules in (a) and (c) and the hydrogen atoms of all MOFs have been removed for clarity.

4.3.3.2 Void Space Analysis

Void space analysis was explored as a means of correlating the observed sorption characteristics with the structural characteristics of **3**, **4** and **JECRAN**. Comparisons were made between the weighted averages of the potential void spaces per unit cell, when the solvents were artificially removed, of **3**, **4** and **JECRAN** and the actual void spaces per unit cell of desolvated **4'** and **JECROB**[85] (**Table 4.7**). The actual void space analysis serves as a direct comparison with sorption studies of the activated MOFs while the potential void space analysis serves as a reference for conclusions based on the as-synthesised MOFs.

The weighted average potential void spaces per unit cell of MOFs **3** (8.8%, 462 $Å^3$), **4** (14.1%, 770 $Å^3$) and **JECRAN** (12.6%, 173 $Å^3$) as well as the actual void spaces for **4'** (13.2%, 179 $Å^3$) and **JECROB** (7.2%, 394 Å), calculated as a weighted average over its four disordered components, are presented in **Table 4.7**. The observed decrease in actual void spaces for **4'** and **JECROB** compared to the potential void spaces of **4** and **JECRAN**, indicate that the respective MOFs undergo a degree of breathing with activation. The potential and actual void spaces in **JECRAN** and **JECROB** are smaller than those of **4** and **4'**, respectively.

To relate pore volumes to sorption study results which are typically reported in amount or volume of adsorbed gas per unit mass of activated material, the void space per unit mass for each structure was determined (**Table 4.7**).

Table 4.7 Void space analyses of potential void and actual void spaces of MOFs **3**, **4** and **JECRAN**

	3* (100 K)	**4* (100 K)**	**JECRAN* (104 K)**	**4' (173 K)**	**JECROB (373 K)**
Void space percent per unit cell (%)	8.8	14.1	12.6	13.2	7.2
Absolute void space per unit cell (Å^3/ unit cell)	462	770	173	179	394
Volume of unit cell (Å^3)	5303	5445	1363	1355	5476
Atomic mass unit (amu) per unit cell	4663.2	4759.2	1140.2	1189.7	4783.0
Void space per atomic mass (Å^3 / amu)	0.099	0.162	0.152	0.150	0.082
Void space per gram of MOF (cm^3 / g)	0.059	0.097	0.091	0.090	0.049

*solvent molecules are deleted

4.4 Liquid Sorption Studies

The retention of crystallinity for the bulk samples after desolvation of **3** and **4** suggests that these MOFs are strong candidates for liquid sorption experiments. Desolvated samples of **3** and **4** were tested for sorption of liquids with a wide range of polarities.

4.4.1 Thermogravimetric Analysis

Samples were heated to 393 K and 573 K, as guided by TGA experiments, for one hour to remove guest molecules for **3** and **4**, respectively. To confirm solvent loss, treated samples underwent subsequent TG analysis to 473 K. Flat thermograms for both compounds confirmed that solvent molecules had been completely removed from both samples. Thereafter, samples were immersed in various solvents for 24 h or 48 h. TG analyses were performed on the samples to determine the degree of sorption as summarised in **Table 4.8** and **4.9**.

Compound **3'** shows the highest sorption for the more polar solvents, water (4.3 molecules per ASU), DMF (2.6 molecules per ASU) and shows liquid sorption for EtOH (1.1 molecules per ASU). Interestingly, **3'** adsorbed more DMF than found in the as-synthesised compound. **3'** also showed some sorption for MeOH (0.3 molecules per ASU), whilst chloroform and benzene were not adsorbed.

Compound **4'** showed completely different liquid sorption behaviour, adsorbing approximately a single molecule of water (1.1 molecules per ASU), DMF (1.2 molecules per ASU) and MeOH (1.4 molecules per ASU). This sample showed low sorption for EtOH, chloroform and benzene, only adsorbing half a molecule in each case.

In a similar set of experiments, **JECRAN** showed no sorption for MeOH, chloroform or toluene. However, **JECRAN** showed 14.6% DMF solvent loss after liquid sorption experiments which was higher than the as-synthesised DMF loss of 9.7%.[86]

Table 4.8 Results summary of the liquid sorption experiments for **3'**. Solvents have been ordered from highest to lowest polarity[78]

Solvent	TGA Mass Loss (%)	No. Solvent Molecules Adsorbed per ASU	Temperature Range (K)	Calculated Mass Loss (%)*
DMF *(as-synthesised)*	7.1	-	305 – 521	7.2
Water	11.6	4.3	293 - 473	3.0
DMF	24.5	2.6	293 – 523	11.2
EtOH	7.9	1.1	295 – 323	7.3
MeOH	1.7	0.3	296 – 312	5.2
Chloroform	0.0	0.0	-	11.8
Benzene	0.0	0.0	-	17.0

*When one molecule per ASU is adsorbed

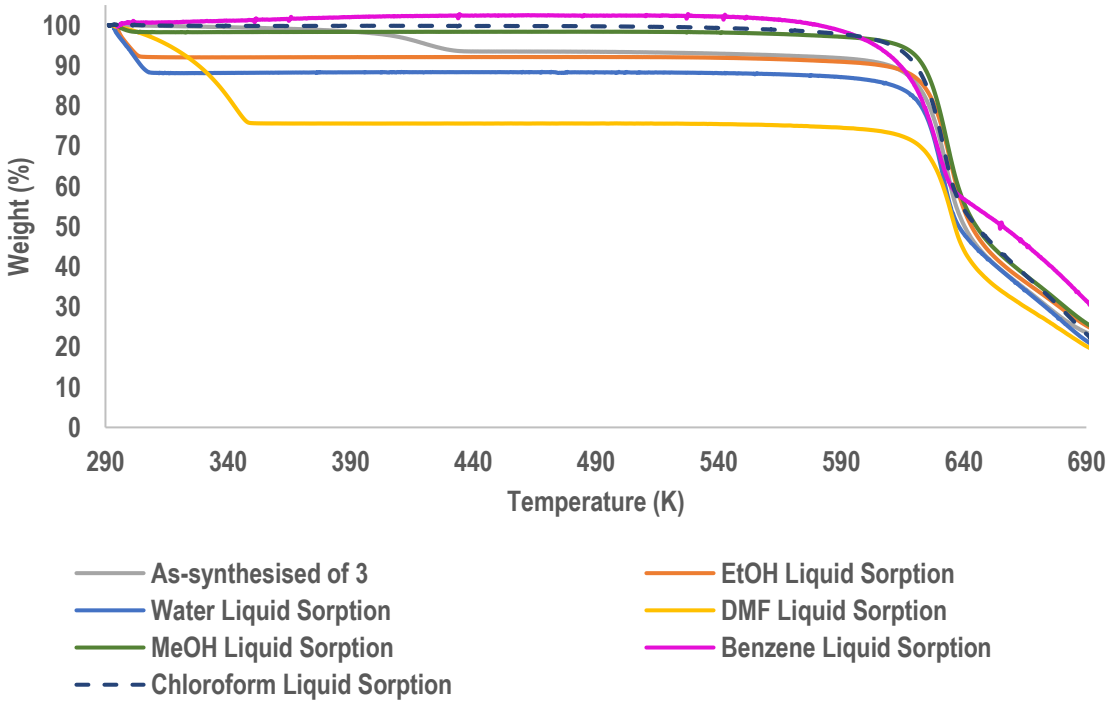

Figure 4.24 TGA for the as-synthesised MOF **3** (grey) against the desolvated MOF **3'** submerged in EtOH (orange), water (blue), DMF (yellow), MeOH (green), benzene (pink) and chloroform (dashed navy) for 24 h or 48 h.

Table 4.9 Results summary of the liquid sorption experiments for **4'**. Solvents have been ordered from highest to lowest polarity[78]

Solvent	TGA Mass Loss (%)	No. Solvent Molecules Adsorbed per ASU	Temperature Range (K)	Calculated Mass Loss (%)*
DMF *(as-synthesised)*	10.9	-	305 – 521	10.9
Water	3.1	1.1	293 – 423	2.9
DMF	12.5	1.2	295 – 545	10.9
EtOH	3.3	0.4	296 – 474	7.2
MeOH	6.9	1.4	291 – 535	5.1
Chloroform	8.9	0.5	298 – 522	16.7
Benzene	5.9	0.5	298 – 549	11.6

*When one molecule per ASU is absorbed

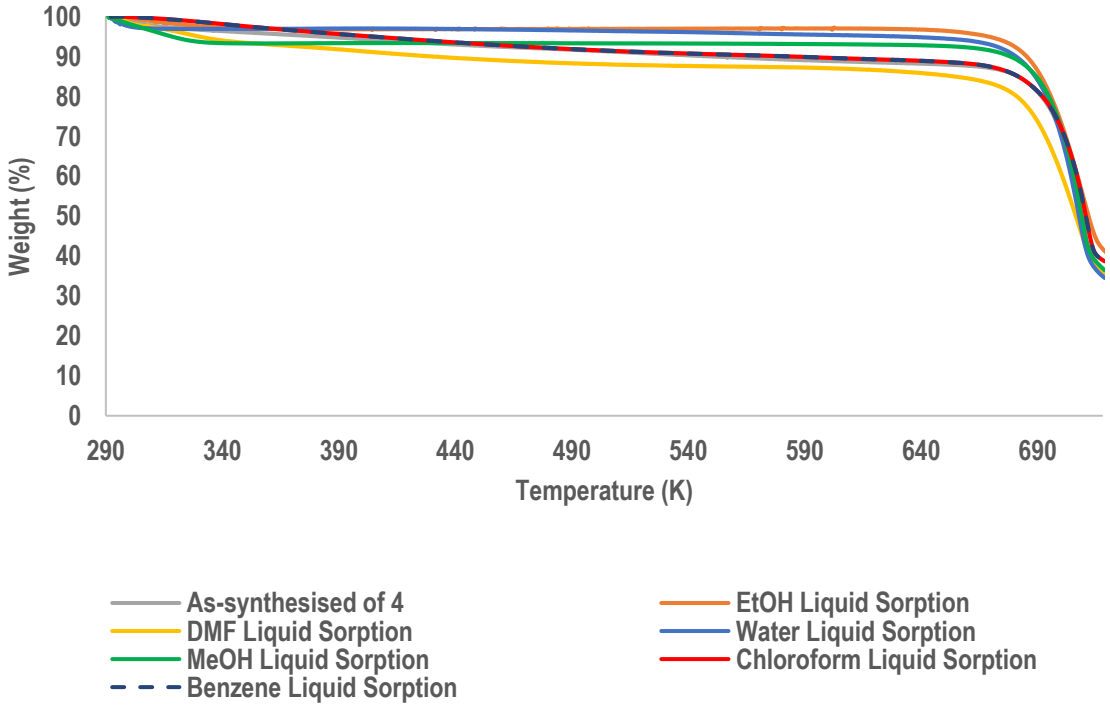

Figure 4.25 TGA for the as-synthesised MOF **4** (grey) against the desolvated MOF **4'** submerged in EtOH (orange), water (blue), DMF (yellow), MeOH (green), chloroform (red) and benzene (dashed navy) for 24 h or 48 h.

4.4.2 Powder X-ray Diffraction Experiments

Observations made during thermogravimetric analysis indicated that more water and DMF molecules were entering the desolvated framework of **3'** than expected from SCXRD analysis of the as-synthesised crystals. This degree of sorption was unexpected, thus PXRD experiments were conducted on sample **3'**, prepared in the same manner as was for the TGA experiments, to determine if structural changes with solvent sorption occurred.

Analysis of the PXRD patterns of **3'** after liquid sorption shows that there are vast differences in the powder patterns of the as-synthesised and desolvated sample (**Figure 4.26**). The as-synthesised pattern has peaks at 7.1°, 9.3°, 10.1°, 10.5°, 11.1° which do not appear in the desolvated pattern and the profiles of both patterns in the 2θ range 13.4° – 14.5° and 16.7° – 20.2° (indicated on the as-synthesised PXRD pattern of **3**) differ greatly. The PXRD pattern of the desolvated sample showed peaks in the 2θ range 11.6° - 13.0° and peaks at 20.5° and 23.0° (indicated on the desolvated PXRD pattern) which do not appear in the as-synthesised powder pattern. However, the powder patterns of the water liquid sorption and DMF liquid sorption experiments are virtually superimposable with the desolvation powder pattern. This suggests that desolvation of **3** facilitates structural changes that allow water and DMF to enter the sample without resulting in further structural changes.

Analysis of the PXRD patterns of **4** show vast differences between the as-synthesised and desolvated PXRD patterns of **4** (**Figure 4.27**). The as-synthesised PXRD pattern has peaks at 9.5° and 11.3° which appear as five intense peaks in the 2θ range 9.4° – 11.6 in the desolvated PXRD pattern, indicated on the as-synthesised and desolvated PXRD patterns, respectively. There are also new peaks at 15.11°, 19.4° and 20.9° in the desolvated powder pattern which do not appear in the as-synthesised powder pattern. Comparison of these PXRD patterns with the PXRD patterns of the liquid sorption experiments shows that the MeOH liquid sorption PXRD pattern is a good match with the desolvated pattern. The DMF liquid sorption PXRD pattern has the best match with the as-synthesised PXRD pattern of **4** with one new peak at 10.0°. Interestingly, the water liquid sorption pattern matches both the as-synthesised

and desolvated pattern with peaks at 15.2°, 17.2°, 17.7°, 20.6° and 21.0° (indicated with red asterisks on the water liquid sorption pattern) which match those in the desolvated pattern and peaks at 13.3°, 13.7° (indicated with green asterisks on the water liquid sorption pattern) matching those of the as-synthesised pattern.

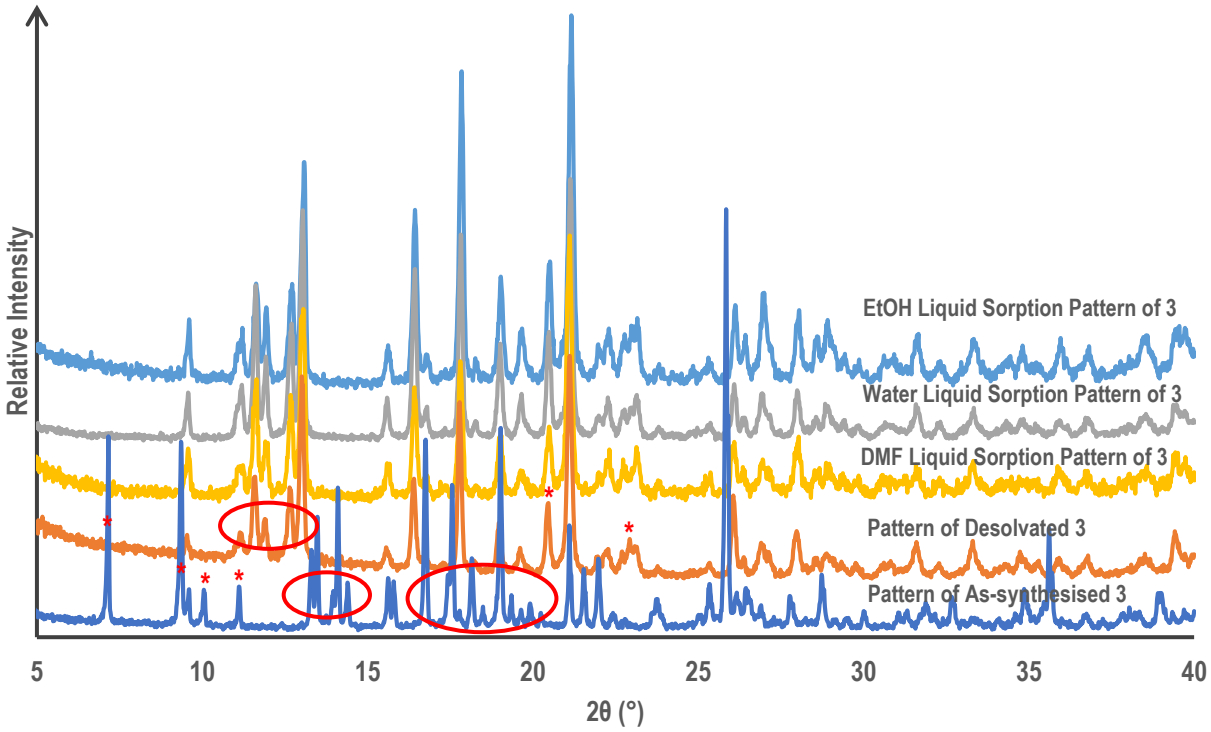

Figure 4.26 PXRD patterns for **3** as-synthesised and desolvated compared against DMF, EtOH and water liquid sorption experiments. Red asterisks and circles indicate peaks and peak regions specified in **section 4.4.2**.

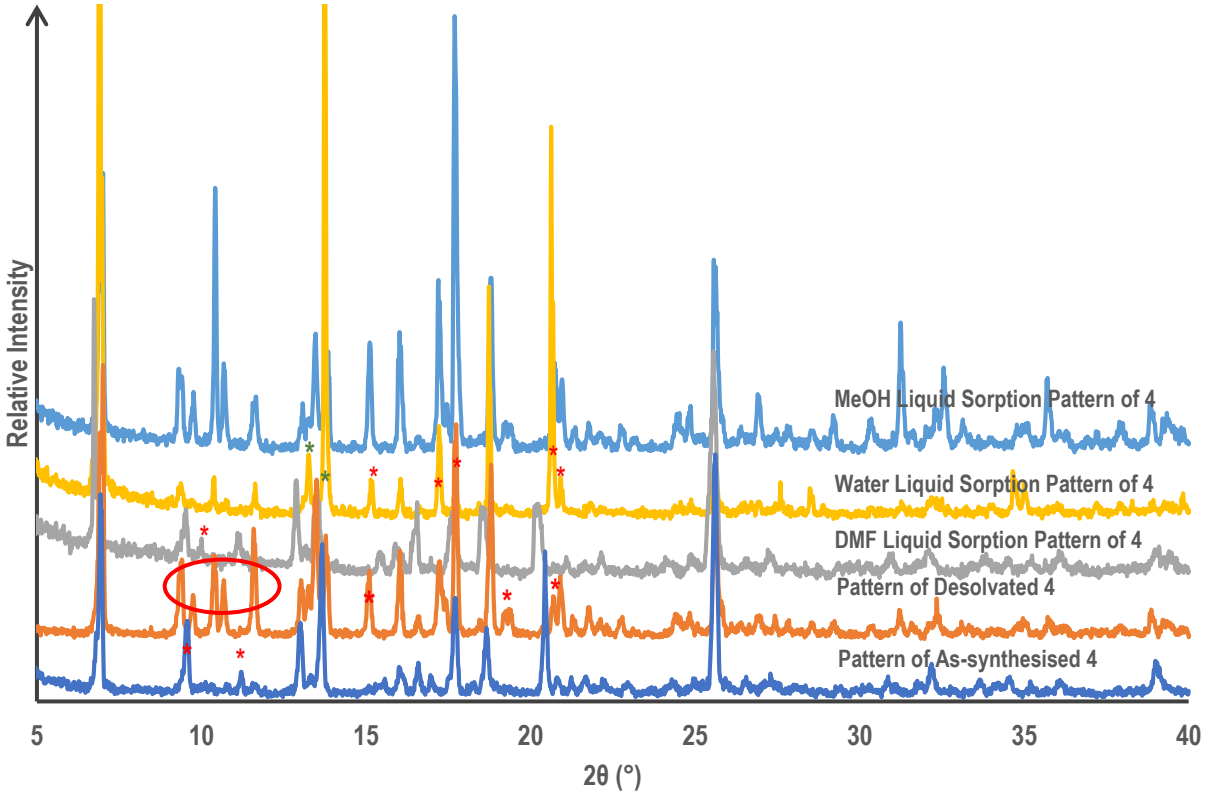

Figure 4.27 PXRD patterns for **4** as-synthesised and desolvated compared against DMF, MeOH and water liquid sorption experiments. Red and green asterisks and red circles indicate peaks and peak regions specified in **section 4.4.2**.

4.5 Gas Sorption Studies

Gas and water vapour sorption studies were conducted to determine the ability of activated samples of **3** and **4** to adsorb different gases. Gas sorption studies were also used to determine the BET surface area and isosteric heats of adsorption for each compound. Compounds **3** and **4** were heated to 393 K and 573 K, respectively, to activate them. Activated samples of **3** and **4**, hereafter referred to as **3'** and **4'**, respectively, were then tested for hydrogen (77 K), nitrogen (77 K), carbon dioxide (195 K and 298 K) and water vapour (298 K) sorption. Comparisons were made between the sorption capabilities of **3'**, **4'** and **JECROB**.[85]

Nitrogen and Hydrogen Sorption

Sample **3'** and **4'** showed no sorption for hydrogen or nitrogen. As both samples showed no sorption for nitrogen, nitrogen was deemed inappropriate for the BET surface calculation.

Carbon Dioxide Sorption

The sorption of carbon dioxide for samples **3'** and **4'** was measured at 298 K and 195 K. **3'** showed no sorption for carbon dioxide at 298 K and showed only moderate sorption for carbon dioxide at 195 K with a maximum sorption of 1.8 cm^3 (STP) g^{-1} (0.05 molecules of CO_2 per ASU) at 725 mmHg pressure. This low sorption could be due to structural changes after desolvation to a non-porous state, as indicated by changes in the VT-PXRD pattern of **3** when desolvated and an endothermic peak indicating a possible phase change after desolvation seen in the DSC thermogram. The maximum sorption of carbon dioxide at 298 K for **4'** was 27.5 cm^3 (STP) g^{-1} (0.73 molecules of CO_2 per ASU) at 796 mmHg and displayed a type-I isotherm. The maximum sorption of CO_2 for **JECROB** at 298 K, which also displayed a type-I isotherm, was reported at 15.6 cm^3 (STP) g^{-1} (0.41 CO_2 molecules per ASU) at an absolute pressure of 796 mmHg. Initially, the sorption capacity at 195 K for **4'** was considerably better than that of **JECROB** with a sharp increase in sorption to 50.0 cm^3 (STP) g^{-1} (1.33 molecules CO_2 per ASU) at a relatively low pressure of 4 mmHg. However, thereafter the sorption isotherm of **4'** plateaus to a maximum sorption amount of 54.4 cm^3 (STP) g^{-1} (1.44 molecules CO_2 per ASU) at 725 mmHg. This initial sharp increase in CO_2 sorption is also observed in **JECROB**. Although the sorption of **4'** is higher than that of **JECROB** at pressures below its first inflection point at 40 mmHg, where CO_2 sorption was 38.9 cm^3 (STP) g^{-1} (0.90 molecules CO_2), its second inflection point at 95 mmHg facilitated a great increase in CO_2 sorption to 56.0 cm^3 (STP) g^{-1} (1.46 CO_2 molecules per ASU) which surpassed even the maximum CO_2 sorption of **4'**. The maximum sorption of **JECROB** was 68.0 cm^3 (STP) g^{-1} at 724 mmHg (1.77 molecules CO_2 per ASU). This total sorption of nearly two CO_2 molecules in **JECROB** was hypothesised by Tahier and Oliver to be the result of a structural change as lateral movement of the bilayers which may have accommodated

the further sorption of CO_2.[85] This potential 'breathing' is absent in **4'** suggesting that the strength of interactions in **4'** is higher than that of **JECROB** at lower temperatures.

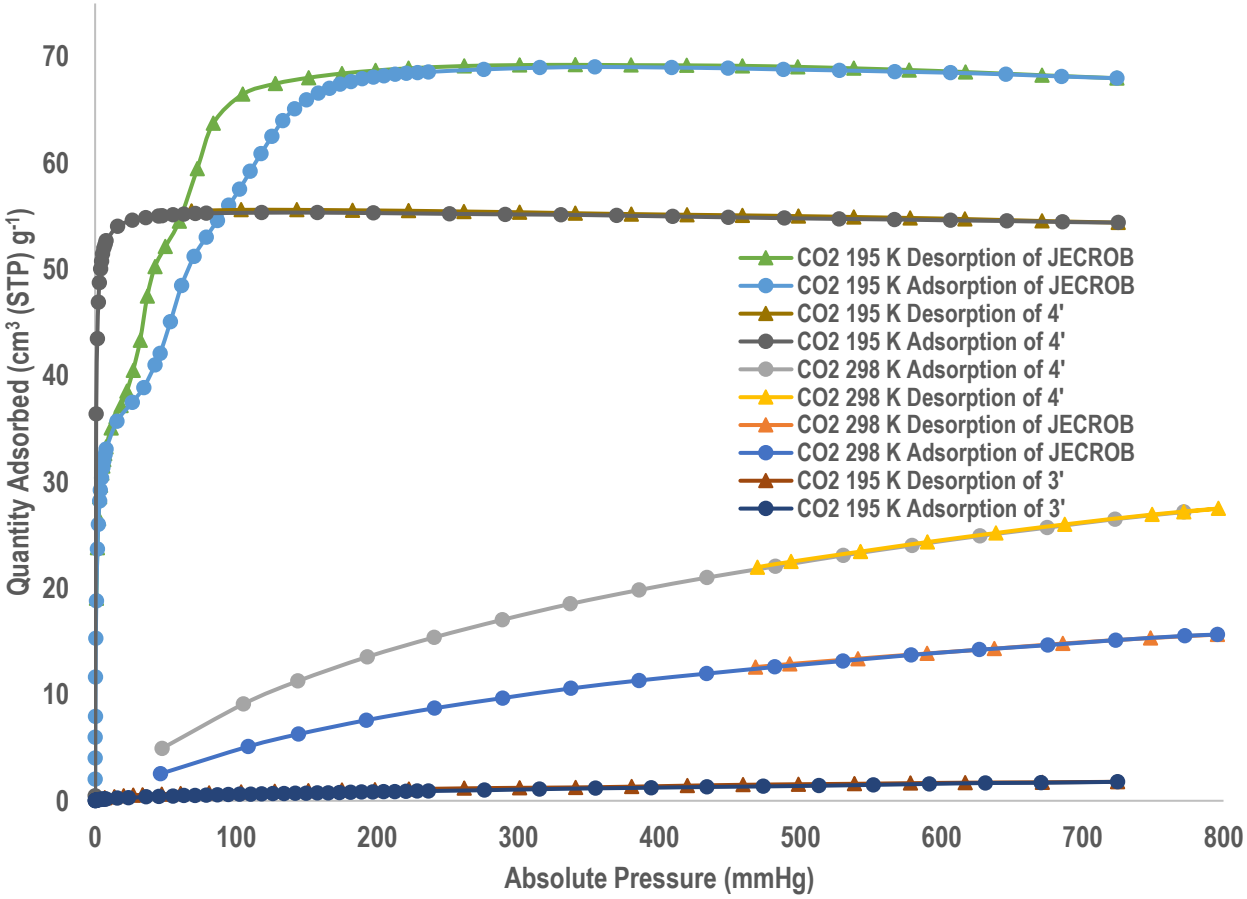

Figure 4.28 Adsorption and desorption isotherms for CO_2 sorption at 195 K for **3'** (navy/brown), **4'** (charcoal/brown) and **JECROB** (blue/green) and 298 K for **4'** (yellow/grey) and **JECROB** (blue/orange).

The maximum sorption of CO_2 at 273 K for **4'** was 42.2 cm^3 (STP) g^{-1} (1.11 molecules CO_2 per ASU) at 783 mmHg while **JECROB** was reported as having a maximum CO_2 sorption of 27.3 cm^3 (STP) g^{-1} (0.71 molecules CO_2 per ASU) at 783 mmHg. Bae, et al. showed that CO_2 sorption at 273 K could be used to determine BET surface in the absence of reliable N_2 sorption data.[82] As **4'** showed no sorption for nitrogen, carbon dioxide sorption at 273 K was used to determine the BET surface areas of these MOFs. The BET surface is reported as 192 m^2 g^{-1} for **4'** and 119 m^2 g^{-1} for **JECROB** which may explain the initial

higher sorption for **4'** before structural changes occur in **JECROB**. However, **3'** showed no sorption for carbon dioxide at 273 K, hence no BET surface area is reported.

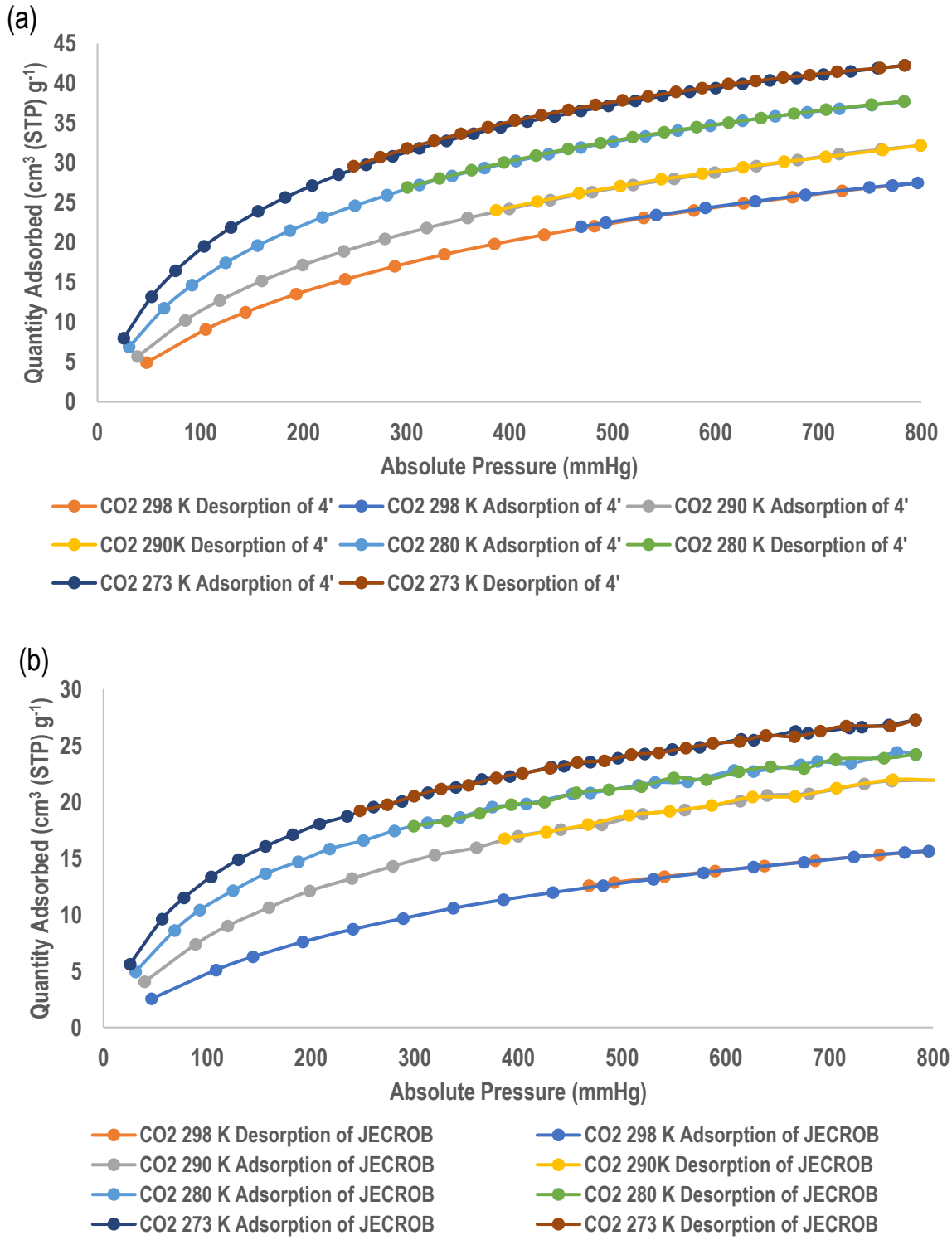

Figure 4.29 Adsorption and desorption isotherms for (a) **4'** and (b) **JECROB** for CO_2 (273 K – 298 K)

The isosteric heat of adsorption (Q_{st}) (**Table 4.10**) values for **4'** and **JECROB** were calculated using CO_2 sorption at 273 K, 280 K, 290 K and 298 K which conformed to a type-I curve. The Q_{st} values for **4'** was calculated at 33.8 – 34.3 kJ mol^{-1} at a coverage of 6.6 – 15.6 cm^3 (STP) g^{-1}. The reported Q_{st} values for **JECROB** were 41.5 – 43.6 kJ mol^{-1} over a coverage range of 5.6 – 15.5 cm^3 (STP) g^{-1}. This indicates that there were strong interactions of CO_2 with the frameworks of both MOFs, however, the interactions in **JECROB** were stronger than in **4'** over the specified coverage ranges.

Table 4.10 Isosteric Heat of Adsorption (Q_{st}) for **4** and **JECROB**

MOF	**4'**	**JECROB**
Coverage Range (cm^3 (STP) g^{-1})	6.6 – 15.6	5.6 – 15.5
Q_{st} Range (kJ mol^{-1})	33.8 – 34.3	41.5 – 43.6

Hirshfeld Surface and PLATON Analysis

Assessment of the Hirshfeld surfaces and isolated, intermolecular interactions of **4'** (173 K) and **JECROB** (373 K) revealed distinct differences that may offer a clue for the carbon dioxide sorption behaviour of the samples. The isolated, intermolecular interactions of **4'** indicated C-H···O interactions between the axial **bpee** ligands of the green bilayer and the carboxylate group of the **nia** ligands of the neighbouring blue bilayer within hexagonal channels of the middle red bilayer (**Figure 4.30**). These interactions possibly limit the ability of the axial **bpee** ligands to move and allow the void spaces (channels are located on either side of the C-H···O interaction) to increase in size and accommodate more sorption. These interactions are completely absent in the case of **JECROB** which only has intramolecular C-H···O interactions (**Table 4.11** and **4.12**). This interaction of catenated bilayers in **4'** may account for the carbon dioxide sorption behaviour of **4'** at 195 K which although initially high, quickly plateaus, whereas in

JECROB the bilayers do not interact with neighbouring bilayers in the same fashion which may allow the bilayers and **bpe** ligands to move and allow the further sorption of almost two carbon dioxide molecules.

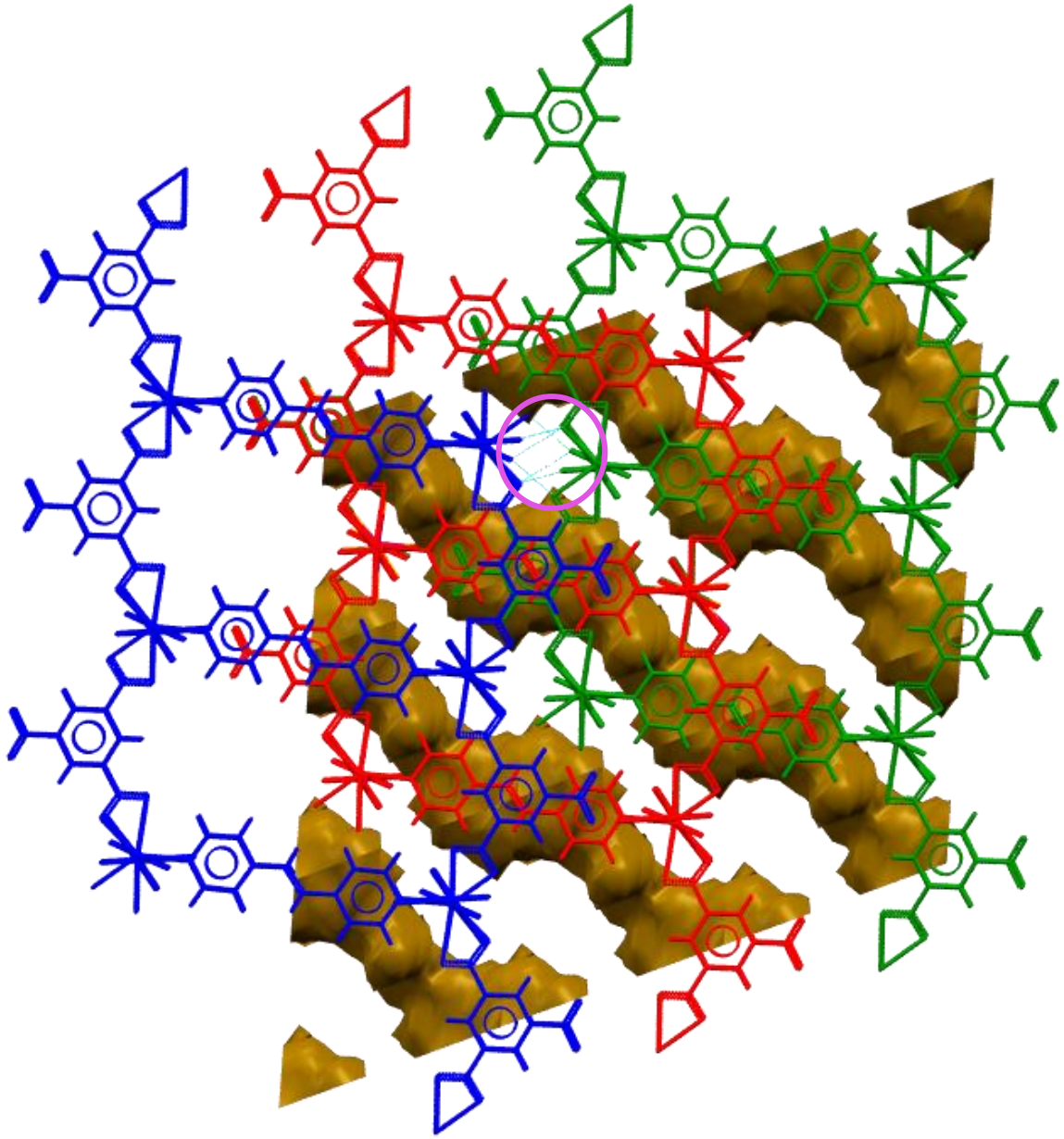

Figure 4.30 Edge on view of **4'** (173 K) showing light blue lines (circled in pink) depicting intermolecular C14-H14···O4 and C17-H17···O1 interactions, as obtained through PLATON, between the blue and green bilayer within the hexagonal channels of the red bilayers. All intramolecular interactions have been omitted for clarity.

Table 4.11 Hydrogen bonding parameters as obtained from PLATON for MOF **4'**

Hydrogen bonding atoms	D-H / Å	H···A / Å	D-H···A / Å	Symmetry operators
C14-H14···O4	0.93	2.51	3.386(7)	-x, -y,1-z
C17-H17···O1	0.93	2.50	3.418(6)	1-x, -y,1-z
C21-H21···O3 (intra)	0.93	2.46	2.149(7)	1+x, y, z
C25-H25···O2 (intra)	0.93	2.50	3.232(8)	

Table 4.12 Hydrogen bonding parameters as obtained from PLATON for MOF **JECROB**

Hydrogen bonding atoms	D-H / Å	H···A / Å	D-H···A / Å	Symmetry operators
C1C-H1C···O2D (intra)	0.93	2.50	3.2444(8)	
C1C-H1C···O2E (intra)	0.93	2.41	3.0572(7)	
C5C-H5C···O3D (intra)	0.93	2.50	3.1993(8)	x,1+y, z

The C14-H14 and C17-H17 region in the Hirshfeld surface analysis of the ASU of **4'** (**Figure 4.31** (a)) has a red region which indicates a short intermolecular contact. This observation supports the interbilayer C-H·· O bonding as obtained *via* PLATON. Although the Hirshfeld surface of **JECROB** (**Figure 4.31** (b)) shows more red regions, the PLATON analysis does not indicate any type of intermolecular interaction in these regions. The observation of red regions is, potentially, the result of the way in which the program CrystalExplorer handles disordered components (depicted as red or blue) rather than as an indicator of 'true' short intermolecular contacts.[73]

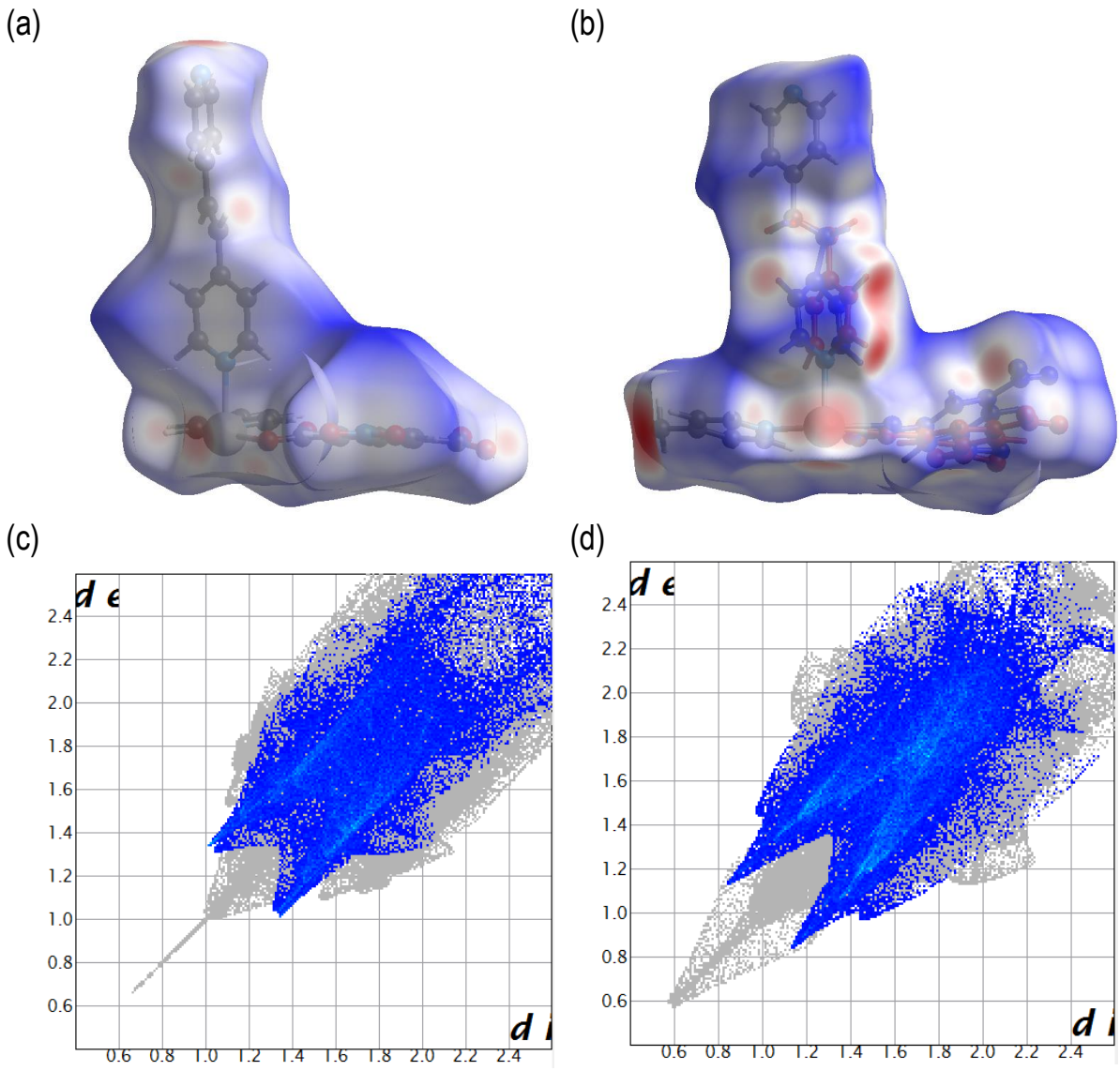

Figure 4.31 Hirshfeld surface of (a) **4'** (173 K) and (b) **JECROB** (373 K) and fingerprint plots for (c) **1'** (195 K) (d) **2'** (195 K)

Water Vapour Sorption

Compound **3'**, **4'** and **JECROB** showed an affinity for water vapour sorption. The maximum water vapour sorption for **JECROB** was reported at 68.1 cm^3 (STP) g^{-1} sorption at P/P_o = 0.77 (1.77 water molecules per ASU). The maximum water vapour sorption for **3'** was significantly lower than that of **JECROB** with a maximum water vapour sorption of 9.00 cm^3 (STP) g^{-1} at P/P_o = 0.77 (0.23 molecules of water per ASU). The low water vapour sorption of **3'** is, again, likely due to possible structural changes of **3** to a non-porous state after desolvation. The water sorption of **4'** was higher than that of **3'** with a maximum

sorption amount of 20.9 cm^3 (STP) g^{-1} at P/P_o = 0.77 (0.55 water molecules per ASU) which is almost a third of the total water vapour sorption of **JECROB**.

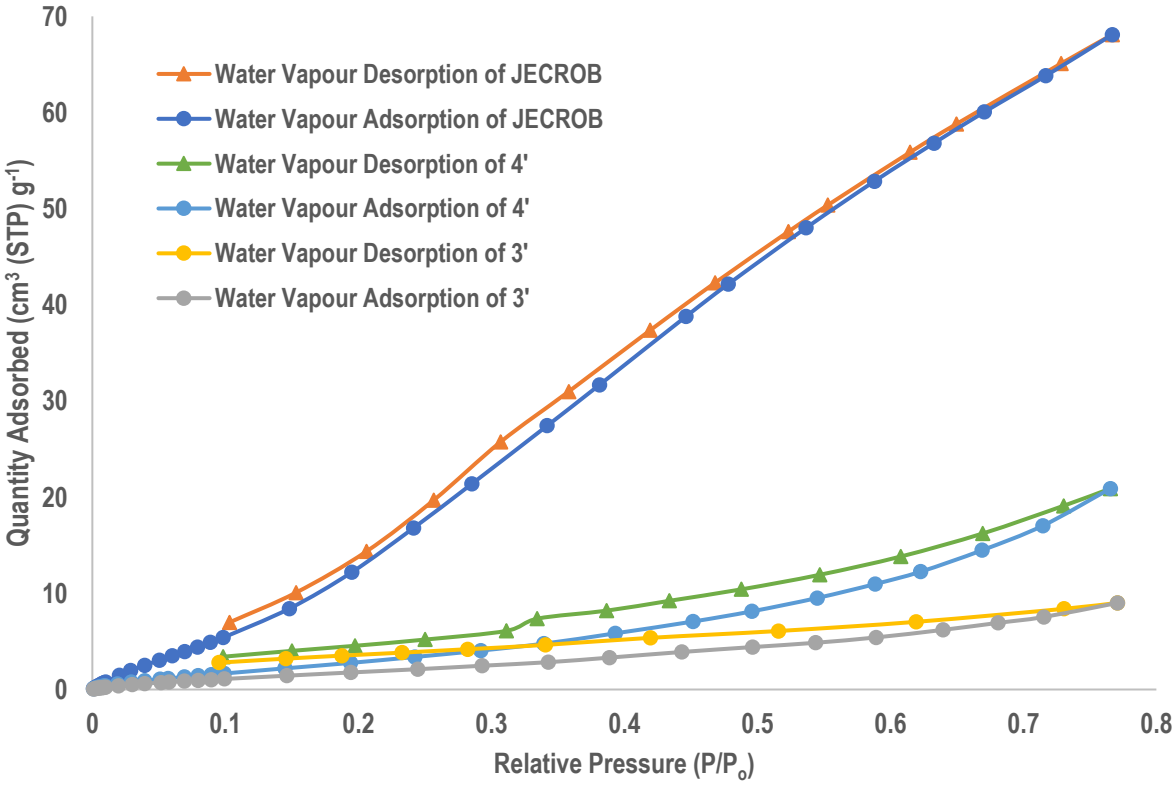

Figure 4.32 Adsorption and desorption isotherms for water vapour sorption (298 K) for **3'**, **4'** and **JECROB**.

Chapter 5:

Conclusions

5.1 Results Summary

In conclusion, four mixed-ligand MOFs were synthesised using either the metal salt $Zn(NO_3)_2 \cdot 6H_2O$ or $Cd(NO_3)_2 \cdot 4H_2O$ and the mixed-ligand combination of either bipyridyl ligand 1,2-bis(4-pyridyl)ethane (**bpe**) or 1,2-bis(4-pyridyl)ethylene (**bpee**) and the carboxylate ligand isophthalic acid (H_2**ia**), 5-methoxyisophthalic acid (H_2**mia**) or 5-nitroisophthalic acid (H_2**nia**). The Zn MOFs, $[Zn(\mu_2\text{-}\mathbf{ia})(\mu_2\text{-}\mathbf{bpe})]_n \cdot n$DMF (**1**) and $[Zn(\mu_2\text{-}\mathbf{mia})(\mu_2\text{-}\mathbf{bpe})]_n \cdot n$DMF (**2**) and the Cd MOFs $[Cd(\mu_2\text{-}\mathbf{mia})(\mu_2\text{-}\mathbf{bpe})_{1.5}]_n \cdot n(DMF)_{0.5}n(H_2O)_{0.5}$ (**3**) and $[Cd(\mu_2\text{-}\mathbf{nia})(\mu_2\text{-}\mathbf{bpee})_{1.5}]_n \cdot n$DMF (**4**) were characterised using SCXRD, PXRD, VT–PXRD, TGA, DSC and HSM. Additional VT–SCXRD and gas sorption experiments were carried out for **1** and **2** while additional liquid sorption and gas sorption experiments were carried out for **3** and **4**.

5.1.1 Zn MOFs $[Zn(\mu_2\text{-ia})(\mu_2\text{-bpe})]_n \cdot n$DMF (1) and $[Zn(\mu_2\text{-mia})(\mu_2\text{-bpe})]_n \cdot n$DMF (2)

The Zn MOFs synthesised were isoreticular, 2-periodic MOFs with a 2D, **sql** net topology. Although both compounds had similar starting materials and similar coordination modes, there were marked differences in their sorption behaviours. The activated single crystals of **1** and **2** were obtained through an intermediate hydrated phase (**1W** and **2W**). The water-exchanged compounds were heated *in situ*, during data collections, to 393 K to obtain the desolvated forms (**1'** and **2'**) in the single-crystal-single-crystal transformation **1** / **2** → **1W** / **2W** → **1'** / **2'**. Void space analysis showed that the compounds underwent some structural change, i.e. an inter-bilayer separation or 'breathing' effect, as suggested by the change in void space **1** (18.6%, 801 Å^3) / **2** (18.3%, 851 Å^3) → **1W** (14.5%, 614 Å^3) / **2W** (14.2%, 646 Å^3) → **1'** (195 K) (14.9%, 631 Å^3) / **2'** (195 K) (15.5%, 712 Å^3) or **1'** (298 K) (15.4%, 655 Å^3) / **2'** (298 K) (15.6%, 719 Å^3). These structural changes are attributed as a plausible explanation for CO_2 and water vapour sorption behaviours observed at 195 K and 298 K, respectively. Whereas the methoxy group may initially aid in carbon dioxide and water vapour sorption, as initial sorption for **2'** was observed to be higher than that of **1'**, the total sorption of CO_2 and water for **1'** was ultimately higher than for **2'**. It is possible that the methoxy group is ultimately responsible for retarding the inter-bilayer separation in **2'**. This observation

is further supported by empirical evidence as direct SC-SC desolvation was possible for **1'**, whereas it was not for **2'**. Furthermore, water-exchange experiments in **2'** took two weeks to reach completion, whereas the same experiment was complete in one day for **1'**.

Additionally, there is hysteresis in the carbon dioxide sorption at 195 K for **1'** that is not seen for **2'**. This hysteresis is interchanged during water sorption at 298 K, pointing to different modes of interaction with adsorbed water and carbon dioxide molecules for this isoreticular pair of MOFs.

5.1.2 Cd MOFs $[Cd(\mu_2\text{-mia})(\mu_2\text{-bpe})_{1.5}]_n \cdot n(DMF)_{0.5} n(H_2O)_{0.5}$ (3) and $[Cd(\mu_2\text{-nia})(\mu_2\text{-bpee})_{1.5}]_n \cdot n(DMF)_{0.5}$ (4)

The Cd MOFs synthesised were isoreticular, 2-periodic MOFs with a 3D, **sql** net topology. These MOFs were also isoreticular with MOF $[Cd(bpe)_{1.5}(nbdc)]_n \cdot n$DMF referred to by its CSD reference code, **JECRAN**.[85] Although these compounds also had similar starting materials and similar coordination modes, they had marked differences in their sorption behaviours. TGA heating of the crystals of **4** at 473 K was employed to obtain **4'**, the activated crystals of **4**. However, repeated attempts at acquiring activated single crystals for **3'** were unsuccessful, nevertheless, VT–PXRD experiments proved that **3** remained crystalline with desolvation. Successful liquid, gas and vapour sorption experiments confirmed that **3'** and **4'** were microporous. The desolvated form of **JECRAN** (referred to by its CSD reference code **JECROB**) was reported to be obtained through *in situ* heating during data collections up to 373 K.[85]

The sorption behaviour of all three MOFs varied significantly. The TGA results of liquid sorption experiments for **3'** showed its affinity for more polar solvents water, DMF and EtOH adsorbing 4.3, 2.6 and 1.1 molecules per ASU of each, respectively. On the other hand, **4'** showed an affinity for water, DMF and MeOH adsorbing 1.1, 1.2 and 1.4 molecules per ASU of each, respectively. Interestingly, **4'** showed a slightly higher affinity for benzene and chloroform than **3'**, adsorbing 0.5 molecules per ASU of each, whereas **3'** showed no sorption.

Gas and water vapour sorption experiments were carried out for **3'** and **4'** and compared to reported experiments for $[Cd(bpe)_{1.5}(nbdc)]_n$ (**JECROB**). Sorption for nitrogen and hydrogen was negligible for all three MOFs. **4'** and **JECROB** showed an affinity for low temperature carbon dioxide (195 K) and water vapour (298 K) sorption, with **JECROB** outperforming **3'** and **4'** in both instances. **3'** displayed a type-I sorption curve for carbon dioxide at 195 K, though sorption was low compared to **4'** and **JECROB**. The porosity of **3'**, particularly in gas and vapour sorption studies, may be due to possible structural changes to a non-porous state when **3** is desolvated. This observation is supported by observed differences in the VT-PXRD patterns of **3** after desolvation and an endothermic event after desolvation in the DSC of **3** which had an onset ~100 K before the onset of decomposition as seen in the TGA thermogram. While **4'** initially outperformed **JECROB** during carbon dioxide (195 K) sorption at pressures below the first inflection point of **JECROB** (39 mmHg), the second inflection points in the CO_2 sorption isotherm of **JECROB** indicated structural changes that allowed the maximum carbon dioxide (195 K) sorption of **JECROB** (68.0 cm^3 (STP) g^{-1} at 724 mmHg amounting to 1.77 molecules CO_2 per ASU) to surpass that of **3'** (1.8 cm^3 (STP) g^{-1} at 725 mmHg amounting to 0.05 CO_2 molecules per ASU) and eventually **4'** (54.4 cm^3 (STP) g^{-1} at 725 mmHg amounting to 1.44 CO_2 molecules per ASU). This observation is hypothesised to be the result of lateral bilayer movement in **JECROB** which allows more void space to open and accommodate more carbon dioxide. [85] Lack of inflection points suggests that **4'** does not display the same structural change. The appreciable water vapour sorption of **JECROB** (68.1 cm^3 (STP) g^{-1} sorption at P/P_o = 0.77 amounting to 1.77 water molecules per ASU) also surpassed that of **4'** (20.9 cm^3 (STP) g^{-1} at P/P_o = 0.77 amounting to 0.55 water molecules per ASU) and **3'** (9.00 cm^3 (STP) g^{-1} at P/P_o = 0.77 amounting to 0.23 molecules of water per ASU).

5.1.3 Final Remarks and Future Work

The objectives of this project were successfully met as the mixed-ligand approach was used to synthesis two pairs of isoreticular, mixed-ligand MOFs. The acid-base mixed-ligand strategy was employed to synthesise MOFs using either Zn(II) or Cd(II) metal ions with polycarboxylate and bipyridyl ligands. MOFs

were characterised using single crystal and powder X-ray diffraction, variable-temperature single crystal and powder X-ray diffraction and thermal analysis. The sorption capabilities of all synthesised MOFs were confirmed with liquid, gas and vapour sorption experiments. Comparison of the isoreticular MOFs with each other and existing structures allowed observations to be made about the effects of small functional changes to ligands employed in MOF synthesis. The activation of MOFs **1**, **2** and **4** occurred through single-crystal-to-single-crystal transformation which allowed some hypotheses to also be made about the structural changes behind these observed differences in sorption behaviour.

Suggestions for future work on the mixed-ligand MOFs include further investigation into acquiring a single crystal of activated **3** and VT–SCXRD experiments for **3** and **4** to track any possible structural changes in the frameworks with *in situ* heating. The synthesis of these compounds in pure DMF could also be explored to determine the effect of solvent on synthesis of MOFs.

References

1. Lehn, J. From supramolecular chemistry towards constitutional dynamic chemistry and adaptive chemistry. *Chem. Soc. Rev.* **2007**, *36*, 151-160.

2. Desiraju, G. R. Chemistry beyond the molecule. *Nature* **2001**, *412*, 397-400.

3. Desiraju, G. R. Crystal Engineering: From Molecule to Crystal. *J. Am. Chem. Soc.* **2013**, *135*, 9952-9967.

4. The Cambridge Crystallographic Data Centre. https://www.ccdc.cam.ac.uk/ (accessed 21 January, 2019).

5. Moghadam, P. Z.; Li, A.; Wiggin, S. B.; Tao, A.; Maloney, A. G. P.; Wood, P. A.; Ward, S. C.; Fairen-Jimenez, D. Development of a Cambridge Structural Database Subset: A Collection of Metal–Organic Frameworks for Past, Present, and Future. *Chem. Mater.* **2017**, *29*, 2618-2625.

6. Gómez-Gualdrón, D. A.; Colón, Y. J.; Zhang, X.; Wang, T. C.; Chen, Y.; Hupp, J. T.; Yildirim, T.; Farha, O. K.; Zhang, J.; Snurr, R. Q. Evaluating topologically diverse metal–organic frameworks for cryo-adsorbed hydrogen storage. *Energy Environ. Sci.* **2016**, *9*, 3279-3289.

7. Mason, J. A.; Oktawiec, J.; Taylor, M. K.; Hudson, M. R; Rodriguez, J.; Bachman, J. E.; Gonzalez, M. I.; Cervellino, A.; Guagliardi, A.; Brown, C. M.; Llewellyn, P. L.; Masciocchi; Jeffrey R. Long Methane storage in flexible metal-organic frameworks with intrinsic thermal management. *Nature* **2015**, *527*, 357-361.

8. Zhang, H.; Osgood, H.; Xie, X.; Shao, Y.; Wu, G. Engineering nanostructures of PGM-free oxygen-reduction catalysts using metal-organic frameworks. *Nano Energy* **2017**, *31*, 331-350.

9. Kholdeeva, O. A. Liquid-phase selective oxidation catalysis with metal-organic frameworks. *Catal. Today* **2016**, *278*, 22-29.

10. Tang, F.; Lin, R.; Lin, R.; Zhao, J. C.; Chen, B. Separation of C2 hydrocarbons from methane in a microporous metal-organic framework. *J. Solid State Chem.* **2018**, *258*, 346-350.

11. Xie, S.; Hu, C.; Li, L.; Zhang, J.; Fu, N.; Wang, B.; Yuan, L. Homochiral metal-organic framework for HPLC separation of enantiomers. *Microchem. J.* **2018**, *139*, 487-491.

12. Zhao, X.; Wang, Y.; Hao, X.; Liu, W. Fluorescent molecule incorporated metal-organic framework for fluoride sensing in aqueous solution. *Appl. Surf. Sci.* **2017***, 402*, 129-135.

13. Van de Voorde, B.; Bart, B. B.; Denayerb, J.; De Vos, D. Adsorptive separation on metal–organic frameworks in the liquid phase. *Chem. Soc. Rev.* **2014**, 5766-5788.

14. Wang, C.; Ke, S.; Cheng, C.; Wang, Y.; Chiu, H.; Ko, Y.; Sun, N.; Ho, M.; Chang, C.; Chuang, Y.; Lee, G. Four Mixed-Ligand Zn(II) Three-Dimensional Metal-Organic Frameworks: Synthesis, Structural Diversity, and Photoluminescent Property. *Polym. J.* **2017**, 644-661.

15. Batten, S. R.; Champness, N. R.; Chen, X.; Garcia-Martinez, J.; Kitagawa, S.; Öhrström, L.; O'Keeffe, M.; Suh, M. P.; Reedijk, J. Terminology of metal-organic frameworks and coordination polymers (IUPAC Recommendations 2013). *Pure Appl.Chem.* **2013***, 85*, 1715-1724.

16. Carlucci, L.; Ciani, G.; Proserpio, D. M.; Mitina, T. G.; Blatov, V. A. Entangled two-dimensional coordination networks: a general survey. *Chem. Rev.* **2014***, 114*, 7557-7580.

17. Yaghi, O. M.; O'Keeffe, M.; Ockwig, N. W.; Chae, H. K.; Eddaoudi, M.; Kim, J. Reticular synthesis and the design of new materials. *Nature* **2003**, *423*, 705-714.

18. Eddaoudi, M.; Kim, J.; Rosi, N.; Vodak, D.; Wachter, J.; O'Keeffe, M.; Yaghi, O. M. Systematic Design of Pore Size and Functionality in Isoreticular MOFs and Their Application in Methane Storage. *Science* **2002***, 295*, 469-472.

19. Rowsell, J. L. C.; Yaghi, O. M. Metal–organic frameworks: a new class of porous materials. *Microporous and Mesoporous Mater.* **2004***, 73*, 3-14.

20. Li, H.; Eddaoudi, M.; O'Keeffe, M.; Yaghi, O. M. Design and synthesis of an exceptionally stable and highly porous metal-organic framework. *Nature* **1999***, 402*, 276-279.

21. Thallapally, P. K.; Lloyd, G. O.; Atwood, J. L.; Barbour, L. J. Diffusion of Water in a Nonporous Hydrophobic Crystal. *Angew. Chem. Int. Ed.* **2005***, 117*, 3916-3919.

22. Bell, R. G. What are zeolites? http://www.bza.org/zeolites/ (accessed 22 January, 2019).

23. Batten, S. R.; Robson, R. Interpenetrating Nets: Ordered, Periodic, Entanglement. *Angew. Chem. Int. Ed.* **1998**, 1460-1494.

24. Fan, J.; Sun, W.; Okamura, T.; Zheng, Y.; Sui, B.; Tang, W.; Ueyama, N. Novel Metal−Organic Frameworks with Specific Topology Formed through Noncovalent Br···Br Interactions in the Solid State. *Cryst. Growth Des.* **2004***, 4*, 579-584.

25. Jiang, H.; Makal, T. A.; Zhou, H. Interpenetration control in metal–organic frameworks for functional applications. *Coord. Chem. Rev.* **2013***, 257*, 2232-2249.

26. Sun, D.; Ma, S.; Ke, Y.; Collins, D. J.; Zhou, H. An interweaving MOF with high hydrogen uptake. *J. Am. Chem. Soc.* **2006***, 128*, 3896-3897.

27. Nakahama, M.; Furukawa, S.; Kondo, M.; Shimomura, S.; Takashima, Y.; Kitagawa, S.; Sugimoto, K.; Uehara, H.; Martínez, V. M. Molecular decoding using luminescence from an entangled porous framework. *Nat. Commun.* **2011***, 2*, 168-175.

28. Wang, M.; Guo, L.; Cao, D. Metal-organic framework as luminescence turn-on sensor for selective detection of metal ions: Absorbance caused enhancement mechanism. *Sensor Actuat. B-Chem.* **2018***, 256*, 839-845.

29. Nijem, N.; Wu, H.; Canepa, P.; Marti, A.; Balkus, J., Kenneth J; Thonhauser, T.; Li, J.; Chabal, Y. J. Tuning the gate opening pressure of Metal-Organic Frameworks (MOFs) for the selective separation of hydrocarbons. *J. Am. Chem. Soc.* **2012***, 134*, 15201-15204.

30. Khan, N. A.; Jhung, S. H. Adsorptive removal and separation of chemicals with metal-organic frameworks: Contribution of π-complexation. *J. Hazard. Mater.* **2017***, 325*, 198-213.

31. Bae, Y.; Mulfort, K. L.; Frost, H.; Ryan, P.; Punnathanam, S.; Broadbelt, L. J.; Hupp, J. T.; Snurr, R. Q. Separation of CO2 from CH4 using mixed-ligand metal-organic frameworks. *Langmuir* **2008***, 24*, 8592-8598.

32. Tang, F.; Lin, R.; Lin, R.; Zhao, J. C.; Chen, B. Separation of C2 hydrocarbons from methane in a microporous metal-organic framework. *J. Solid State Chem.* **2018***, 258*, 346-350.

33. Ogawa, T.; Iyoki, K.; Fukushima, T.; Kajikawa, Y. Landscape of Research Areas for Zeolites and Metal-Organic Frameworks Using Computational Classification Based on Citation Networks. *Mater. J.* **2017***, 10*, 1428-1447.

34. Millward, A. R.; Yaghi, O. M. Metal-Organic Frameworks with Exceptionally High Capacity for Storage of Carbon Dioxide at Room Temperature. *J. Am. Chem. Soc.* **2005***, 127*, 17998-17999.

35. Caro, J. Are MOF membranes better in gas separation than those made of zeolites? *Curr. Opin. Chem. Eng.* **2011***, 1*, 77-83.

36. Burth, N. C.; Jasaju, H.; Walton, K. S. Water Stability and Adsorption in Metal−Organic Frameworks. *Chem. Rev.* **2014***, 114*, 10575-10612.

37. Jeremias, F.; Khutia, A.; Henninger, S. K.; Janiak, C. MIL-100(Al, Fe) as water adsorbents for heat transformation purposes—a promising application. *J. Mater. Chem.* **2012***, 22*, 10148-10151.

38. Küsgens, P.; Rose, M.; Senkovska, I.; Fröde, H.; Henschel, A.; Siegle, S.; Kaskel, S. Characterization of metal-organic frameworks by water adsorption. *Microporous and Mesoporous Mater.* **2009***, 120*, 325-330.

39. Chand, S.; Pal, A.; Das, M. C. A Moisture-Stable 3D Microporous CoII-Metal–Organic Framework with Potential for Highly Selective CO2 Separation under Ambient Conditions. *Chem. Eur. J.* **2018***, 24*, 5982-5986.

40. Pal, A.; Chand, S.; Das, M. C. A Water-Stable Twofold Interpenetrating Microporous MOF for Selective CO2 Adsorption and Separation. *Inorg. Chem.* **2017***, 56*, 13991-13997.

41. Jasuja, H.; Walton, K. S. Effect of catenation and basicity of pillared ligands on the water stability of MOFs. *Dalton Trans.* **2013***, 42*, 15421-15426.

42. Mendes, R. F.; Almeida Paz, F. A. Dynamic breathing effect in metal-organic frameworks: Reversible 2D-3D-2D-3D single-crystal to single-crystal transformation. *Inorganica Chim. Acta* **2017***, 460*, 99-107.

43. Naumov, P. E.; Bharadwaj, P. K. Single-crystal-to-single-crystal transformations. *CrystEngComm* **2015***, 17*, 8775-8775.

44. Jiang, P.; Peng, F.; Chen, Y. Temperature-induced single-crystal-to-single-crystal transformation of a binuclear Mn(II) complex into a 1D chain polymer. *RSC Adv.* **2016**, *6*, 89192-89197.

45. Shin, S.; Jeong, S.; Kim, D.; Lah, M. S. Reversible Single-Crystal-to-Single-Crystal Transformations of Metal–Organic Frameworks that Accompany Two-Dimensional Framework Reorganizations. *Cryst. Growth Des.* **2017***, 17*, 2228-2237.

46. Husain, A.; Ellwart, M.; Bourne, S. A.; Öhrström, L.; Oliver, C. L. Single-Crystal-to-Single-Crystal Transformation of a Novel 2-Fold Interpenetrated Cadmium-Organic Framework with Trimesate and 1,2-Bis(4-pyridyl)ethane into the Thermally Desolvated Form Which Exhibits Liquid and Gas Sorption Properties. *Cryst. Growth Des.* **2013***, 13*, 1526-1534.

47. Zeng, M.; Tan, Y.; He, Y.; Yin, Z.; Chen, Q.; Kurmoo, M. A porous 4-fold-interpenetrated chiral framework exhibiting vapochromism, single-crystal-to-single-crystal solvent exchange, gas sorption, and a poisoning effect. *Inorg. Chem.* **2013***, 52*, 2353-2360.

48. Murdock, C. R.; Hughes, B. C.; Lu, Z.; Jenkins, D. M. Approaches for synthesizing breathing MOFs by exploiting dimensional rigidity. *Coord. Chem. Rev.* **2014***, 258-259*, 119-136.

49. Yin, Z.; Zhou, Y.; Zeng, M.; Kurmoo, M. The concept of mixed organic ligands in metal-organic frameworks: design, tuning and functions. *Dalton Trans.* **2015***, 44*, 5258-5275.

50. Du, M.; Li, C.; Liu, C.; Fang, S. Design and construction of coordination polymers with mixed-ligand synthetic strategy. *Coord. Chem. Rev.* **2013***, 257*, 1282-1305.

51. Qi, Y.; Che, Y.; Batten, S. R.; Zheng, J. Unprecedented trinodal 4-connected metal–organic frameworks (MOFs) with 2-fold interpenetration. *CrystEngComm* **2008***, 10*, 1027-1030.

52. Koh, K.; Wong-Foy, A. G.; Matzger, A. J. A crystalline mesoporous coordination copolymer with high microporosity. *Angew. Chem. Int. Ed.* **2008***, 47*, 677-680.

53. Eddaoudi, M.; Li, H.; Yaghi, O. M. Highly porous and stable metal-organic frameworks: Structure design and sorption properties. *J. Am. Chem. Soc.* **2000**, *122*, 1391-1397.

54. Hou, L.; Zhang, J.; Chen, X. Two Metal-Carboxylate Frameworks Featuring Uncommon 2D + 3D and 3-Fold-Interpenetration: (3,5)-Connected Isomeric hms and gra Nets. *Cryst. Growth Des.* ***2009****, 9*,2415-2419.

55. Liu, X.; Fang, Q.; Zhu, G.; Xue, M.; Shi, X.; Wu, G.; Tian, G.; Qiu, S.; Fang, L. Crystal structure and fluorescence of a novel 3D inorganic–organic hybrid polymer with mixed ligands. *Inorg. Chem. Commun.* **2003***, 7*, 31-34.

56. Xu, L.; Guo, G.; Liu, B.; Wang, M.; Huang, J. 2-D open frameworks and blue fluorescence of two new zinc coordination polymers with mixed ligands. *Inorg. Chem. Commun.* **2004***, 7*, 1145-1149.

57. Huang, F.; Tian, J.; Chen, G.; Li, D.; Gu, W.; Liu, X.; Yan, S.; Liao, D.; Cheng, P. A case study of the ZnII-BDC/bpt mixed-ligand system: positional isomeric effect, structural diversification and luminescent properties. *CrystEngComm* **2010***, 12*, 1269-1279.

58. Yue-Qing Zheng; Jie Zhang; Ji-Yong Liu New Zn(II) coordination polymers with 1,3-bis(4-pyridyl)-propane: syntheses, crystal structures and properties. *CrystEngComm* **2010**, *12*, 2740-2748.

59. Wang, X.; Liu, G. Syntheses and Crystal Structures of Three Cu(II) Coordination Polymers Based on 1,3,5-Tris(imidazol-1-yl)benzene and Benzene Carboxylate Ligands. *J. Chem. Crystallogr.* **2016**, *46*, 252-261.

60. Habib, H. A.; Sanchiz, J.; Janiak, C. Mixed-ligand coordination polymers from 1,2-bis(1,2,4-triazol-4-yl)ethane and benzene-1,3,5-tricarboxylate: Trinuclear nickel or zinc secondary building units for three-dimensional networks with crystal-to-crystal transformation upon dehydration. *Dalton Trans.* **2008**, *13*, 1734-1744.

61. Yaghi, O. M.; Davis, C. E.; Li, G.; Li, H. Selective Guest Binding by Tailored Channels in a 3-D Porous Zinc(II)Benzenetricarboxylate Network. *J. Am. Chem. Soc.* **1997***, 119*, 2861-2868.

62. Lin, Z.; Liu, T.; Xu, B.; Han, L.; Huang, Y.; Cao, R. Pore-size tuning in double-pillared metal–organic frameworks containing cadmium clusters. *CrystEngComm* **2011***, 13*, 3321-3324.

63. *Bruker (2013)*, Bruker AXS Inc.: Madison WI, 2007.

64. Sheldrick, G. M. *SADABS*; Bruker AXS Inc.: Madison, WI, 2001.

65. Sheldrick, G. M. SHELXT Integrated space-group and crystal-structure determination. *Acta Crystallogr., Sect. A: Found. Adv.* **2015***, 71*, 3-8.

66. Barbour, L. J. LAYER– a computer program for the graphic display of intensity data as simulated precession photographs. *J. Appl. Crystallogr.* **1999**, *32*, 351-352.

67. Sheldrick, G. M. Crystal structure refinement with SHELXL. *Acta Crystallogr., Sect. C: Struct. Chem.* **2015**, *71*, 3-8.

68. The SHELX-97Manual. http://www.unics.uni-hannover.de/nhccurla/chemie/programme/shelx/SHELX-97%20Manual.pdf (accessed 6 February, 2019).

69. Thorn, A.; Dittrich, B.; Sheldrick, G. M. Enhanced rigid-bond restraints. *Acta Cryst., Sect. A.* **2012**, *68*, 448-451.

70. Barbour, L. J. X-Seed — A Software Tool for Supramolecular Crystallography. *J. Supramol. Chem.* **2001**, *1*, 189-191.

71. Dolomanov, O. V.; Bourhuis, L. J.; Gildea, R. J.; Howard, K.; Puschmann, H. OLEX2: a complete structure solution, refinement and analysis program. *J. Appl. Crystallogr.* **2009**, *42*, 339-341.

72. Macrae, C. F.; Bruno, I. J.; Chisholm, J. A.; Edgington, P. R.; McCabe, P.; Pidcock, E.; Rodriguez-Monge, L.; Taylor, R.; Van De Streek, J.; Wood, P. A. Mercury CSD 2.0– new features for the visualization and investigation of crystal structures. *J. Appl. Crystallogr.* **2008**, *41*, 466-470.

73. The Hirshfeld Surface. http://crystalexplorer.scb.uwa.edu.au/wiki/index.php/The_Hirshfeld_Surface (accessed 26 January, 2019).

74. McKinnon, J. J.; Mitchell, A. S.; Spackman, M. A. Hirshfeld Surfaces: A New Tool for Visualising and Exploring Molecular Crystals. *Chem. Eur. J.* **1998**, *4*, 2136-2141.

75. Universal Analysis QuickStart Course. https://www.tainstruments.com/universal-analysis-quickstart-course/ (accessed 2 February, 2019).

76. *TRIOS Software*; TA Instruments: New Castle, DE, 2018.

77. *analysis Program*, Soft Imaging System GmbH Digital Solutions for Imaging and Microscopy: Munster, Germany, 2000.

78. Polarity Index. http://macro.lsu.edu/howto/solvents/polarity%20index.htm (accessed 26 January, 2019).

79. Fenn, T. D.; Ringe, D.; Petsko, G. A. POVScript+: a program for model and data visualization using persistence of vision ray-tracing. *J. Appl. Crystallogr.* **2003**, *36*, 944-947.

80. Spek, A. L. Single-crystal structure validation with the program PLATON. *J. Appl. Crystallogr.* **2003**, *36*, 7-13.

81. Yang, L.; Powell, D. R.; Houser, R. P. Structural Variation in Copper(I) Complexes with Pyridylmethylamide Ligands: Structural Analysis with a New Four-Coordinate Geometry Index, τ_4. *Dalton Trans.* **2007**, *955*, 955-964.

82. Kim, K. C.; Yoon, T.; Bae, Y. Applicability of using CO 2 adsorption isotherms to determine BET surface areas of microporous materials. *Microporous and Mesoporous Materials* **2016**, *224*, 294-301.

83. Ambroz, F.; MacDonald, T. J.; Martis, V.; Parkin, I. P. Evaluation of the BET Theory for the Characterization of Meso and Microporous MOFs. *Small Methods* **2018**, *2*, 1800173-1800189.

84. Ng, E.; Mintova, S. Nanoporous materials with enhanced hydrophilicity and high water sorption capacity. *Microporous and Mesoporous Mater.* **2008**, *114*, 1-26.

85. Tahier, T.; Oliver, C. L. A Cd mixed-ligand MOF showing ligand-disorder induced breathing behaviour at high temperature and stepwise, selective carbon dioxide adsorption at low temperature. *CrystEngComm* **2017**, *19*, 3607-3618.

86. Tahier, T. Crystal Engineering of Mixed-Ligand Metal Organic Frameworks, University of Cape Town, 2016.